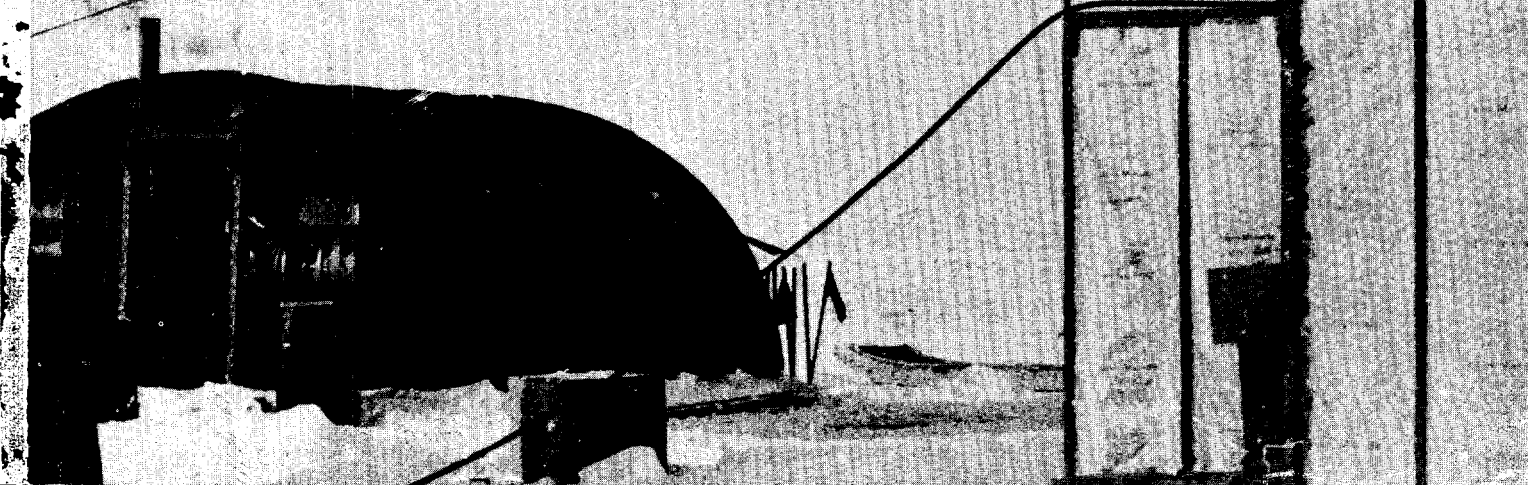


Bulletin No. 24
May 1974
NUMERICAL MODELING REPORT

AIDJEX BULLETIN

ARCTIC
ICE
DYNAMICS
JOINT
EXPERIMENT



AIDJEX BULLETIN No. 24
Numerical Modeling Report
May 1974

CONTENTS

MODELING THE PACK ICE AS AN ELASTIC-PLASTIC MATERIAL --M. D. Coon, G. A. Maykut, R. S. Pritchard, D. A. Rothrock, and A. S. Thorndike	1
STRAIN CALCULATIONS USING AIDJEX 1972 POSITION DATA --A. S. Thorndike	107
FRACTURE OF ICE SHEETS DUE TO ISOSTATIC IMBALANCE --R. T. Schwaegler	131
ABSTRACTS OF INTEREST	147
Corrections for Bulletin 23	149

*Front cover: NASA CV-990 remote sensing flight over
AIDJEX main camp during 1972 pilot study.*

*Back cover: Evergreen helicopter removing the rotating
dome which housed the CRREL laser.*

AIDJEX BULLETIN No. 24

May 1974

* * * * *

*Financial support for AIDJEX is provided by
the National Science Foundation,
the Office of Naval Research,
and other U.S. and Canadian agencies.*

* * * * *

Arctic Ice Dynamics Joint Experiment
Division of Marine Resources
University of Washington
Seattle, Washington 98105

Division of Marine Resources

UNIVERSITY OF WASHINGTON

The AIDJEX Bulletin aims to provide both a forum for discussing AIDJEX problems and a source of information pertinent to all AIDJEX participants. Issues--numbered, dated, and sometimes subtitled--contain technical material closely related to AIDJEX, informal reports on theoretical and field work, translations of relevant scientific reports, and discussions of interim AIDJEX results.

Bulletin No. 24 comprises a long report from the numerical modeling group on the present status of the AIDJEX ice model and related articles by Thorndike and by Schwaegler.

Of all the persons at AIDJEX who helped prepare this Bulletin, two deserve special editorial thanks: Drew Rothrock, whom the modeling group short-strawed into the grueling task of going over the report with the editor; and Claudia Barnard, who produced a beautiful copy from a sometimes appalling draft and often served as the editor's editor.

Any correspondence concerning the Bulletin should be addressed to

*Alma Johnson, Editor
AIDJEX Bulletin
4059 Roosevelt Way N.E.
Seattle, Washington 98105*

MODELING THE PACK ICE AS AN ELASTIC-PLASTIC MATERIAL

by

M. D. Coon, G. A. Maykut, R. S. Pritchard,
D. A. Rothrock, and A. S. Thorndike
Arctic Ice Dynamics Joint Experiment
University of Washington
Seattle, Washington 98105

ABSTRACT

A model of the motion of drifting pack ice in the Arctic Ocean is presented, treating explicitly, if not with consistent rigor, the growth and melt rates of the ice, the formation of leads and pressure ridges, and a mechanical response which is elastic at low stress levels and plastic at some higher, critical state of stress. The strength of the ice is determined by its thickness distribution, and therefore varies because of both thermal and mechanical effects. To examine the behavior of the model, several artificial calculations were made by specifying the strain rate history of a single element of pack ice and solving for the ice thickness distribution and the states of stress in the ice. This paper--properly viewed as a progress report--identifies many details in the model that require further study, but concludes that the underlying physical assumptions will do.

OUTLINE

1	INTRODUCTION	3
2	ICE THICKNESS DISTRIBUTION	11
2.1	Definitions	11
2.2	The Basic Equation	14
2.3	The Redistribution Function	16
2.3.1	The ridging mode, W_r	
2.3.2	Redistribution of ice under an arbitrary strain rate	
2.4	Important Integrals	28
3	THE ELASTIC-PLASTIC CONSTITUTIVE LAW	30
3.1	The Rationale for an Elastic-Plastic Model	30
3.2	The Basic Equations	33
3.3	An Energy Relation Between the Yield Function and the Redistribution Function	39
3.4	Possible Shapes of the Yield Curve	42
3.5	The Yield Strength p^* --Hardening and Weakening of the Material	44
3.6	Drucker's Postulate and the Present Theory	46
4	A COMPLETE MODEL FOR MASS AND MOMENTUM	48
4.1	The Governing Equations	48
4.2	Thermodynamic Ice Growth	51
4.2.1	Moderately thick ice	
4.2.2	Thin ice	
4.2.3	Thick ice	
4.3	The Redistribution Function	57
4.4	The Yield Curve	59
5	THE RESPONSE OF AN ELEMENT OF PACK ICE TO SPECIFIED DEFORMATIONS	60
5.1	Introduction	60
5.2	Thermodynamics Only	61
5.3	The Isotropic Case	67
5.3.1	Diverging motion	
5.3.2	Converging motion	
5.3.3	Changes in potential energy	
5.3.4	Some limitations of the isotropic cases	
5.4	The Uniaxial Case	80
5.4.1	$0 < t < 7$ days	
5.4.2	$7 < t < 8$ days	
5.4.3	$8 < t < 10$ days	
5.4.4	$t > 10$ days	
5.5	The Case of Pure Shear	85
5.6	1972 AIDJEX Pilot Study Data	88
6	DISCUSSION	93
6.1	Summary	93
6.2	Conclusions	94
6.3	Recommendations	96
	Acknowledgment	
	APPENDIX A	98
	APPENDIX B	100
	REFERENCES	103

1. INTRODUCTION

The AIDJEX Modeling Group is developing a mathematical model to describe the motion of arctic pack ice. The model is based on the physical principles of conservation of momentum, mass, and energy, and on certain known or postulated properties of the pack ice. Of these properties, generically referred to as "constitutive properties," the most important is the assumed elastic-plastic mechanical behavior.

The pack ice is represented as a continuum on length scales of 100 km or longer. On shorter scales, the microstructure of the pack becomes important and the necessary assumptions about the continuity and differentiability of field variables may no longer hold. An element of the continuum, then, has typical dimensions of 100 km by 100 km, and we do not ask that the system of equations resolve any smaller-scale phenomena. This paper investigates the properties of such an element of material by considering the behavior and composition of the ice inside the element.

The model is intended to resolve time scales of no less than one day. This limit reflects the quality and quantity of the input data more than it does any physical restriction. Data to drive and to test the model will be collected during the main 1975-1976 AIDJEX field experiment.

Independent variables in the system of equations are position \underline{x} , time t , and an ice thickness h . It is important neither to confuse the independent variable h with the vertical coordinate z , nor to think that h is dependent on \underline{x} and t . The actual thickness of the ice at any point is denoted by $\zeta(\underline{x}, t)$. The treatment is two-dimensional in the sense that the vertical coordinate never appears. We justify this treatment on the basis of the great difference between horizontal scales (1000 km) and vertical scales (10 m) for sea ice; the great difference in horizontal velocities (1 cm/sec) and vertical velocities (10^{-5} cm/sec); and the field observation that horizontal velocities are constant throughout the thickness of any particular piece of ice.

Dependent variables in the model are the ice velocity $\underline{v}(\underline{x}, t)$, the stress resultant $\sigma(\underline{x}, t)$, and a function $G(h, \underline{x}, t)$ which determines the state

of the ice within the element. Called the ice thickness distribution, G gives the fractional area of ice thinner than h in a 100 km element of material at \mathbf{x} at time t . G determines the state of the ice in the sense that all properties of an element--its strength, its mean thickness, and its potential energy per unit area--are written as functionals of G . Of course, the thickness distribution of the ice is continually changing in response to thermodynamic effects which, by freezing and melting, alter the thickness of the ice, and in response to mechanical effects which rearrange existing ice to form pressure ridges and open leads. The darker grey levels in Figure 1.1 correspond to thinner ice formed thermodynamically following a recent local opening of the ice pack. At present, the model parameterizes the thermodynamics through a growth rate function $f(h,t)$ specified in section 4.2. The treatment of the mechanical processes that form ridges and leads is more elaborate but is based on scanty field observations. These ideas are all discussed in section 2, where the governing equation for the ice thickness distribution is presented.

Looking at the microstructure of a typical 100 km element, we argue that pack ice should be modeled as an elastic-plastic material. Our image of the ice on this small scale is of a densely fractured material (see Fig. 1.2). Enough cracks are formed by processes not considered in this model (such as thermal cracking and uneven isostatic loading) that we ignore how cracks are formed and just assume they exist independent of the motions we are describing. Deformation may occur in the ice cover by relative motions at the cracks, but the ice between cracks is rigid. Relative motion at a crack may result in three types of local deformation: the crack can open to form a lead; it can close to eliminate a lead and perhaps form a pressure ridge; and, at the same time, it can shear without forming anything. The strongest argument, then, for a plastic model is that, despite rather smooth variations in the atmospheric and oceanic forcing fields, local events such as ridging and the formation of leads are known to happen sporadically, as though a critical stress state in the ice must be reached before deformation can occur. The major part of the work expended in building a pressure ridge appears to go into potential energy--this energy cannot be recovered. Furthermore, assuming that the shape of a ridge is

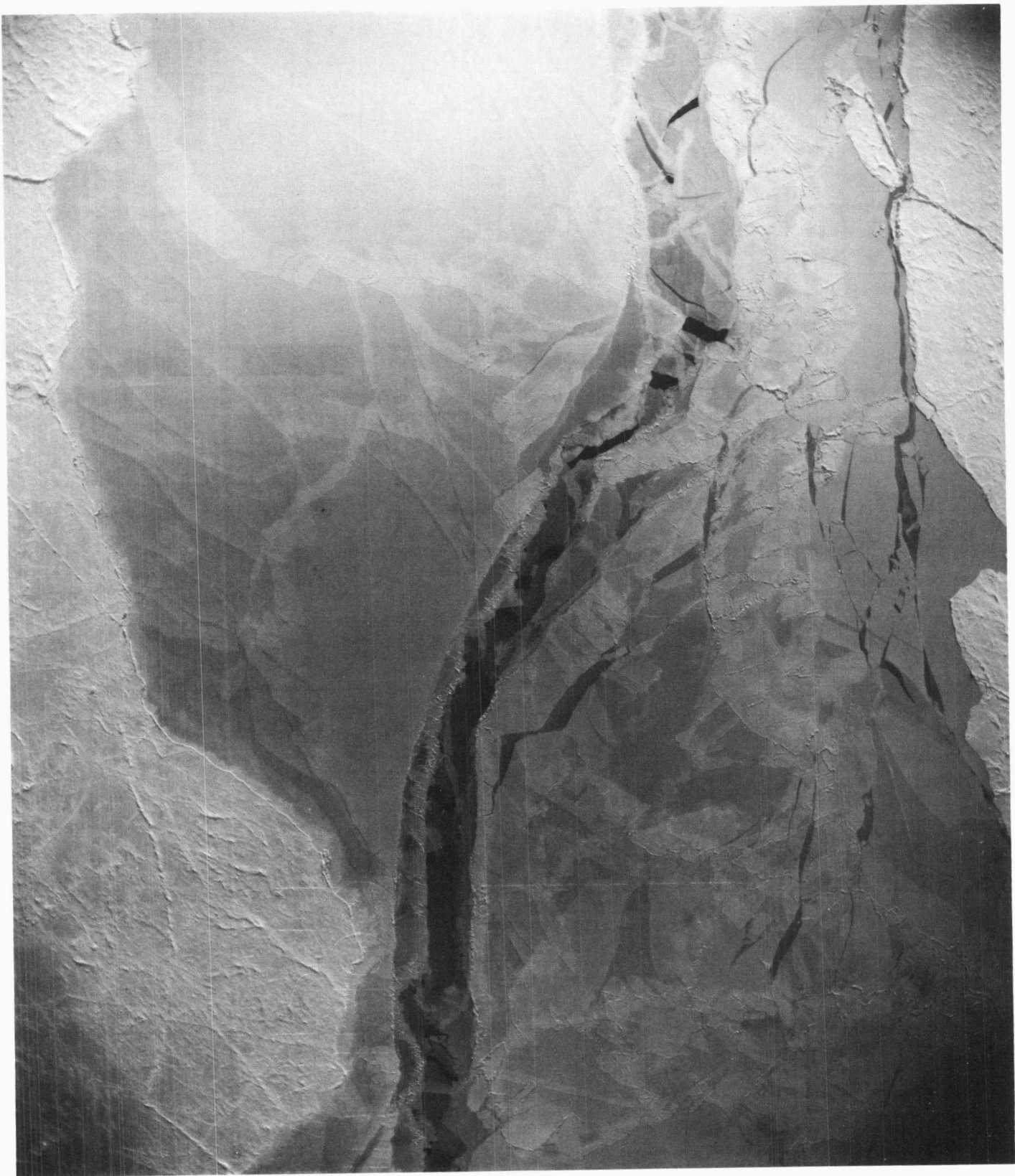


Fig. 1.1. NAVOCEANO photograph taken from 30,000 ft during the 1972 AIDJEX pilot study. The frame shows a lead that has frozen, partially closed, and opened again. Ice within the lead has rafted at many spots. Full scale is about 15 km.

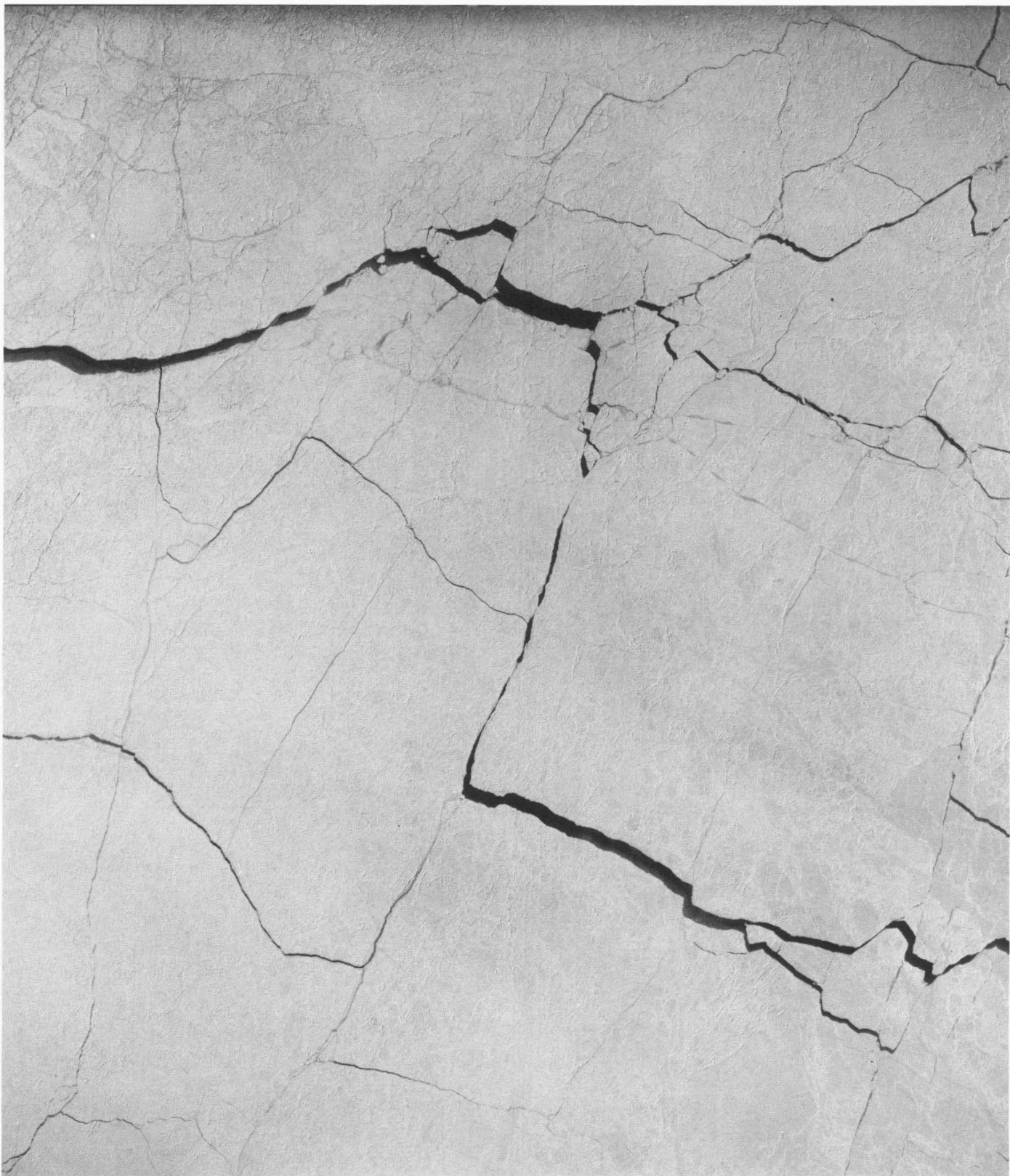


Fig. 1.2. NASA CV-990 photograph taken from 30,000 ft during the 1972 AIDJEX pilot study. The dark lines are cracks where open water or thin ice is exposed. Full scale is about 20 km.

independent of the rate at which the ridging occurred, the work done is also rate independent. A final argument for plastic behavior invokes a compelling visual analogy between pack ice (Fig. 1.3) and such granular materials as soils, which have been modeled successfully as a plastic. This analogy, together with notions of a critical stress, nonrecoverable energy dissipation, and rate-independence, supports a plastic treatment. At stresses below the critical level the ice is assumed to behave elastically. The development of the elastic-plastic equations is given in section 3.

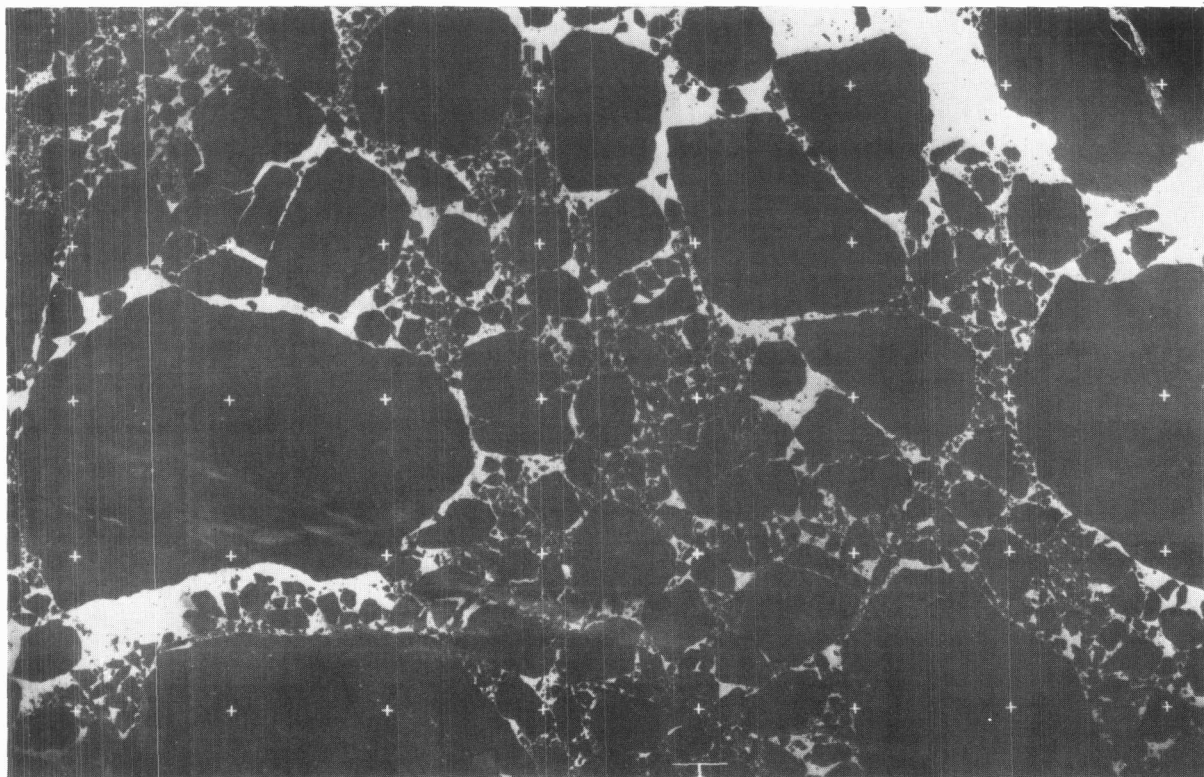


Fig. 1.3. An image of sea ice constructed from signals received from the ERTS RBV sensor during August 1972. In this negative format, the dark areas are ice, the bright areas are open water. The frame is about 50×100 km.

The set of equations for the entire model is summarized in section 4, including the special forms of the thermodynamic growth function, the plastic yield criterion, the elastic moduli, and the parameterization of pressure ridging.

Section 5 contains the results of a sequence of calculations which solve, not the full set of equations given in section 4.1, but a reduced set missing the momentum equation. A "zero-dimensional" problem is addressed by assuming a strain-rate and solving for the thickness distribution and for the state of stress using the equation for $G(h,t)$ and the elastic-plastic constitutive law. These "constrained motion" tests were run using artificial data for the motion--isotropic strain rate, uniaxial strain rate, and pure shear--and using real strain rate data from the 1972 AIDJEX pilot study.

Section 6 summarizes the major ideas of the report and contains recommendations for future work.

To our knowledge, pack ice has never been treated as an elastic-plastic material. In the models that have actually been used for calculations, and in constitutive laws that have been proposed but not used in calculations, the emphasis has been placed on finding an appropriate viscous behavior. The most complete viscous model was presented by Doronin [1970]; it treats the ice as a cavitating fluid with a shear viscosity. An intrinsic property of any viscous model is that the state of stress depends on the rate at which deformations proceed. Here the present treatment differs fundamentally, because the state of stress in anelastic-plastic material is assumed to be independent of the rate of deformation.

An important similarity between the present and previous work is that the material behavior is allowed to depend on the state of the ice, although there has been no agreement as to how the state of the ice should be measured. Evans [1970], for example, wrote a constitutive equation in which the viscosity depended on the amount of strain an element had undergone since some initial state. Glen [1970], on the other hand, proposed that the viscosity depends on the strain rate. The shear viscosity in Doronin's model depended on the compactness of the ice. Here, we present a theory in which the elastic and plastic parameters depend on the ice thickness distribution. The thickness distribution summarizes the thermal and mechanical history of an element; we believe it characterizes the state of the ice.

A thorough comparison of the present model with previous models will be attempted later when our perspective on the present work is better. The

important differences between this theory and previous ones appear to be that:

1. We have inferred the large-scale mechanical response of the ice on the basis of small-scale phenomena such as ridging and cracking; this approach has led us to view pack ice as an elastic-plastic material.
2. We have considered the variations in ice thickness, rather than ignoring them entirely or treating only the percentage of open water, as previous modelers have done.

A Note to the Reader

During the preparation of this report, many attempts were made to define the intended audience. We have tried to make ideas intelligible both to readers who know some mechanics but not much about ice and to those who know sea ice but not mechanics. Many of the arguments could have been made more concisely and more elegantly had the intended audience been less general. We encourage a vigorous review of the validity of our arguments and of the manner in which we have presented them.

Different readers may choose to read the document differently. For many readers, the details of sections 2, 3, 4, and 5 can be omitted on a first reading. Sections 2, 3, and 4.2 can be read in any order, but section 5 and parts of section 4 are contingent on all the previous material. The introductory material to the various sections is somewhat overlapping, making it easier to read each section in a separate sitting.

2. ICE THICKNESS DISTRIBUTION

Conservation of mass is often represented by an equation describing changes in the mass density of a body. The two-dimensional model presented in this report requires that we treat this fundamental law of physics in greater detail than heretofore attempted for two-dimensional models.

We take the view here that, on a scale of tens of kilometers, sea ice is a mixture of constituents defined only by their thickness, and that the bulk thermal and mechanical properties of the ice are determined by the properties of each constituent and by its abundance measured by the area it covers. Although in practice we may wish only to resolve a few discrete constituents, the mathematical formulation is cleaner if we consider a continuous range of thickness.

2.1 Definitions

We define the ice thickness distribution $G(h, t, R)$ as the fractional area in a region R at time t covered by ice thinner than h . G is defined for all h and t , and for all R that have some area in the usual sense. For a given region, G is constructed by determining the function $\zeta(x, t) =$ thickness of the ice at t and at the point x in R . Then, using the Heaviside function

$$H(\gamma) = \begin{cases} 1, & \gamma > 0 \\ 0, & \gamma \leq 0 \end{cases}, \quad (2.1)$$

$$G(h, t, R) \equiv \frac{1}{R} \int_{x \in R} H(h - \zeta) da. \quad (2.2)$$

It will be useful to extend this definition to apply at a point. Letting the region collapse to a point, though, is not acceptable: this would force $G(h, t, R=(x))$ to be $H(h - \zeta(x, t))$, a trivial distribution function. For convenience we might choose circular neighborhoods of radius 100 km, say, centered at x . Because the dependence of G on position is not important to this paper, the notation $G(h, t, x)$ will usually be contracted to $G(h, t)$.

The function $\zeta(x, t)$ is non-negative and bounded by some thickness h_{\max} . It takes a value of zero when the point x is covered by ice of zero thickness, that is, open water. Because ζ is non-negative, $G(0, t)$ is always zero, even when there is a finite area of open water. This follows from eq. 2.2 and the strict inequality in eq. 2.1. For with $h = 0$ in the integrand in eq. 2.2, the integrand is zero, both at points where $\zeta = 0$ and at points where $\zeta > 0$. Other immediate consequences of the definitions, proven in a similar manner, are that

1. $G(h, t)$ is monotonic increasing in h .
2. $G(h, t) = 0$ for $h \leq 0$.
3. $G(h, t) = 1$ for $h > h_{\max}$.
4. $G(h, t)$ can be discontinuous in h , with steps corresponding to finite areas of some particular thickness.
5. If G has a discontinuity at a point h_1 , then

$$\lim_{|\Delta| \rightarrow 0} G(h_1 - |\Delta|, t) = G(h_1, t) \neq \lim_{|\Delta| \rightarrow 0} G(h_1 + |\Delta|, t).$$

(See Fig. 2.1.)

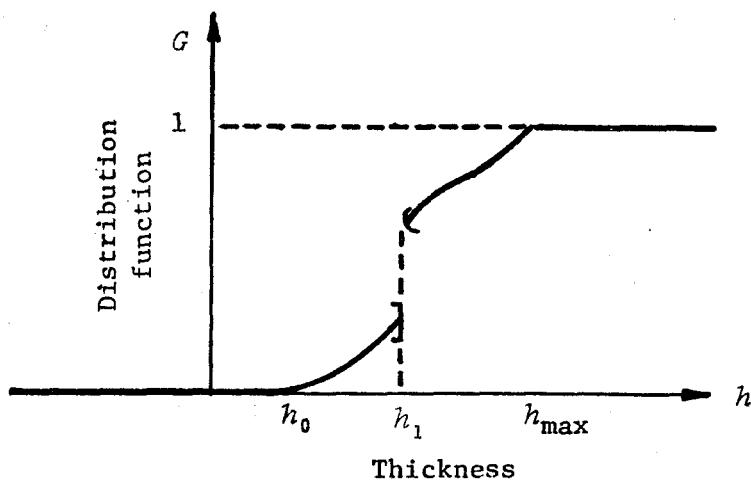


Fig. 2.1. A possible ice thickness distribution, showing a finite area of ice of thickness exactly equal to h_1 .

The upper bound of h_{\max} on ζ is important only to force $G(h, t, R(x))$ to behave well as a function of x and, incidentally, to set finite bounds on the calculations of G ; ζ need never actually achieve a value of h_{\max} .

Our formulation could have included the density of the ice and defined a distribution of mass per unit area. At this writing, however, thickness seems to be just as useful for describing the thermodynamics and the dynamic behavior of the ice. If at some time it becomes important to include density effects--such as when, as suggested by Parmerter and Coon [1973], the presence of voids reduces the effective density of ridges--this can be done within the framework of the present ice thickness distribution theory. For the present, we take the density of the ice to be a constant.

At times, it will be more natural to refer to the ice probability density function $g(h, t)$, which is related to G by

$$g(h, t) = \lim_{|\Delta| \rightarrow 0} \frac{G(h+|\Delta|, t) - G(h, t)}{|\Delta|}. \quad (2.3)$$

It is important to remember, but easy to forget, that $g(h, t)$, being a probability density, only makes sense in an integral form; i.e.,

$$g(h_1, t) dh \approx \int_{h_1}^{h_1 + dh} g(\xi, t) d\xi = G(h_1 + dh, t) - G(h_1, t) \quad (2.4)$$

which is the fractional area of ice with thickness between h_1 and $h_1 + dh$. If h_1 happens to be a point of discontinuity in $G(h, t)$, then $g(h_1, t)$ is a delta function times the magnitude of the discontinuity, and the integral $\int_{h_1}^{h_1 + dh} g(\xi, t) d\xi$ would include the entire contribution from the delta function.

When interpreting $G(h, t)$ and $g(h, t)$ as a cumulative probability function and its probability density function, we should think of h as the random variable and t as a parameter indicating that the distribution may vary in time. If one adopts the probabilistic point of view, then G and g may be well defined at a point (x, t) , but one must rewrite ζ as a random variable and take the integral in eq. 2.2 over an ensemble rather than over a geographical region. Both points of view are valid and useful; for the

most part, however, we will confine ourselves to the area interpretations of these functions.

2.2 The Basic Equation

The basic equation governing the ice thickness distribution was written by Thorndike and Maykut [1973] as

$$\frac{\partial G}{\partial t} + f \frac{\partial G}{\partial h} = (W - G) \operatorname{div} \underline{v}. \quad (2.5)$$

In this discussion, we will use a slightly different form following the notation of Rothrock [1974a]:

$$\frac{\partial G}{\partial t} + f \frac{\partial G}{\partial h} = -\underline{v} \cdot \operatorname{grad} G + (\Psi - G \operatorname{div} \underline{v}). \quad (2.6)$$

Here the term $W \operatorname{div} \underline{v}$ has been replaced by Ψ . The treatment in Thorndike and Maykut [1973] considered $G(h, t, R)$ where R is a Lagrangian region moving with the pack ice; this made easier the development of the basic equation. When an Eulerian region is considered, as is implicit in the definition above of the regions $R(\underline{x})$, it is necessary to add the advection term, $-\underline{v} \cdot \operatorname{grad} G$, to the right-hand side of eq. 2.5.

The distinction between Eulerian and Lagrangian approaches is conceptually important, but since in this paper $\operatorname{grad} G$ is always zero, the distinction has no practical importance. The Eulerian time derivative will be denoted by $\partial/\partial t$ and the Lagrangian derivative by $d/dt = (\partial/\partial t + \underline{v} \cdot \operatorname{grad})$.

The function $f = f(h, t, \underline{x})$ in eq. 2.6 describes the growth rate of ice of thickness h due to thermodynamic processes. Under the action of thermodynamics, some of the ice within R may grow thicker and some may become thinner; and thus the composition of the mixture will change. Equation 2.6 accounts for this by the balance $\partial G/\partial t = -f \partial G/\partial h +$ additional terms.

Neglecting the additional terms in eq. 2.6, f will cause G to move laterally in h , and so for fixed h the change in G will be given by $\Delta G = -f \Delta t \frac{\partial G}{\partial h}$. (See Fig. 2.2.) In this sense, f is an h velocity analogous

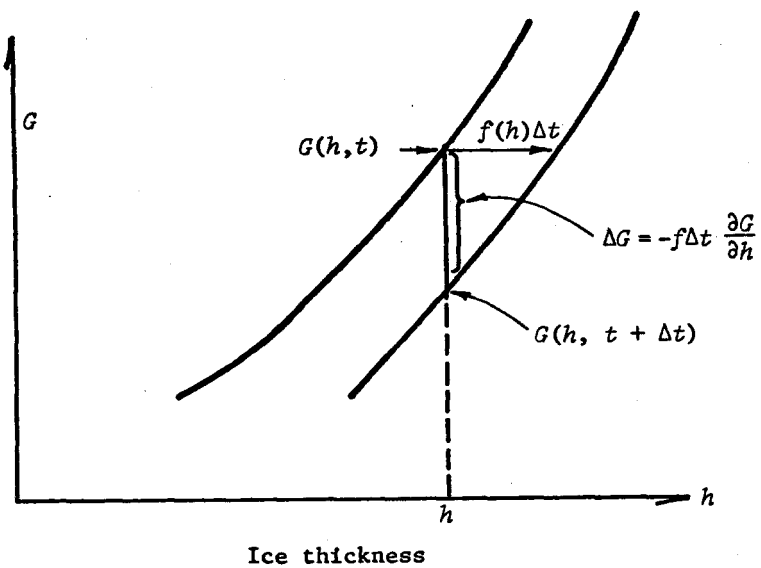


Fig. 2.2. The thickness distribution, G , changes thermodynamically because the ice growth rates, f , move the curve along the h -axis.

to the spatial velocity \mathbf{v} , and the term $-f \frac{\partial G}{\partial h}$ is analogous to the advection $-\mathbf{v} \cdot \nabla G$. Since f does vary in h , different parts of the function $G(h)$ will move with different speeds and even in different directions. On a time scale of years in the Central Arctic, f is positive for ice thinner than about 3 m and negative for ice thicker than about 3 m. This implies that in the long run, and under the influence of f alone, all of the ice would approach a thickness of about 3 meters.

Mathematically, f has an important position in the basic equation. Curves in (h, t) space which everywhere have slope $f(h, t)$ are called characteristics of the equation, and have the property that G satisfies an ordinary differential equation along each of these lines. A set of characteristics for G is plotted in Figures 2.3 and 2.4. A method for solving eq. 2.6, using characteristics, is given in Appendix A.

A characteristic can be interpreted as the path in (h, t) space that a piece of ice would follow under the influence of thermodynamic processes only. From the figure it is clear that, since all ice originates with zero thickness, there is no thermodynamic process by which a piece of ice can ever achieve a thickness greater than 3 meters. All ice thicker than 3 meters

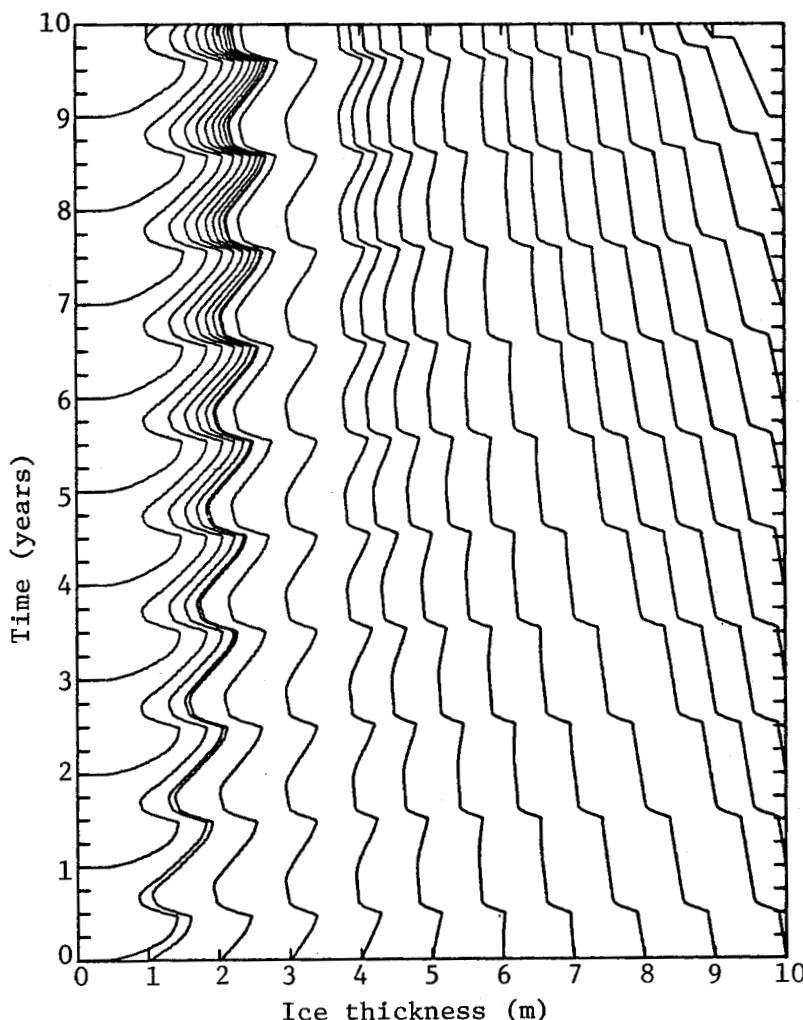


Fig. 2.3. The characteristics of the basic equation are lines in (h, t) space such that $dh/dt = f(h, t)$. A detail of the characteristics for $0 < t < 1$ year and $0 < h < 2$ meters is given in Figure 2.4.

must have been formed by some mechanical process and will in time ablate down to 3 meters.

2.3 The Redistribution Function Ψ

The terms $\Psi - G \operatorname{div} \mathcal{Y}$ in eq. 2.6 describe the modification of G due to the deformation of the ice pack. Ψ depends on h , on the strain rate ξ , and on the thickness distribution $G(h')$ at all thicknesses h' ; thus Ψ is a functional of G . In the absence of thermodynamics, and neglecting advection,

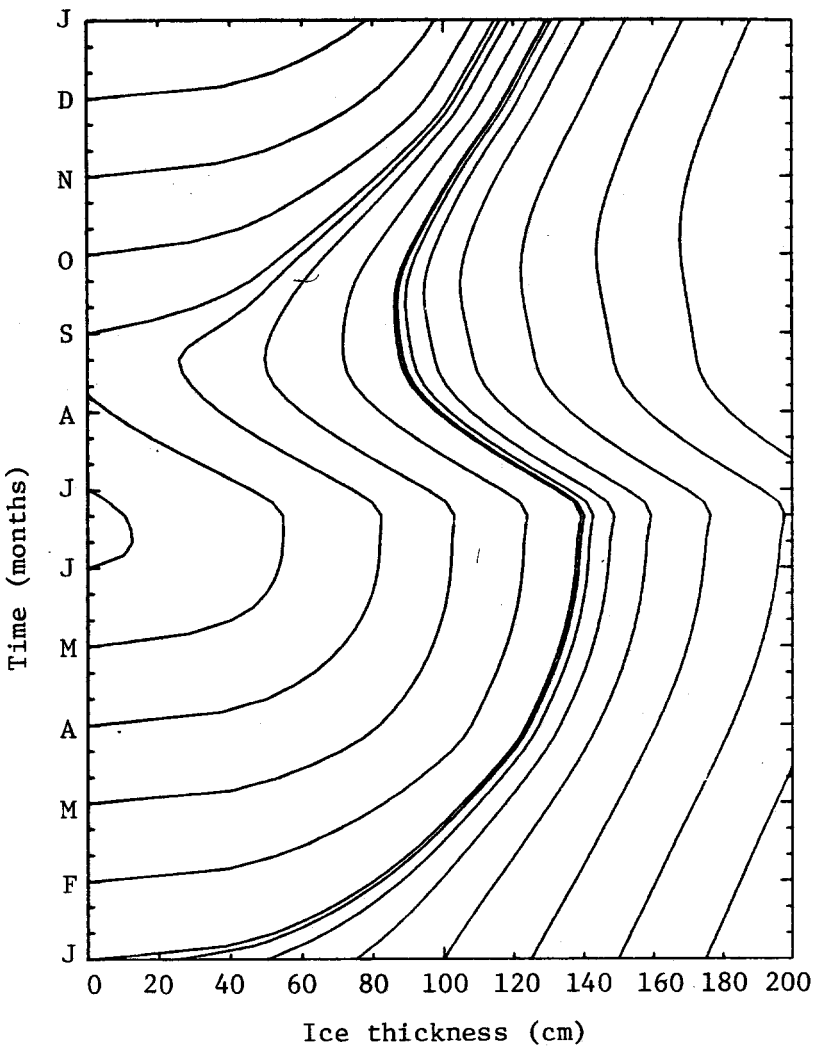


Fig. 2.4. A detail of the characteristics for thin ice.
A positive slope implies that the ice is growing thicker;
a negative slope implies that the ice is ablating.

the equation reduces to $\partial G / \partial t = \Psi - G \operatorname{div} \vec{v}$. These terms must be taken together; balancing $\partial G / \partial t$ with either Ψ or $-G \operatorname{div} \vec{v}$ alone leads to contradictions. Since $G(h > h_{\max}, t)$ is always unity, its time derivative is zero; and we note that $\Psi(h > h_{\max})$ must equal $\operatorname{div} \vec{v}$, to conserve area. During an episode of deformation there will be, in general, a flux of area across the boundary of R , as described by $-G \operatorname{div} \vec{v}$, but since the total area of R is fixed, Ψ must compensate for any loss or gain of area caused by $-G \operatorname{div} \vec{v}$.

When ice is diverging, for example, the decreasing coverage of all constituents will be compensated for as Ψ causes the area of open water $G(0^+, t)$ to increase. This is accomplished by a step in Ψ at $h = 0^+$, or, using the Heaviside function, $\Psi = \operatorname{div} \underline{\gamma} H(h)$. (Figure 2.5.) Because of the cumulative nature of Ψ , increments $\Delta\Psi = \Psi(h_2) - \Psi(h_1)$ correspond to changes in area of ice with thickness $h_1 < h \leq h_2$. In pure divergence the only increment, $\Delta\Psi$, occurs at $h = 0$. In the more difficult case, when the pack ice is converging ($\operatorname{div} \underline{\gamma} < 0$), the term $-G \operatorname{div} \underline{\gamma}$ causes a flux of ice into R , and Ψ must make room for this new ice by rearranging the ice already in R so that it occupies less area. This is accomplished by taking thin ice and building thick pressure ridges so that the area covered by thin ice is decreased while the area covered by thick ice is increased. The net effect of Ψ is still $\Psi(h > h_{\max}, t) = \operatorname{div} \underline{\gamma}$; so that through the combined action of Ψ and $-G \operatorname{div} \underline{\gamma}$, G still accounts for the entire area in R . We make the simplest assumption that in the ridging process the volume (mass) of ice must be conserved. This is expressed by

$$\int h d\Psi = 0. \quad (2.7)$$

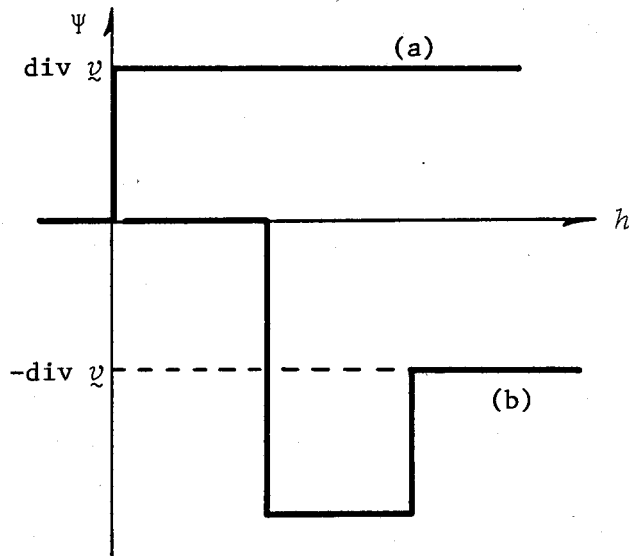


Fig. 2.5. a) In isotropic divergence, the redistribution function Ψ is a step at $h = 0^+$; $\Psi = \operatorname{div} \underline{\gamma} H(h)$. b) A possible redistribution function for isotropic convergence has a negative step of $-2 \operatorname{div} \underline{\gamma}$ at some thickness h_1 , and a positive step of $\operatorname{div} \underline{\gamma}$ at $2h_1$. This corresponds to the simple rafting model in which pressure ridges of thickness $2h_1$ are constructed out of ice of thickness h_1 .

In places we have used the notation $\int d\Psi$ where $\int_0^{h_{\max}} \frac{\partial \Psi}{\partial h} dh$ would have served just as well.

The conservation of area and conservation of volume constraints are both satisfied by the Ψ functions in Figure 2.5. Within these constraints Ψ can be selected to conform with our intuition and to simplify the formulation. For the pure divergence case, the Ψ just presented seems to be acceptable on both counts, but the redistribution process for pure convergence is more complicated and is discussed next. Having constructed a more acceptable ridging model, the treatment will be generalized in section 2.3.2 to account for effects of shear as well.

2.3.1 The Ridging Mode, W_r

In pure convergence, Ψ can be written as $|\operatorname{div} v| W_r(h)$. The ridging mode $W_r(h)$ is constructed by:

1. specifying the thickness distribution of the ice participating in the ridging,
2. specifying the rule by which the participating ice of some thickness is transformed into thicker ridged ice, in a way that conserves volume,
3. calculating the distribution of the newly ridged ice, and
4. combining the distributions 1 and 3 above, and normalizing to guarantee that $W_r(h>h_{\max}) = -1$, thus conserving area.

The formulation is general enough to account for all of the possible redistributors, Ψ , which have been suggested by Thorndike and Maykut [1973] and Rothrock [1974b]. In this section we develop these four steps and then present several examples. The development requires that we discuss a two-dimensional space spanned by two thickness axes h_1 and h_2 , where h_1 refers to the ice participating in the ridging and h_2 to the resulting deformed ice.

The participating ice has a distribution $A(h_1)$; i.e., $A(h_1)$ is the area of ice thinner than h_1 which is participating instantaneously in the deformation. Clearly A is related to G , since it would not make sense to have ice of some particular thickness participate in ridging if G told us

that no ice of that thickness existed. So a universal function $B(G)$ is postulated such that

$$B(G) = \begin{cases} 0 & \text{when } G = 0, \\ \text{monotonic increasing} & \text{when } 0 \leq G \leq G^*, \\ 1 & \text{when } G = G^*. \end{cases} \quad (2.8)$$

The function $A(h_1)$ is defined then as

$$A(h_1) = B(G(h_1)). \quad (2.9)$$

In this formulation, only the thinnest G^* of the ice by area participates in the ridging. (We take G^* to be 0.15 in sections 4 and 5.) We define h^* , by $G(h^*) = G^*$, to be the thickest ridging ice. As G changes in time, so does h^* and so does the distribution A of ice being ridged. $B(G)$ is called the participation function.

In general, if we take a unit area of ice of thickness h_1 and make pressure ridges out of it, we would get ridged ice with a cumulative distribution of thickness $\Gamma(h_1, h_2)$; that is, $\Gamma(h_1, h_2)$ is the area of ice thinner than h_2 which is formed when a unit area of ice of thickness h_1 is used up. We assume that Γ , called the redistribution process, conserves volume:

$$\int_{h_2=0}^{h_2=\infty} h_2 d\Gamma(h_1, h_2) \Big|_{h_1=\text{constant}} = h_1. \quad (2.10)$$

The distribution of the newly ridged ice is found easily in terms of Γ and A :

$$N(h_2) = \text{area of newly ridged ice thinner than } h_2$$

$$= \int_{h_1=0}^{h_1=\infty} \Gamma(h_1, h_2) dA(h_1).$$

Since $A(h)$ refers to ice which has been transferred into different thicknesses, it represents a decrease in $G(h)$; $N(h)$, referring to newly formed ice, represents an increase. Thus

$$W_r(h) = \frac{-A(h) + N(h)}{A(h>h_{\max}) - N(h>h_{\max})} . \quad (2.11)$$

Several examples of how different ridging modes W_r may be constructed are presented here to clarify the above discussion and to relate it to redistributors discussed by Thorndike and Maykut [1973] and Rothrock [1974b].

1. Thinnest ice first, simple rafting (Thorndike and Maykut [1973, p. 37]). Here $B(G) = H(G)$, the Heaviside function. This means that only the thinnest ice actually present participates in the ridging. The redistribution process becomes a step of height 1/2 at $h_2 = 2h_1$ (Fig. 2.6):

$$\Gamma(h_1, h_2) = \frac{1}{2} H(h_2 - 2h_1) . \quad (2.12)$$

If the thinnest ice present has $h = h_0$, then

$$A(h_1) = H(h_1 - h_0) \quad (2.13)$$

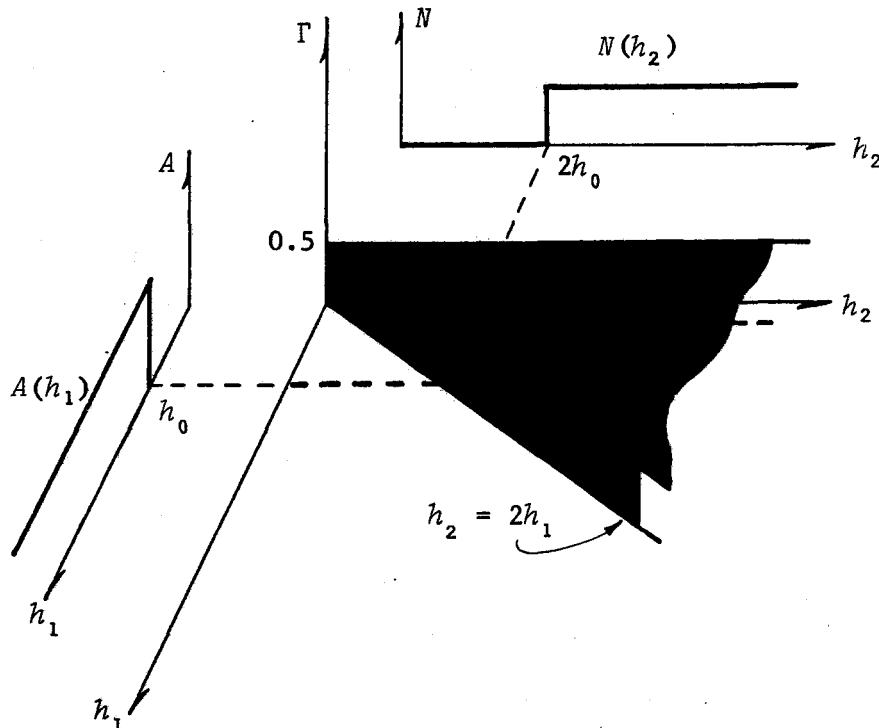


Fig. 2.6. The redistribution process for simple rafting, using the thinnest ice first participation function, is a step of magnitude 0.5 at $h_2 = 2h_1$.

and consequently

$$\begin{aligned} N(h_2) &= \int \frac{1}{2} H(h_2 - 2h_1) dH(h_1 - h_0) \\ &= \frac{1}{2} H(h_2 - 2h_0). \end{aligned} \quad (2.14)$$

$$\begin{aligned} \text{Thus } W_R(h) &= \frac{-H(h - h_0) + (1/2)H(h - 2h_0)}{+1 - 1/2} \\ &= -2H(h - h_0) + H(h - 2h_0). \quad (\text{See Fig. 2.5b.}) \end{aligned} \quad (2.15)$$

2. Thinnest ice first, uniform distribution (Fig. 2.7; Thorndike and Maykut [1973, p. 39]). As in the previous example, $B(G)$ is just $H(G)$, and $A(h)$ is $H(h - h_0)$. The redistribution process, which must satisfy eq. 2.10, is

$$\Gamma(h_1, h_2) = \begin{cases} 0 & , h_2 < h_1 , \\ \frac{2h_1(h_2 - h_1)}{h_{\max}^2 - h_1^2} & , h_1 < h_2 < h_{\max} , \text{ and} \\ \frac{2h_1}{h_{\max} + h_1} & , h_2 > h_{\max} . \end{cases} \quad (2.16)$$

So now

$$\begin{aligned} N(h_2) &= \int \frac{2h_1(h_2 - h_1)}{h_{\max}^2 - h_1^2} dH(h_1 - h_0) \\ &= \begin{cases} 0 & , h_2 < h_0 , \\ \frac{2h_0(h_2 - h_0)}{h_{\max}^2 - h_0^2} & , h_0 < h_2 < h_{\max} , \text{ and} \\ \frac{2h_0}{h_{\max} + h_0} & , h_2 > h_{\max} . \end{cases} \end{aligned}$$

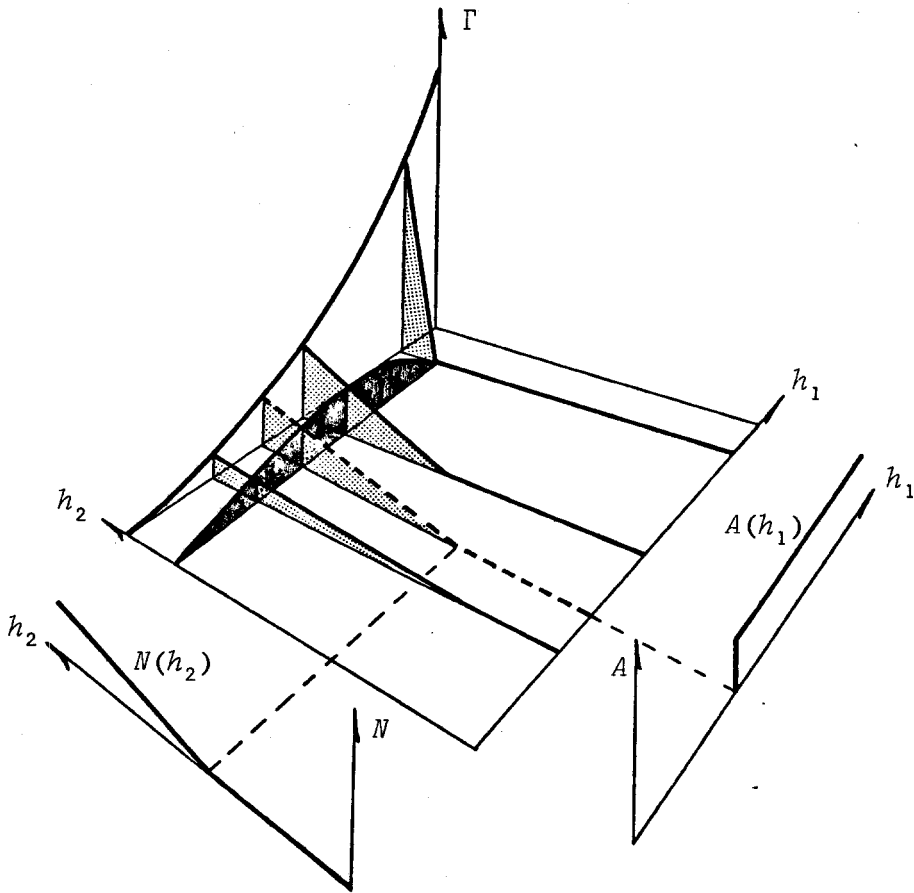


Fig. 2.7. The uniform redistribution process, using the thinnest ice first participation function. The Γ surface is zero for $h_2 \leq h_1$. For h_1 fixed, Γ increases linearly with h_2 . If h_2 is held constant, Γ first increases with h_1 reaching a maximum at some value $h_1 < h_2$, and then decreases to zero at $h_1 = h_2$. (See eq. 2.16.)

and consequently,

$$w_r(h) = \begin{cases} 0 & , h < h_0 , \\ -\frac{h_{\max} + h_0}{h_{\max} - h_0} + \frac{2h_0}{(h_{\max} - h_0)} (h - h_0) & , h_0 < h < h_{\max} , \\ -1 & , h \geq h_{\max} . \end{cases} \quad (2.17)$$

3. Relaxing the thinnest-ice-first concept but reverting to a one-to-one redistribution process (as in Rothrock [1974b]). B is some given function, so that we can generate $A(h)$. In this example, ridged ice of thickness h_2 is constructed from ice of thickness $h_1 = \hat{h}(h_2)$; we assume that \hat{h} is a monotonic increasing function. It is convenient to define the inverse mapping \tilde{h} such that $h_2 = \tilde{h}(h_1)$. The redistribution process Γ is idealized as a step at $h_2 = \tilde{h}(h_1)$, and, to satisfy volume conservation (eq. 2.10), we must have

$$\Gamma(h_1, h_2) = \frac{h_1}{\tilde{h}(h_1)} H(h_2 - \tilde{h}(h_1)). \quad (2.18)$$

Note that the redistribution process for simple rafting (eq. 2.12) occurs as a special case of eq. 2.18. (See Fig. 2.8.)

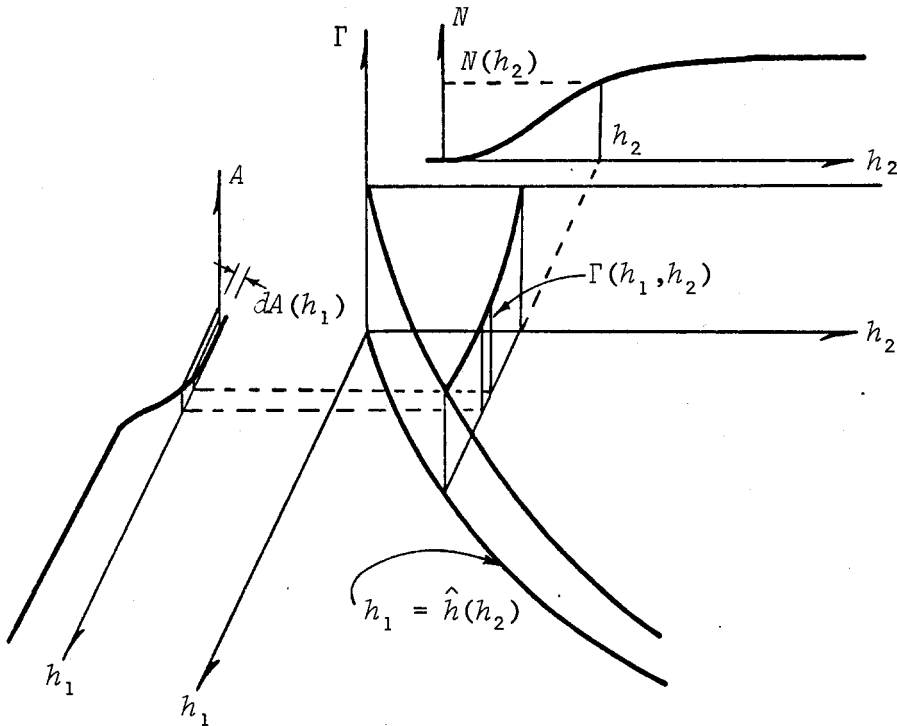


Fig. 2.8. A more general participation function, with a one-to-one ridging rule, $h_1 = \hat{h}(h_2)$. To construct $N(h_2)$, take an increment $dA(h_1)$ along the A axis and find the corresponding value of $\Gamma(h_1, h_2)$ as shown, then sum $\Gamma(h_1, h_2)dA(h_1)$ for all increments $dA(h_1)$.

To construct $N(h_2)$ we compute:

$$\begin{aligned}
 N(h_2) &= \int \frac{h_1}{\tilde{h}(h_1)} H(h_2 - \tilde{h}(h_1)) dA(h_1) \\
 &= \int_0^{h_1 = \hat{h}(h_2)} \frac{h_1}{\tilde{h}(h_1)} dA(h_1). \tag{2.19}
 \end{aligned}$$

The result in Rothrock [1974b, eq. 16] can be reproduced by differentiating $N(h_2)$ with respect to h_2 :

$$\begin{aligned}
 n(h_2) \equiv \frac{dN(h_2)}{dh_2} &= \frac{d}{dh_2} \int_0^{\hat{h}(h_2)} \frac{h_1}{\tilde{h}(h_1)} \frac{dA(h_1)}{dh} dh_1 \\
 &= \frac{d\hat{h}(h_2)}{dh_2} \frac{\hat{h}(h_2)}{\tilde{h}(\hat{h}(h_2))} a(\hat{h}(h_2)) = \hat{h}' \frac{\hat{h}}{h_2} a(\hat{h}(h_2)). \tag{2.20}
 \end{aligned}$$

The participation function B is a fixed function of G , and the redistribution process Γ is a fixed surface in (h_1, h_2) space. As G changes, according to eq. 2.6, the A distribution participating in the deformation will change, and consequently different portions of the surface Γ will be used, but the underlying process itself does not change. The three examples above simply review forms of $B(G)$ and $\Gamma(h_1, h_2)$ hypothesized in earlier papers; choosing one of these forms on the basis of our present scant knowledge is highly speculative. In section 5 we report on some calculations done using the B and Γ of the third example. That a distribution of thin ice participates in ridging seems physically reasonable to us and provides smoother computation properties. The one-to-one assumption for the redistribution process is very crude, but a fancier rule would be hard to justify. A physical argument for the one-to-one rule is given in section 4.3.

2.3.2 Redistribution of Ice Under an Arbitrary Strain Rate

The redistributor Ψ is a function of the strain rate tensor. We assume that the ice is isotropic, so that Ψ depends only on two invariants of the strain rate tensor: $\dot{\varepsilon}_I$, the sum of the principal values, being the divergence of velocity; and $\dot{\varepsilon}_{II}$, the difference between the principal values, being related to the shearing.

At this time we can make only qualitative and intuitive arguments for how Ψ depends on the strain rate invariants (except when $\dot{\varepsilon}_I > 0$ and $\dot{\varepsilon}_{II} = 0$, about which we are more confident). That Ψ is active, even during pure shear when $\dot{\varepsilon}_I = \text{div } \boldsymbol{\varphi} = 0$, is a consequence of the following reasoning. The pack ice is partitioned into discrete quasi-rigid floes by a dense network of irregular, jagged cracks (Fig. 1.2). When shearing occurs, the displacement vector at any point along a crack may have any orientation with respect to the crack, depending on which way the crack trends locally. In Figure 2.9 we imagine different segments of cracks opening, closing, and shearing, all in response to the same applied strain rate. The ice thickness

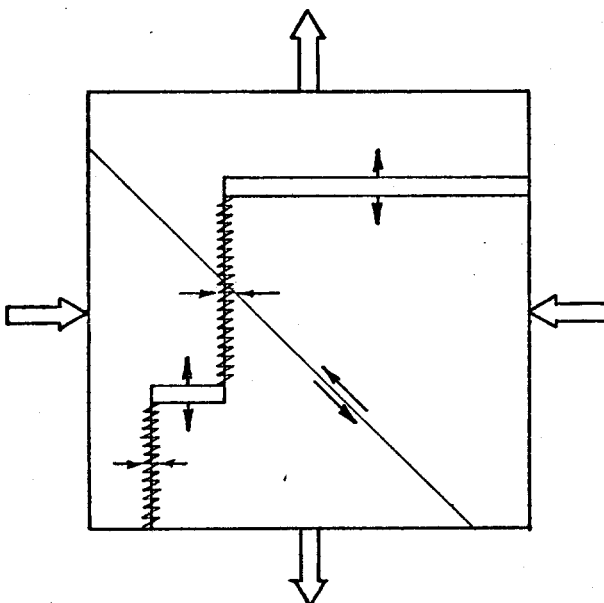


Fig. 2.9. A possible configuration of cracks in an element of pack ice. To achieve the deformation shown (pure shear) some cracks open, some close forming pressure ridges, and some just slip.

distribution is not affected by components of the displacement parallel to the crack, but the components normal to the crack will cause local deformation and redistribution analogous to the ridging and opening cases treated above. The deformation indicated in Figure 2.9 is pure shear, and still there are some cracks opening and some closing.

The conclusion is that shearing can alter the thickness distribution, but that it does so by exercising the same ridging and opening modes involved in pure convergence and pure divergence. In general, then, the redistributor is the sum of two modes:

$$\Psi = \sqrt{\dot{\varepsilon}_I^2 + \dot{\varepsilon}_{II}^2} \{ \alpha_o W_o + \alpha_r W_r \} \quad (2.21)$$

where $W_o = H(h)$ (the Heaviside function) and W_r are the opening and ridging modes and depend only on h and G . The coefficients α_o and α_r depend only on θ , which is defined as $\tan^{-1} (\dot{\varepsilon}_{II}/\dot{\varepsilon}_I)$ and is a measure of the relative rates of shearing and divergence.

The factor $\sqrt{\dot{\varepsilon}_I^2 + \dot{\varepsilon}_{II}^2}$ is the rate at which a given deformation occurs. The manner in which Ψ depends on h is assumed to be affected by θ , but not by the rate of deformation.

To reproduce pure opening during pure divergence, $\alpha_o(\theta=0)$ must equal 1, and $\alpha_r(\theta=0)$ must be zero. Similarly, $\alpha_o(\pi) = 0$ and $\alpha_r(\pi) = 1$ ensure that pure ridging is retained in pure convergence. In fact, to preserve area conservation ($\int d\Psi = \text{div } \underline{\nu}$), we require

$$\alpha_o(\theta) - \alpha_r(\theta) = \cos \theta \quad (2.22)$$

so that only one of α_o and α_r can be regarded as arbitrary. (To verify this, recall $\int dW_o = 1$, $\int dW_r = -1$, and

$$\frac{\text{div } \underline{\nu}}{\sqrt{\dot{\varepsilon}_I^2 + \dot{\varepsilon}_{II}^2}} = \cos \theta.$$

Then insert eq. 2.21 into $\int d\Psi = \text{div } \underline{\nu}$.)

2.4 Important Integrals

In this section we examine expressions for the volume V of ice per unit area and the isostatic potential energy PE per unit area in terms of integrals of h and G . Since V and PE will be functions only of time and since they have ready physical significance, they are useful for summarizing the behavior of G in time.

At a fixed time, G is monotonic in h , so it is equivalent to consider either $G = G(h)$ or $h = h(G)$; and for the most part the choice of which variable is independent and which dependent will be made only to simplify the integrals. Thus the forms

$$G(h) = \int_0^h g(\xi) d\xi = \int_0^h \frac{\partial G}{\partial \xi} d\xi = \int_0^{G(h)} dG \quad (2.23)$$

are all equivalent. The volume $V(t)$ and potential energy $PE(t)$ (both per unit area) are given by

$$V = \int_0^1 h dG \quad (2.24)$$

and

$$PE = c \int_0^1 h^2 dG \quad (2.25)$$

where the constant c depends on the densities of sea ice and of water, ρ_{ice} and ρ_{water} , and on the acceleration of gravity \hat{g} in the form (from Rothrock [1974a])

$$c = \frac{1}{2} \hat{g} \rho_{ice} (\rho_{water} - \rho_{ice}) \rho_{water} .$$

In probability jargon, the volume and potential energy appear as the first and second moments of the distribution function G .

We can now manipulate the basic equation 2.6 and the integrals 2.24 and 2.25 to get equations that describe the rates of change of the volume and the potential energy

$$\frac{dV}{dt} = \int f dG - V \operatorname{div} \tilde{v} \quad (2.26)$$

and

$$\frac{dPE}{dt} = c \int 2fh dG + c \int h^2 d\Psi - PE \operatorname{div} \tilde{v}. \quad (2.27)$$

The thermodynamic terms show how the volume (or average thickness) and the potential energy are changed due to ice growth and melt. The terms containing $\operatorname{div} \tilde{v}$ account for the change in area of the region occupied by a fixed set of material particles. The area increases during divergence, thereby reducing the volume and the potential energy per unit area; the area decreases during convergence, increasing these quantities. The term containing Ψ shows that the redistribution of ice from thin ice to thick effects a change in the potential energy per unit area. There is no change in volume due to Ψ . Recalling that Ψ is a composite of two modes of deformation, W_o and W_r , we should note that the contribution from W_o (the opening mode) is always zero because its only increment occurs at $h = 0$.

The changes in energy effected by redistributing the ice represent mechanical work and will be related in the next section to the yield stress of the pack ice.

3. THE ELASTIC-PLASTIC CONSTITUTIVE LAW

3.1 The Rationale for an Elastic-Plastic Model

We argue here that the large-scale mechanical behavior of pack ice can be represented by an elastic-plastic model. Then we relate the plastic behavior to the ice thickness distribution by assuming that all of the energy dissipated through plastic deformation appears as an increase in the potential energy of the ice as described by the redistribution function.

The concept of a yield stress, or critical stress, is central to an understanding of elastic-plastic behavior. When the stress state in a one-dimensional elastic-plastic material is less than the yield stress, the material deforms elastically. When the stress is equal to the yield stress, plastic deformation occurs. Stresses greater than the yield stress cannot be applied. The elastic and plastic responses are quite different and are described by different equations. During elastic deformations, no energy is dissipated; the work done in compressing the material elastically is stored in the material and, when the load is removed, the energy and the deformation are fully recovered. In the plastic behavior, however, deformations are irreversible. When the load falls below the yield stress, the plastic straining stops and the work that has been expended is not recovered.

These ideas are illustrated by subjecting a specimen of an elastic-plastic substance of unit length to a tensile stress σ . If σ is less than the yield stress σ_{cr} , the material stretches elastically and returns to its original length when the stress is removed, remaining on segment *AB* in Figure 3.1. If the yield stress σ_{cr} is applied, the material may stretch plastically to any length at any rate along segment *BCE*. Suppose it stretches an amount ε_c and then the stress is removed. It returns to a length $1 + \varepsilon_D$, having suffered a permanent plastic deformation ε_D . It then can be considered exactly as a longer sample of the original specimen. The elastic work performed along segment *AB* is recovered when the stress is removed over segment *CD*, but the plastic work dissipated along segment *BC* is irrecoverable.

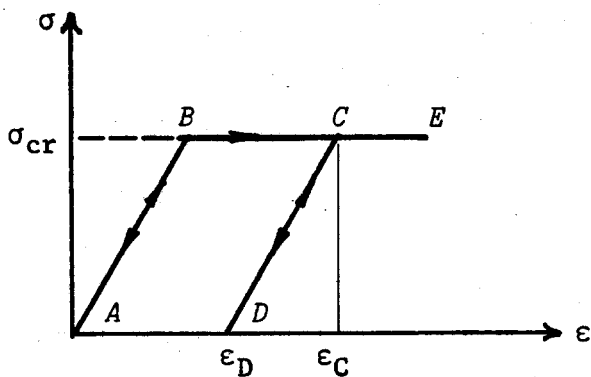


Fig. 3.1. The stress-strain relation for an ideal elastic-plastic material. See explanation in text.

In a non-ideal elastic-plastic material subjected to the same tensile test, the yield stress can change as deformation occurs. The common behavior is for plastic strain to harden the material, as on segment BCD in Figure 3.2a. It is still correct to say that the material can support no stress greater than the instantaneous value of its yield stress. (When the material has been stretched by ϵ_c , its yield stress is σ_c .) However, during deformation, and in the present model even without deformation but

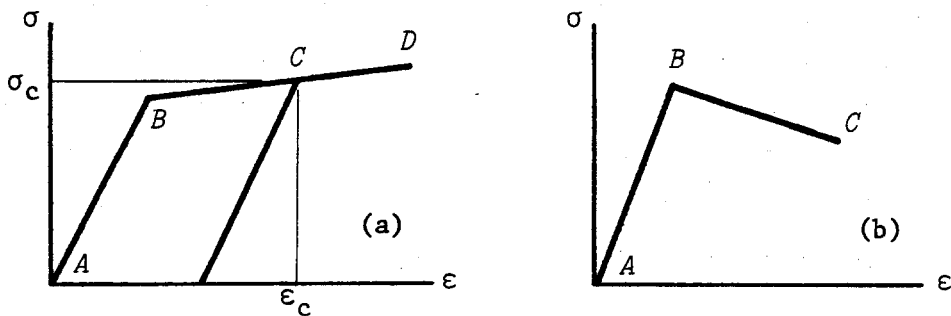


Fig. 3.2. The stress-strain relation for (a) a hardening and (b) a weakening elastic-plastic material. See explanation in text.

with freezing, the material may harden and σ_{cr} increase, so that eventually the material can support larger stresses. On the other hand, the material may weaken and σ_{cr} decrease, as on segment *BC* in Figure 3.2b, and it may not continue to support the same stresses. Our material does both.

Why do we apply an elastic-plastic law to pack ice? Our arguments have evolved from studying the most striking features of the icescape--the varied thickness of the ice, the many cracks, and the pressure ridges--so that the justification for elastic-plastic large-scale behavior is founded on our interpretation of small-scale processes. We imagine the ice pack to be densely fractured by mechanisms outside the present model--e.g., long-period waves [Assur, 1963], thermal cracking [Evans and Untersteiner, 1971], and isostatic imbalance [Schwaegler, 1974]. The fractures partition the ice into numerous strong floes. In tension the cracks between floes open without resistance, exposing regions of open water to the atmosphere. These freeze rapidly to create a matrix of thin ice surrounding the thick floes. In compression the thin ice fails and piles up and down to form pressure ridges. Both the opening and the ridging mode of deformation are permanent.

Parmerter and Coon [1973], discussing the mechanisms of ridge formation, conclude that most of the energy expended in building a ridge goes into doing work against gravity (and buoyancy) and thus appears as gravitational potential energy in the ridge. And they argue that the total work does not depend on the rate at which the ridge is built. The rate independence, together with the irreversibility of the process, suggests plastic behavior. Parmerter and Coon further predict a maximum horizontal load which can be supported by ice of a given thickness during the ridging process, making it quite natural to model ridging using plasticity theory.

A final argument for a plastic treatment is based on a strong visual similarity between the pack ice, as seen from high-altitude aircraft or satellites, and other materials, such as sands, gravels, clays, and fractured rocks, which have been modeled successfully as plastic and elastic-plastic materials.

The case for including an elastic response is made on grounds more formal than physical. The alternative, a rigid-plastic model, is undesirable because the set of equations does not close: the stress state cannot be determined when it is less than the yield stress, and if we cannot determine the stress we cannot decide whether it is critical or subcritical, plastic or rigid. On physical grounds we would argue that even under subcritical loads there should be some deformation, however small. The individual discrete floes certainly do have some elastic compressibility. If within the pack ice many of the thick floes are wedged together, and very little thin ice is present, the ice will have a large yield stress. Subcritical stresses that are applied can quite reasonably be expected to cause only elastic deformations in the thick floes. These deformations will be small compared to the plastic deformations associated with opening and closing cracks. But, although the deformations are small and probably can be neglected safely, the elastic stresses will often be quite large and must be evaluated. Only after attempting to evaluate the elastic stress can we decide whether the stress state is elastic or plastic.

3.2 The Basic Equations

To describe an elastic-plastic material mathematically, we require (1) a deformation law for elastic behavior, (2) a yield criterion, equivalent to the yield stress in the previous example, to determine whether plastic behavior can occur, and (3) a flow rule for plastic behavior. In addition to discussing these three elements in this section, we will formally equate plastic work to the production of potential energy in ridge formation and thus demonstrate how the redistribution function, defined in section 2, and the criterion for plastic flow are related.

In a two-dimensional problem such as ours, the yield criterion depends on the stress tensor σ_{ij} . It should be emphasized that what we call stress has dimensions of force per unit length and is the integral of the Cauchy stress through the thickness of the ice. For an isotropic material, the orientation of the principal axes of stress cannot affect the response, so the yield criterion can be taken to depend on the principal stresses σ_1 ,

and σ_2 . We find it convenient to define invariants σ_I and σ_{II} in terms of the stress tensor and in terms of principal values

$$\sigma_I = \text{negative pressure} = \frac{1}{2} (\sigma_1 + \sigma_2) = \frac{1}{2} \sigma_{ii} \quad (3.1)$$

and

$$\sigma_{II} = \text{maximum shear stress} = \frac{1}{2} (-\sigma_1 + \sigma_2) = \pm \sqrt{-\det \underline{\sigma}'} . \quad (3.2)$$

The stress deviator is denoted by $\underline{\sigma}'$:

$$\sigma_{ij}' = \sigma_{ij} - \frac{1}{2} \sigma_{ll} \delta_{ij} . \quad (3.3)$$

The σ_I and σ_{II} axes are obtained from the σ_1 and σ_2 axes by a 45-degree rotation and a scaling. The yield criterion is written as $F(\sigma_I, \sigma_{II}) \leq 0$, and defines a curve, called a yield curve in the (σ_I, σ_{II}) plane (Figure 3.3). Actually, $F = 0$ denotes a family of yield curves, determined by scalar parameters which are properties of the material. We will show in section 3.3 that our yield curve depends on only one parameter, the compressive yield strength p^* , which is determined by the thickness distribution.

The yield curve is analogous to the yield surface in a typical three-dimensional plasticity problem. The scalar function F is called a yield function and is written so that $F < 0$ denotes the interior of the yield curve. For an isotropic material, F must be symmetric in σ_{II} , that is (see Truesdell and Noll [1965]),

$$F(\sigma_I, \sigma_{II}, p^*) = F(\sigma_I, -\sigma_{II}, p^*) . \quad (3.4)$$

We will use the direct notation $\underline{\sigma}$ and the component notation σ_{ij} interchangeably. Occasionally, the notation $\underline{\sigma}$ will indicate the vector (σ_I, σ_{II}) ; the context will make the usage clear.

We suppose, as commonly done in plasticity theory, that the strain rate $\dot{\underline{\epsilon}}$ can be decomposed into two parts, $\dot{\underline{\epsilon}} = \dot{\underline{\epsilon}}^e + \dot{\underline{\epsilon}}^p$. The elastic strain rate $\dot{\underline{\epsilon}}^e$ is related to stress by an elastic law. The plastic strain rate $\dot{\underline{\epsilon}}^p$ is related to stress by the plastic flow law and is zero when the stress is not

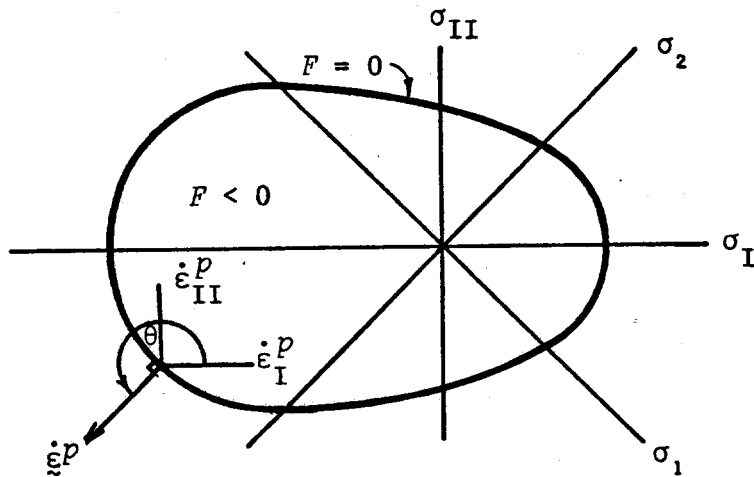


Fig. 3.3. The yield curve $F = 0$ in the (σ_I, σ_{II}) plane. The stress on the material must lie within or on this curve. The plastic flow rule (eq. 3.18) requires that the plastic strain rate be normal to the yield curve.

on the yield curve ($F < 0$). When the flow is plastic, the total strain rate $\dot{\varepsilon}$ has both elastic and plastic contributions. In the examples described in section 5, however, we have made the approximation that the elastic strain rate can be neglected during plastic flow, that is,

$$\dot{\varepsilon} = \begin{cases} \dot{\varepsilon}^e, & F < 0 \text{ (elastic),} \\ \dot{\varepsilon}^p, & F = 0 \text{ (plastic).} \end{cases} \quad (3.5)$$

The stretching, or strain rate, tensor used in this paper is defined in terms of velocity derivatives (eq. 4.4). Since the strain tensor itself has not been defined precisely here, it is not possible to state a precise relationship between the strain and strain rate tensors. The argument is weak, then, when we take time derivatives of the elastic equation 3.6, as is done in Appendix B, and interpret the time derivative of strain as being equal to the strain rate. For small deformation this interpretation is approximately valid regardless of how the strain is defined or whether one takes material (Lagrangian) or partial (Eulerian) time derivatives. More work is needed to formulate this portion of the theory so that it does not rely on the assumption of small deformations.

We assume that the elastic behavior is linear and isotropic, so that the stress-strain relation is

$$\varepsilon_{ij}^e = \frac{1}{2M_1} \frac{\sigma_{\ell\ell}}{2} \delta_{ij} + \frac{1}{2M_2} \sigma'_{ij} \quad (3.6)$$

where δ_{ij} is the Kronecker delta. The quantities M_1 and M_2 are the bulk and shear moduli, respectively, and have the same dimensions as σ_{ij} (force per unit length). We relate these moduli to the three-dimensional elastic properties of sea ice by the following argument. We assume a three-dimensional elastic response of the ice on a microscale:

$$E\varepsilon_{ij}^e = -\nu T_{kk} \delta_{ij} + (1+\nu) T_{ij} \quad i,j,k = 1,2,3 \quad (3.7)$$

where ε_{ij}^e is a three-dimensional strain tensor, and E and ν are Young's modulus and Poisson's ratio of sea ice (assumed constant). We define T_{ij} to be the Cauchy stress less the average hydrostatic stress

$-(\frac{1}{2} \rho_{\text{water}} \hat{g} \zeta'^2 / \zeta) \delta_{ij}$, in which ρ_{water} is the density of sea water, \hat{g} is the acceleration of gravity, and ζ' is the thickness of the submerged portion of ice of thickness ζ . Thus, in eq. 3.7, strains caused by the hydrostatic load are neglected. We integrate the microscale response over a typical region, R , by a procedure similar to that used to define the thickness distribution G . In this case, however, we also integrate through the thickness, $\zeta(x,t)$, to get

$$E \iint_{R \times 0}^{\zeta} \varepsilon_{ij}^e dz da = \iint_{R \times 0}^{\zeta} [-\nu T_{kk} \delta_{ij} + (1+\nu) T_{ij}] dz da. \quad (3.8)$$

We now wish to introduce average quantities that are more meaningful on the desired macroscale. The stress resultant $\underline{\sigma}$ may be related to the stress \underline{T} by

$$\underline{\sigma} = \frac{1}{R} \int_R (\int_0^{\zeta} \underline{T} dz) da \quad (3.9)$$

where R is the area of the two-dimensional region R .

The integral on the left-hand side of eq. 3.8 can be simplified by making assumptions about $\underline{\varepsilon}^e$. First we assume that the elastic strain $\underline{\varepsilon}^e$ does not depend on the vertical coordinate, z , and we write

$$E \int_R \int_0^\zeta \xi^e dz da = E \int_R \zeta \xi^e da. \quad (3.10)$$

Then we assume that $\xi^e(x)$ can be written as a function only of ice thickness ζ ; $\xi^e(x) = \hat{\xi}(\zeta(x))$. Then the area integral can be written as an h integral:

$$E \int_R \zeta \xi^e da = R E \int_0^\infty h \hat{\xi}(h) g(h) dh. \quad (3.11)$$

Even though we expect $\hat{\xi}$ to depend on h in actuality, we neglect this dependence here. With this assumption, all of the integrals in eq. 3.8, 3.10, and 3.11 collapse immediately to $R E \bar{h} \xi^e$, where \bar{h} is the average ice thickness in R . Finally, then, we have

$$E \bar{h} \xi_{ij}^e = -v \sigma_{kk} \delta_{ij} + (1+v) \sigma_{ij}. \quad (3.12)$$

For our two-dimensional pack-ice theory, only the values $i,j = 1,2$ apply. As the equation has been formulated, it is valid for our use as long as we assume that $\sigma_{33} = 0$. The comparison of eq. 3.12 with eq. 3.6 shows that

$$\begin{aligned} M_1 &= \frac{E}{2(1-v)} \bar{h}, \\ M_2 &= \frac{E}{2(1+v)} \bar{h}. \end{aligned} \quad (3.13)$$

Zubov [1943] has given values, for fresh ice, of

$$E = 6 \times 10^6 \text{ to } 180 \times 10^6 \text{ dyn/cm}^2, \text{ and} \quad (3.14)$$

$$v = 0.36$$

with other values obtained from acoustic sound speeds going as much as three orders of magnitude higher. We have used values of Young's modulus near the lower limits and a reasonable Poisson's ratio ($E = 2/3 \times 10^7$, $v = 1/3$) to obtain the two-dimensional properties

$$\begin{aligned} M_1 &= 10^7 \bar{h} \text{ dyn/cm} \\ M_2 &= 1/2 \times 10^7 \bar{h} \text{ dyn/cm} \end{aligned} \quad \left\{ \begin{array}{l} (\bar{h} \text{ in cm}) \end{array} \right\} \quad (3.15)$$

Whenever the stress state lies on the yield curve, plastic (permanent) deformation can occur, and irrecoverable work is performed. In the one-dimensional tensile test described above, the flow rule for the ideal plastic was simply that an indefinite extension could occur. In more than one dimension, the situation is more complicated. We assume, for reasons examined in section 3.6, the plastic flow law

$$\dot{\varepsilon}_{ij}^p = \lambda \frac{\partial F}{\partial \sigma_{ij}} \Big|_{F=0} \quad \text{for } i,j = 1,2 \text{ and } \lambda \geq 0 \quad (3.16)$$

where $\dot{\varepsilon}_{ij}^p$ is the plastic strain rate, and λ is some undetermined scalar to be found as part of the solution. This equation states that the plastic strain rate is normal to the yield curve, but is of unknown magnitude. We can rewrite eq. 3.16 after differentiating by the chain rule and evaluating $\partial\sigma_I/\partial\sigma_{ij}$ and $\partial\sigma_{II}/\partial\sigma_{ij}$ as

$$\dot{\varepsilon}_{ij}^p = \lambda \left(\frac{1}{2} \frac{\partial F}{\partial \sigma_I} \delta_{ij} + \frac{1}{2\sigma_{II}} \frac{\partial F}{\partial \sigma_{II}} \sigma'_{ij} \right) \Big|_{F=0} \quad (3.17)$$

which shows that the principal axes of stress and strain rate are aligned. When we write eq. 3.17 as

$$\dot{\varepsilon}_k^p = \lambda \frac{\partial F}{\partial \sigma_k} \Big|_{F=0} \quad k = I, II \quad (3.18)$$

the idea of normality becomes very graphic, as in Figure 3.3. There, we see that if $\dot{\varepsilon}_I^p$ (the divergence of velocity) and $\dot{\varepsilon}_{II}^p$ (defined in section 2.3.2, and equal to $\pm 2(-\det \xi^p')^{1/2}$, where ξ^p' denotes the strain rate deviator) are plotted parallel to the (σ_I, σ_{II}) -axes, the vector $(\dot{\varepsilon}_I^p, \dot{\varepsilon}_{II}^p)$ is normal to the yield curve. We have not considered the implications of other possible flow rules.

3.3 An Energy Relation Between the Yield Function and the Redistribution Function

Although the elastic-plastic constitutive equations (3.5), (3.6), and (3.16) show us how to use the yield function F , we have not yet provided any insight into the form of this function. We will now introduce an energy argument which determines F uniquely in terms of the redistribution function Ψ [Rothrock, 1974a,b]. This relation between F and Ψ is an important and unifying element of our model.

We assume that the rate of dissipation of plastic work $\sigma_{ij}\dot{\varepsilon}_{ij}^p$ equals the rate of production of isostatic potential energy in pressure ridge formation, given by the term $c\int h^2 d\Psi$ in eq. 2.27. Although the non-isostatic potential energy may be a substantial fraction (0.4) of the total potential energy, certainly part--and perhaps a large part--of the formation of non-isostatic potential energy is due to processes other than ridging, such as unequal ablation of sails and keels of ridges, drifting snow, and melt pond formation. Thus, equating plastic work to changes in isostatic potential energy may be a better approximation than supposing total potential energy to be given by its isostatic part. Other possible energy sinks in ridge formation have been neglected, because they have been shown to be small compared to the storage of potential energy [Parmerter and Coon, 1973]; these are the surface energy produced as sheets of ice are fragmented, the frictional losses as rubble tumbles, and the elastic energy stored in the bending ice sheet. We have also ignored frictional losses associated with shearing between ice floes, of which no estimate has been made.

Because of the alignment of principal axes of stress and strain rate, the plastic work $\sigma_{ij}\dot{\varepsilon}_{ij}^p$ can be written in the notation of section 2.3.2 as

$$\sigma_I \dot{\varepsilon}_I^p + \sigma_{II} \dot{\varepsilon}_{II}^p . \quad (3.19)$$

To eliminate Ψ from the integral $\int h^2 d\Psi$, we assume that the strain rate $\dot{\varepsilon}$ in 2.21 refers specifically to the plastic strain rate $\dot{\varepsilon}^p$. (In fact, we have ignored all effects on the thickness distribution caused by elastic deformations, and $\text{div } \underline{v}$ in eq. 2.6 has been approximated by $\dot{\varepsilon}_I^p$.) The integral $c\int h^2 d\Psi$ can be written, then, as

$$\left[(\dot{\varepsilon}_I^p)^2 + (\dot{\varepsilon}_{II}^p)^2 \right]^{\frac{1}{2}} p^* \alpha_r(\theta) \quad (3.20)$$

by defining

$$p^* = c \int h^2 dW_r \quad (3.21)$$

By equating the plastic work (3.19) to the mechanical formation of potential energy (3.20), we have

$$(\sigma_I \cos\theta + \sigma_{II} \sin\theta) \Big|_{F=0} = p^* \alpha_r(\theta) \quad (3.22)$$

which is algebraic in the ridging coefficient α_r and differential in the yield function F since θ is known in terms of $\partial F / \partial \sigma_I$ and $\partial F / \partial \sigma_{II}$.

We can immediately establish the points where the yield curve intersects the σ_I -axis. The curve is symmetric about the σ_I -axis since it is an even function of σ_{II} . At $\sigma_{II} = 0$, θ must take the value zero or π . Equation 3.22 and the conditions $\alpha_r(0) = 0$ and $\alpha_r(\pi) = 1$ show that $\sigma_I(\theta=0)$ takes the value zero, and $\sigma_I(\theta=\pi)$ takes the value $-p^*$.

The yield function satisfying eq. 3.22 is of the form $F(\sigma_I/p^*, \sigma_{II}/p^*)$; hence, the shape of the yield curve is determined by $\alpha_r(\theta)$ and is independent of p^* . This relation is best seen by defining nondimensional stresses $x = \sigma_I/p^*$ and $y = \sigma_{II}/p^*$ and regarding the yield criterion $F(x,y) = 0$ as the curve $y = y(x)$. The angle θ (between the x -axis and the curve's normal) is given by $\tan\theta = -(dy/dx)^{-1}$. Equation 3.22 can then be rewritten as

$$y = -(\tan\theta)^{-1} x + \frac{\alpha_r(\theta)}{\sin\theta} . \quad (3.23)$$

This is Clairaut's equation; it has a straight line solution for each value of θ with slope $(-\tan\theta)^{-1}$ and y -intercept $\alpha_r/\sin\theta$. This equation also has a singular solution consisting of the envelope of these straight lines, and it is this solution which we require for a yield curve (see Fig. 3.4). Thus, there is a direct correlation between $\alpha_r(\theta)$ and the singular solution ($y = y(x)$ or $F = 0$). If $\alpha_r(\theta)$, and therefore a family of straight lines,

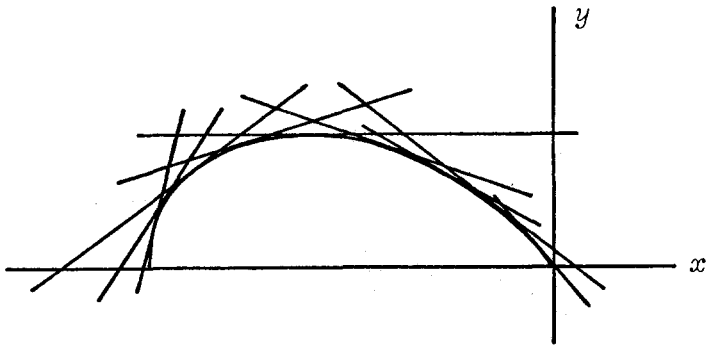


Fig. 3.4. The set of tangents specified by eq. 3.23. Their envelope is the yield curve.

is given, there exists a unique envelope. On the other hand, if the yield curve is given, it has only one set of tangent lines which determine $\alpha_r(\theta)$.

The restrictions that the yield function depends on only one parameter p^* and that this parameter does not affect the shape of the yield curve are not general restrictions; they are consequences of the assumed form of the redistribution function and of the assumed potential energy relation. Other parameters would be introduced by including energy sinks other than potential energy and by assuming the existence of additional ridging modes.

One can visualize the yield criterion $F(\sigma_I, \sigma_{II}, p^*) = 0$ as a surface in $(\sigma_I, \sigma_{II}, p^*)$ space (Fig. 3.5). This surface is a material property and never changes (in analogy with the redistribution proces Γ defined in section 2.3.1). The material is described at a given instant by a point within or on the surface. The intersection of the plane $p^* = \text{constant}$ with the surface determines the yield curve.

Equation 3.22 relates the size of the yield curve p^* to the ridging mode W_r and the shape of the yield curve to the ridging coefficient $\alpha_r(\theta)$. In our current thinking, we tend to assume that W_r is known and determines p^* , but that α_r is unknown until determined by the yield curve, whose shape we are content to assume.

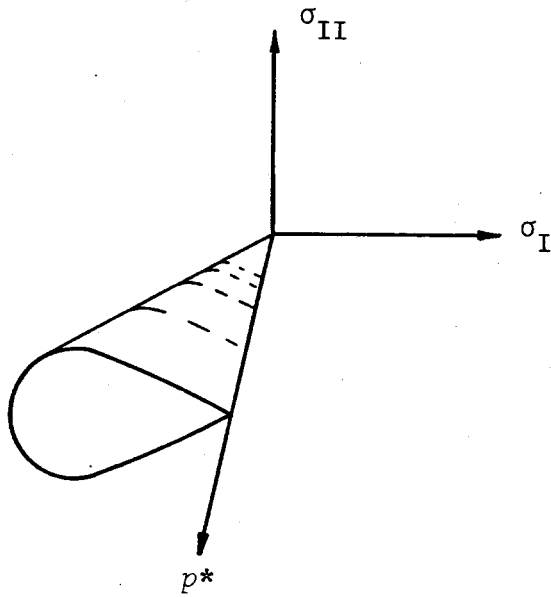


Fig. 3.5. The yield surface $F(\sigma_I, \sigma_{II}, p^*) = 0$.

3.4 Possible Shapes of the Yield Curve

Neither the shape of the yield curve nor $\alpha_r(\theta)$ can be said to be known. Our procedure is to deduce what we can about the yield curve from our physical picture of pack ice and then to calculate α_r . We have asserted that the yield curve is symmetrical about the σ_I -axis and passes through the points $(0,0)$ and $(-p^*,0)$. Randomly oriented cracks should preclude tension in any direction, so the yield curve should be confined to the quadrant in Figure 3.3 in which the principal stresses σ_1 and σ_2 are negative. Within these general constraints, any yield curve is physically acceptable. A general property of yield curves of this type is that shear stress can only be applied if pressure is applied simultaneously--a property well documented in some granular materials.

For the examples of section 5, we have chosen a circular yield curve (in Fig. 3.6) even though it violates the no-tension constraint described above. We chose it because its equation does not require piecewise definitions and so minimizes the logical decisions to be made during numerical calculations.

The square yield curve in Figure 3.6 represents behavior in which the principal directions behave independently. Whenever the critical value of

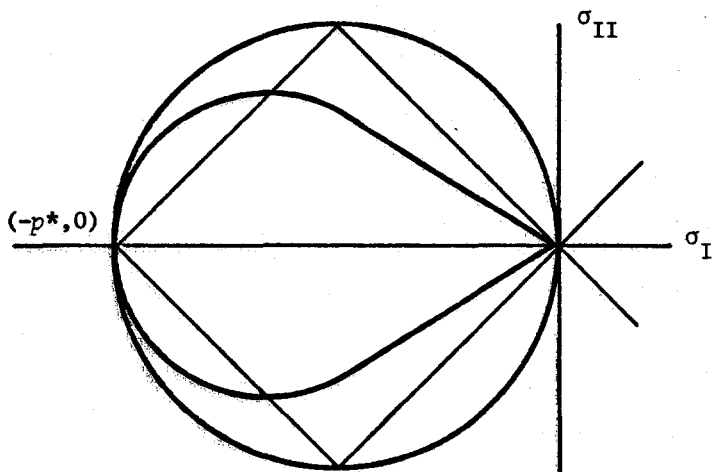


Fig. 3.6. Yield curves of several shapes.

stress is reached in either principal direction, flow occurs in that direction. On any of the sides of that yield curve, the strain is uniaxial. However, at any of the four corners, flow in both principal directions can occur.

The ice-cream-cone yield curve is a two-dimensional version of the yield curve used by Drucker and Prager [1952] and Nelson, Baron, and Sandler [1971] to analyze soils and rock. This behavior is well documented for soil (e.g.; Schofield and Wroth [1968]). It was introduced for pack ice by Coon [1972]. The two straight-line portions represent a two-dimensional analogue of the Coulomb yield criterion [Shield, 1955], which states that the amount of shear stress sustained by a material is linearly related to the pressure.

Although the Coulomb criterion is usually stated for three dimensions, we make the statement for our two-dimensional problem that the shear stress σ_{II} in the horizontal plane is proportional to the horizontal pressure σ_I . We are assuming then that any vertical stress, σ_z , say, does not affect the shear stress σ_{II} that the pack can sustain. The two-dimensional Coulomb yield curve is therefore different from the curve obtained by intersecting a plane, $\sigma_z = \text{constant}$, say, with a three-dimensional Coulomb surface appropriate to a material that is isotropic in three dimensions. In this respect the present treatment departs from the approach frequently used in soil and rock mechanics.

In pack ice, the flow associated with a stress state on one of the straight sides requires opening, but no ridging, so α_r is zero. Such a condition would seem quite reasonable for pack ice when it resembles a granular material, as in Figure 1.3. The circular cap on the loading surface is associated with ridging; here α_r is no longer zero.

Several general relations can be stated between the shape of the yield curve and the properties of $\alpha_r(\theta)$. It helps to associate with each point on the yield curve a value of θ (many values at corners) and thus a value of α_r . Three of these relations are (1) that α_r is zero at the origin of the (σ_I, σ_{II}) plane and on straight-line segments of the yield curve through the origin, (2) that $\alpha_r(\theta)$ is a continuous, single-valued function for any closed, convex yield curve, and (3) that discontinuities in $d\alpha_r/d\theta$ correspond to straight-line segments of the yield curve [Rothrock, 1974b]. A necessary condition on $\alpha_r(\theta)$ for the yield curve to be convex is given by eq. 3.30.

3.5 The Yield Strength p^* --Hardening and Weakening of the Material

The yield strength p^* depends on the thickness distribution through eq. 3.21. We can acquire some feeling for this dependence by assuming the linear, one-to-one redistribution process and putting $\hat{h}(h) = \frac{1}{k} h$ in example 3 of section 2.3.1. Then

$$p^* = 2kc \int_0^\infty h[1 - A(h)]dh \quad (3.24)$$

where $k = 5$ is the multiplier in the special form of the ridging rule given later in eq. 4.20, and c is as used in eq. 2.25. An approximate expression for p^* in terms of h^* ($\equiv G^{-1}(G^*)$) may be reached by assuming that the thin ice is uniformly distributed; i.e.,

$$G(h) \approx \frac{G^*h}{h^*}, \quad 0 < h < h^*. \quad (3.25)$$

Using eq. 4.19 for $B(G)$ and evaluating the integral for p^* in eq. 3.24 we get

$$p^* \approx \frac{kc}{6} h^{*2} \approx 37h^{*2} \text{ dyn cm}^{-1} \text{ (with } h^* \text{ in cm).} \quad (3.26)$$

An upper bound on p^* is easily found by considering the case in which all of the ice going into the ridging process has thickness h^* . Then, $A(h) = H(h - h^*)$ and

$$p^* = kc h^{*2} \approx 220h^{*2} \text{ dyn cm}^{-1} \text{ (with } h^* \text{ in cm).} \quad (3.27)$$

In the present model, the thickness distribution is continually changing, causing p^* (and the elastic moduli which depend on the mean thickness) to vary. Such dependence of the yield function on a single scalar parameter has been proposed previously for other geological materials. Sands [Nelson, Baron, and Sandler, 1971; Schofield and Wroth, 1968], clays [Schofield and Wroth, 1968], and porous solids [Green, 1972] have all been described by relating the yield function to some measure of the volume change; the yield function of rocks has been related to a plastic strain invariant involving both volume change and shear [Nelson, Baron, and Sandler, 1971].

An equation for \dot{p}^* is obtained by differentiating eq. 3.21 (or, for our redistribution function, eq. 3.24) giving

$$\dot{p}^* = 2kc \int_0^\infty \frac{\partial B}{\partial G} [hf \frac{\partial G}{\partial h} - h(\Psi - G \operatorname{div} \boldsymbol{\nu})] dh. \quad (3.28)$$

Since $\partial B/\partial G$ is zero outside (h_0, h^*) , we could restrict the integral to that interval. In the cases considered here, but not in all possible cases, f is positive over (h_0, h^*) so that the thermodynamics always tends to strengthen the ice. In any case, since h and $\partial G/\partial h$ are non-negative, the sign of this term depends only on the sign of f in (h_0, h^*) . The other term $-h(\Psi - G \operatorname{div} \boldsymbol{\nu})$ may change sign within (h_0, h^*) and may therefore have either a positive or a negative net effect depending on the present distribution and on the strain rate state. In pure divergence, the term is negative for all h , thus tending to decrease p^* ; similarly, pure convergence always tends to increase p^* .

3.6 Drucker's Postulate and the Present Theory

Our initial thinking about a plastic model for pack ice was based on ideas strongly linked to a postulate by Drucker [1950] which helped to unify the early development of plasticity theory. The postulate states that if a material is under stress and an external agent applies an additional stress so that plastic deformation occurs, the work provided by the agent must be positive.

When our material is weakening ($\dot{\varepsilon}^p < 0$), it violates this postulate, as shown schematically in Figure 3.7. At some initial instant, when the yield curve is the outer circle and the ice is supporting a stress $\underline{\sigma}$, the material begins to deform. After some time interval, sufficient open water has been created to weaken the material and reduce the yield curve to the smaller circle. The external agent must apply a stress $\Delta\underline{\sigma}$ so that the new stress state is $\underline{\sigma} + \Delta\underline{\sigma}$. The work performed by the external agent is $\int \dot{\varepsilon}^p \cdot \Delta\underline{\sigma} dt$, which is negative whenever the new yield curve lies inside the initial yield curve. (The quantities $\dot{\varepsilon}^p$ and $\Delta\underline{\sigma}$ denote the vectors $(\dot{\varepsilon}_I^p, \dot{\varepsilon}_{II}^p)$ and $(\Delta\sigma_I, \Delta\sigma_{II})$.)

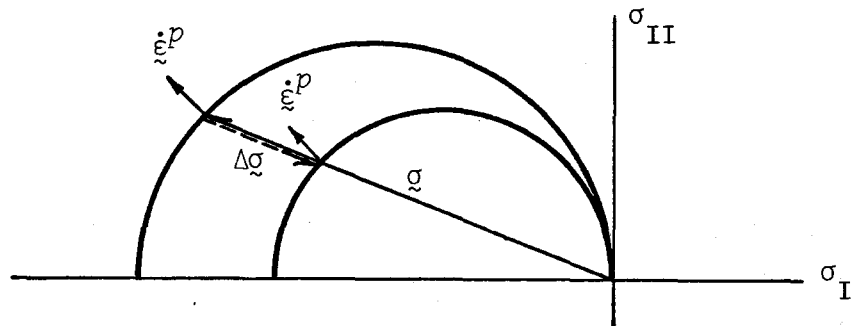


Fig. 3.7. The contraction of the yield curve during weakening.
The external agent works on the material at a rate $\Delta\underline{\sigma} \cdot \dot{\varepsilon}^p$,
which is negative.

We cannot, therefore, base our theory on Drucker's postulate. However, there are three consequences of the postulate which are desirable for simplicity and which we maintain in our theory:

1. The flow rule is given by equation 3.16. This has been assumed in the present theory.

2. The rate of plastic work $\dot{g} \cdot \dot{\xi}^p$ is non-negative. (The plastic work above is not the same as the work applied by the external agent $\Delta g \cdot \dot{\xi}^p$.) This is true by virtue of the energy relation assumed in section 3.3 and the assumption that ridges congeal and therefore cannot unridge. The plastic work has the same sign as $\alpha_r(\theta)$, which is taken to be non-negative.

3. The yield curve is everywhere convex (outward). We assume this to be a property of the yield curve and ask what restriction this condition places on $\alpha_r(\theta)$. We know, without convexity and simply by the definition of the redistribution function, that α_r is a continuous, single-valued function of θ ; that $\alpha_r(0)$ is zero and $\alpha_r(\pi)$ is 1; that both $\alpha_r(\theta)$ and $\alpha_o(\theta)$ are non-negative; and, therefore, by equation 2.22, that α_r satisfies

$$\alpha_r \geq \begin{cases} 0 & , \quad 0 \leq \theta \leq \pi/2 , \\ -\cos \theta & , \quad \pi/2 \leq \theta \leq \pi . \end{cases} \quad (3.29)$$

Convexity implies that d^2y/dx^2 is non-positive, in the notation of equation 3.23. This condition can be shown to be equivalent to the inequality

$$\frac{d^2\alpha_r}{d\theta^2} + \alpha_r \geq 0 . \quad (3.30)$$

4. A COMPLETE MODEL FOR MASS AND MOMENTUM

We have, in the two preceding sections, developed the theory for two new elements in a model of the large-scale movement and mass balance of pack ice: the balance equation for the thickness distribution (2.6) and the elastic-plastic constitutive equations (3.5, 3.6, and 3.16). In addition, we have argued that a strong constraint (expressed by equations 3.21 and 3.22) can be found between the redistribution function and the yield function by invoking a simple argument about the energetics of the controlling mechanism, pressure ridge formation.

In this section we record explicitly the set of field equations and constitutive equations which together make up a complete model of the mass and momentum balances of pack ice.

4.1 The Governing Equations

The primary field variables in two spatial dimensions are the velocity v_i , the thickness distribution $G(h)$, and the stress tensor σ_{ij} . The stress tensor is required to be symmetric to conserve angular momentum. All variables are regarded as functions of space x_i and time t ; only the thickness distribution is a function of the additional independent variable h . We use interchangeably the direct notations x and g with the component notations x_i and σ_{ij} , where $i,j = 1,2$.

The mass m and the yield strength p^* are determined from the thickness distribution by

$$m = \rho_{\text{ice}} \int_0^1 h \, dG \quad (4.1)$$

and

$$p^* = c \int_0^1 h^2 \, dW_r \quad (4.2)$$

where ρ_{ice} is the density of sea ice and c , as defined in section 2.4, is

$$c = \frac{1}{2} \hat{g} \rho_{\text{ice}} (\rho_{\text{water}} - \rho_{\text{ice}}) / \rho_{\text{water}} \quad (4.3)$$

The strain rate

$$\dot{\varepsilon}_{ij} = \frac{1}{2} \left(\frac{\partial v_i}{\partial x_j} + \frac{\partial v_j}{\partial x_i} \right) \quad (4.4)$$

is approximated by

$$\dot{\varepsilon}_{ij} = \begin{cases} \dot{\varepsilon}_{ij}^e, & F(\xi, p^*) < 0 \\ \dot{\varepsilon}_{ij}^p, & F(\xi, p^*) = 0 \end{cases} \quad (4.5)$$

as described in section 3.1. When ξ occurs as an argument of F , it denotes (σ_I, σ_{II}) .

The governing equations are:

(1) The thickness distribution equation

$$\frac{d}{dt} G = -f \frac{\partial G}{\partial h} + (\Psi - G \operatorname{div} \underline{v}) \quad (4.6)$$

where d/dt is the material derivative; f is the thermodynamic growth rate of ice, known as a function of the independent variables h , \underline{x} , and t ; and $\Psi(h, \dot{\xi}, G)$ is a known function of h and dependent variables. We make the approximation in eq. 4.6 that elastic deformations do not affect the thickness distribution of a Lagrangian area; hence, we assume

$$\Psi = \Psi(h, \dot{\xi}^p, G) \quad (4.7)$$

and approximate $G \operatorname{div} \underline{v}$ by $G \dot{\varepsilon}_{ii}^p$, neglecting the quantity $G \dot{\varepsilon}_{ii}^e$.

(2) The momentum equation

$$m \frac{d}{dt} \underline{v} = -m f_c \underline{k} \times \underline{v} + \underline{\tau}_w + \operatorname{div} \underline{g} + \underline{\tau}_a - m \hat{g} \operatorname{grad} H \quad (4.8)$$

in which \underline{k} is the unit vector in the vertical; the Coriolis parameter f_c , the air stress $\underline{\tau}_a$, and the sea surface height H are given as functions of \underline{x} and t ; the water stress $\underline{\tau}_w$ is known in terms of \underline{v} , \underline{x} , and t ; and \hat{g} is the acceleration of gravity.

(3) The elastic constitutive law

$$\dot{\varepsilon}_{ij}^e = \frac{1}{4M_1} \sigma_{\ell\ell} \delta_{ij} + \frac{1}{2M_2} \sigma'_{ij} \quad (4.9)$$

in which M_1 and M_2 are known in terms of G , as in eq. 3.15, and δ_{ij} is the Kronecker delta.

(4) The plastic constitutive law

$$\dot{\varepsilon}_{ij}^p = \begin{cases} 0 & \text{when } F(\underline{\sigma}, p^*) < 0, \text{ and} \\ \lambda \frac{\partial F}{\partial \sigma_{ij}} & \text{when } F(\underline{\sigma}, p^*) = 0, \end{cases} \quad (4.10)$$

in which F is a known function and λ is an unknown scalar. Table 4.1 summarizes the dependent variables and the equations.

(5) The yield criterion

$$F(\underline{\sigma}, p^*) = 0. \quad (4.12)$$

TABLE 4.1

THE UNKNOWN AND THE EQUATIONS THAT DETERMINE THEM

Scalar Unknown	Equation	Vector Unknown	Equation	Tensor Unknown	Equation
m	4.1	\underline{v}	4.8	$\dot{\underline{\varepsilon}}$	4.4
p^*	4.2			$\dot{\underline{\varepsilon}}^p$	4.5
G	4.6			$\dot{\underline{\varepsilon}}^e$	4.9
Ψ	4.7			$\underline{\sigma}$	either 4.10 or 4.11
λ	4.12				

Our assumptions about $f(h, \underline{x}, t)$, $\Psi(h, \dot{\underline{\varepsilon}}^p, G)$, and $F(\underline{\sigma}, p^*)$ are described in the following subsections.

4.2 Thermodynamic Ice Growth

The rate of ice growth f in eq. 4.6 is a function of ice thickness, position, and time (season). It is determined by the magnitude of the atmospheric and oceanic energy fluxes at the horizontal boundaries of the ice, by the thermal history of the ice, by the thickness of the snow cover, and by the distribution of liquid brine inclusions within the interior of the ice.

Although existing field observations are insufficient to determine f directly, various ice growth models can be used to estimate f from the heat balance or temperature data that are available.

Growth rates for different ranges of thickness were calculated by different methods, as we describe in detail below. Briefly, growth rates for thin ice (up to 50 cm) were determined from an empirical formula [Anderson, 1961]. Rates for the thickness range 100 cm to 400 cm were deduced from a theoretical model [Maykut and Untersteiner, 1969, 1971]. Rates for ice thicker than 800 cm were related to the oceanic heat flux. In the two intermediate ranges (50 cm to 100 cm, and 400 cm to 800 cm), rates are interpolated.

In the calculations in section 5, we use growth rates applicable to the central Arctic Basin; spatial variations are not treated. Values for f throughout the year are summarized in Table 4.2 at 50 cm intervals up to 1000 cm and illustrated in Figure 4.1. We believe that these values are representative up to a thickness of about 500 cm, but somewhat arbitrary for thicker ice.

4.2.1 Moderately Thick Ice

Our basic tool for obtaining growth rates is the ice growth model of Maykut and Untersteiner [1969, 1971] which utilizes energy balance equations to predict mass changes at the top and bottom of the ice. This model incorporates the effects of (1) internal heating caused by short-wave radiation penetrating the interior of the ice, (2) latent heat release by the included brine, and (3) insulation by the seasonal snow cover. Required inputs from

TABLE 4.2

GROWTH RATES OF SEA ICE IN CM DAY⁻¹ AS A FUNCTION OF THICKNESS AND TIME OF YEAR

Date	Thickness (in centimeters)									
	0	50	100	150	200	250	300	350	400	450
Jan 1	12.09	1.95	0.46	0.37	0.31	0.27	0.21	0.14	0.09	0.03
11	12.15	1.97	0.51	0.37	0.32	0.27	0.21	0.17	0.11	0.06
21	12.29	2.00	0.57	0.37	0.32	0.27	0.22	0.18	0.13	0.07
Feb 1	12.49	2.07	0.63	0.37	0.32	0.27	0.23	0.19	0.15	0.09
11	12.67	2.11	0.68	0.37	0.32	0.28	0.25	0.20	0.16	0.10
21	12.82	2.16	0.73	0.39	0.34	0.29	0.25	0.20	0.17	0.11
Mar 1	12.90	2.18	0.77	0.40	0.34	0.29	0.25	0.21	0.17	0.12
11	12.71	2.13	0.80	0.39	0.34	0.29	0.26	0.23	0.18	0.13
21	12.38	2.03	0.81	0.38	0.34	0.29	0.26	0.23	0.19	0.13
Apr 1	11.71	1.86	0.41	0.36	0.32	0.29	0.25	0.23	0.20	0.14
11	10.82	1.63	0.36	0.32	0.29	0.27	0.25	0.23	0.20	0.14
21	9.69	1.36	0.34	0.28	0.26	0.25	0.23	0.22	0.19	0.14
May 1	8.18	1.03	0.27	0.22	0.22	0.22	0.21	0.21	0.18	0.14
11	6.88	0.78	0.21	0.17	0.18	0.18	0.19	0.18	0.17	0.13
21	5.16	0.50	0.13	0.12	0.14	0.15	0.15	0.16	0.16	0.12
Jun 1	3.10	0.24	0.05	0.07	0.09	0.11	0.12	0.14	0.14	0.12
11	0.00	0.00	-0.00	0.03	0.05	0.08	0.09	0.11	0.12	0.10
21	-0.65	-0.20	-0.08	-0.01	0.02	0.05	0.07	0.08	0.10	0.08
Jul 1	-1.60	-1.40	-1.32	-1.28	-1.25	-1.21	-1.16	-0.40	0.07	0.07
11	-1.55	-1.35	-1.25	-1.22	-1.19	-1.17	-1.14	-1.12	-1.11	-1.10
21	-1.40	-1.20	-1.07	-1.04	-1.01	-0.99	-0.97	-0.94	-0.93	-0.93
Aug 1	-1.00	-0.90	-0.84	-0.80	-0.77	-0.75	-0.72	-0.71	-0.69	-0.70
11	-0.65	-0.55	-0.52	-0.49	-0.46	-0.43	-0.42	-0.40	-0.39	-0.38
21	0.13	0.01	-0.17	-0.14	-0.10	-0.06	-0.04	-0.02	-0.00	-0.00
Sep 1	4.08	0.36	-0.16	-0.14	-0.10	-0.07	-0.05	-0.03	-0.01	-0.01
11	5.50	0.56	-0.12	-0.13	-0.10	-0.07	-0.06	-0.04	-0.02	-0.02
21	6.81	0.77	0.06	-0.12	-0.10	-0.08	-0.06	-0.05	-0.03	-0.03
Oct 1	8.05	1.01	0.25	-0.03	-0.09	-0.08	-0.07	-0.05	-0.03	-0.03
11	9.01	1.21	0.34	0.10	-0.05	-0.07	-0.06	-0.05	-0.04	-0.04
21	9.99	1.43	0.40	0.20	0.04	-0.04	-0.06	-0.05	-0.05	-0.04
Nov 1	10.97	1.66	0.48	0.26	0.12	0.02	-0.03	-0.04	-0.04	-0.04
11	11.55	1.81	0.55	0.30	0.19	0.08	0.00	-0.02	-0.03	-0.03
21	11.95	1.92	0.62	0.34	0.25	0.14	0.05	0.00	-0.02	-0.02
Dec 1	12.06	1.95	0.44	0.35	0.28	0.20	0.11	0.04	0.00	-0.01
11	12.04	1.94	0.44	0.37	0.30	0.23	0.15	0.08	0.03	-0.00
21	12.04	1.94	0.44	0.38	0.31	0.25	0.19	0.12	0.06	0.01

TABLE 4.2 -- Continued

Date	Thickness (in centimeters)										
	500	550	600	650	700	750	800	850	900	950	1000
Jan 1	0.00	-0.02	-0.03	-0.04	-0.05	-0.05	-0.06	-0.06	-0.06	-0.06	-0.06
11	0.02	-0.01	-0.03	-0.04	-0.04	-0.05	-0.06	-0.06	-0.06	-0.06	-0.06
21	0.03	0.00	-0.02	-0.04	-0.04	-0.05	-0.06	-0.06	-0.06	-0.06	-0.06
Feb 1	0.05	0.01	-0.02	-0.03	-0.04	-0.05	-0.06	-0.06	-0.06	-0.06	-0.06
11	0.05	0.01	-0.01	-0.03	-0.04	-0.05	-0.06	-0.06	-0.06	-0.06	-0.06
21	0.06	0.02	-0.01	-0.02	-0.04	-0.05	-0.06	-0.06	-0.06	-0.06	-0.06
Mar 1	0.07	0.03	-0.00	-0.02	-0.04	-0.05	-0.06	-0.06	-0.06	-0.06	-0.06
11	0.08	0.04	0.00	-0.02	-0.04	-0.05	-0.06	-0.06	-0.06	-0.06	-0.06
21	0.08	0.04	0.01	-0.02	-0.03	-0.05	-0.06	-0.06	-0.06	-0.06	-0.06
Apr 1	0.09	0.05	0.01	-0.01	-0.03	-0.05	-0.06	-0.06	-0.06	-0.06	-0.06
11	0.09	0.05	0.02	-0.01	-0.03	-0.05	-0.06	-0.06	-0.06	-0.06	-0.06
21	0.10	0.06	0.02	-0.01	-0.03	-0.05	-0.06	-0.06	-0.06	-0.06	-0.06
May 1	0.10	0.06	0.03	-0.00	-0.03	-0.04	-0.06	-0.06	-0.06	-0.06	-0.06
11	0.09	0.06	0.03	-0.00	-0.03	-0.04	-0.06	-0.06	-0.06	-0.06	-0.06
21	0.09	0.06	0.03	-0.00	-0.02	-0.04	-0.06	-0.06	-0.06	-0.06	-0.06
Jun 1	0.08	0.05	0.02	-0.00	-0.02	-0.04	-0.06	-0.06	-0.06	-0.06	-0.06
11	0.07	0.05	0.02	-0.00	-0.02	-0.04	-0.06	-0.06	-0.06	-0.06	-0.06
21	0.06	0.04	0.02	-0.00	-0.03	-0.04	-0.06	-0.06	-0.06	-0.06	-0.06
Jul 1	0.05	0.03	0.02	-0.00	-0.03	-0.04	-0.06	-0.06	-0.06	-0.06	-0.06
11	-1.11	-1.13	-1.15	-1.17	-1.18	-1.20	-1.20	-1.20	-1.20	-1.20	-1.20
21	-0.93	-0.94	-0.96	-0.97	-0.99	-1.00	-1.00	-1.00	-1.00	-1.00	-1.00
Aug 1	-0.70	-0.71	-0.71	-0.73	-0.74	-0.75	-0.75	-0.75	-0.75	-0.75	-0.75
11	-0.38	-0.39	-0.39	-0.41	-0.42	-0.43	-0.43	-0.43	-0.43	-0.43	-0.43
21	0.00	-0.01	-0.02	-0.02	-0.04	-0.05	-0.06	-0.06	-0.06	-0.06	-0.06
Sep 1	-0.01	-0.01	-0.02	-0.02	-0.04	-0.05	-0.06	-0.06	-0.06	-0.06	-0.06
11	-0.02	-0.01	-0.02	-0.03	-0.04	-0.05	-0.06	-0.06	-0.06	-0.06	-0.06
21	-0.02	-0.02	-0.02	-0.03	-0.04	-0.05	-0.06	-0.06	-0.06	-0.06	-0.06
Oct 1	-0.02	-0.02	-0.03	-0.03	-0.04	-0.05	-0.06	-0.06	-0.06	-0.06	-0.06
11	-0.03	-0.03	-0.03	-0.04	-0.04	-0.05	-0.06	-0.06	-0.06	-0.06	-0.06
21	-0.03	-0.03	-0.03	-0.04	-0.04	-0.05	-0.06	-0.06	-0.06	-0.06	-0.06
Nov 1	-0.03	-0.03	-0.03	-0.04	-0.04	-0.05	-0.06	-0.06	-0.06	-0.06	-0.06
11	-0.03	-0.03	-0.03	-0.04	-0.04	-0.05	-0.06	-0.06	-0.06	-0.06	-0.06
21	-0.03	-0.03	-0.03	-0.04	-0.05	-0.05	-0.06	-0.06	-0.06	-0.06	-0.06
Dec 1	-0.03	-0.03	-0.03	-0.04	-0.05	-0.05	-0.06	-0.06	-0.06	-0.06	-0.06
11	-0.00	-0.02	-0.03	-0.04	-0.05	-0.05	-0.06	-0.06	-0.06	-0.06	-0.06
21	-0.01	-0.02	-0.03	-0.04	-0.05	-0.05	-0.06	-0.06	-0.06	-0.06	-0.06

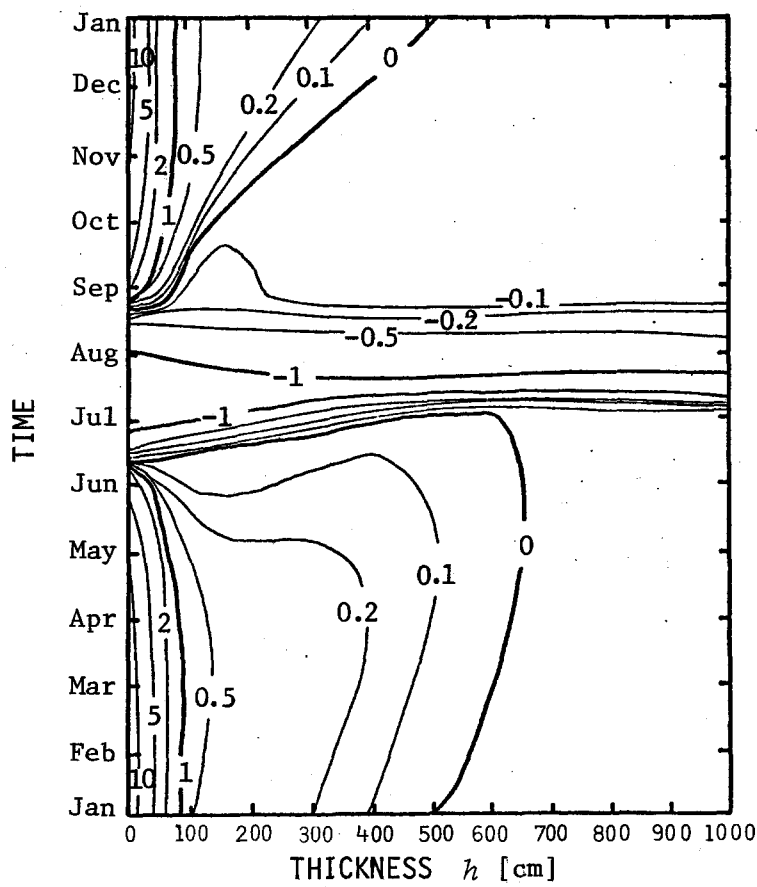


Fig. 4.1. Contours of f in cm day^{-1} as a function of thickness and time.

the upper surface are incoming long-wave and short-wave radiation fluxes, sensible and latent heat fluxes, and rate of snow accumulation; for these, we have used the upper surface energy fluxes suggested by Fletcher [1965] for the central Arctic. The only information needed about the underside of the ice is the magnitude of the oceanic heat flux, which, under level ice, is believed to be on the order of $2 \times 10^3 \text{ erg cm}^{-2} \text{ sec}^{-1}$ [Badgley, 1966; Untersteiner, 1964; Maykut and Untersteiner, 1969, 1971]. Application of this model is restricted to a description of growth rates and temperatures in level, undeformed ice that is past the early stage of growth when brine rejection is rapid. Hence, these rates were used for ice in the 100 cm to 400 cm range.

4.2.2 Thin Ice

The formation and initial growth of sea ice is accompanied by large changes in the amount of entrapped brine and by salinity-induced convection in the underlying ocean, processes which are incompletely understood and difficult to treat theoretically. In some ways, however, the growth of thin ice is simpler than the growth of thicker ice:

1. Thin ice has a low thermal mass and responds rapidly to changes in surface temperature, so that we need not know its thermal history in detail.
2. Approximately 99% of the heat lost from rapidly growing ice is derived from latent heat release; the oceanic heat flux is therefore negligible.
3. Given the low rate of snowfall in the Arctic during most of the winter, the ice is essentially snow free for the first week or so of its existence.

For these reasons, empirical formulas have been used with substantial success to predict the growth of thin ice. Here, we have chosen the formula of Anderson [1961]:

$$\zeta^2(t_0, t) + b_1 \zeta(t_0, t) = b_2 \int_{t_0}^t [T_f - T(t')] dt' \quad (4.13)$$

where $\zeta(t_0, t)$ is the thickness the ice attains at time t starting with zero thickness at time t_0 , $T(t')$ is the air temperature near the surface of the ice, T_f is the freezing point (assumed to be 0°C in these calculations), and b_1 and b_2 are constants with $b_1 = 5.1$ cm and $b_2 = 7.75 \times 10^{-5}$ cm⁻² sec⁻¹. Anderson reports this equation to be valid for ζ up to about 80 cm. Differentiating eq. 4.13 with respect to time, we obtain the instantaneous growth rate as a function of thickness and time

$$f = \frac{d\zeta}{dt} = \frac{b_2 [T_f - T(t)]}{2\zeta + b_1}. \quad (4.14)$$

In the calculations discussed in section 5, we use a time step Δt of order one day. To ensure the correct daily growth in those examples, we do not use

instantaneous values of f , but rather the daily mean growth rate defined by

$$\hat{f} = \frac{\zeta(t_0, t + \Delta t) - \zeta(t_0, t)}{\Delta t} \quad (4.15)$$

Equation 4.13 can be used to eliminate t_0 in favor of thickness and time. It is \hat{f} which appears in Table 4.2. The air temperatures which were used in eq. 4.14 appear in Table 4.3.

For ice thicker than 50 cm, the increasing snow cover and thermal mass of the ice become significant; hence, we interpolate between the $f(50, t)$ value from Anderson's formula and the $f(100, t)$ value from the Maykut and Untersteiner ice model.

TABLE 4.3

AVERAGE AIR TEMPERATURE ($^{\circ}\text{C}$) OVER ARCTIC PACK ICE

[Derived from the heat balance of Fletcher (1965) and the model of Maykut and Untersteiner (1969, 1971)]

<i>Month</i> \ <i>Day</i>	1	11	21
January.....	-31.0	-31.3	-31.9
February.....	-32.8	-33.6	-34.3
March.....	-34.7	-33.8	-32.3
April.....	-29.7	-25.7	-21.4
May.....	-16.6	-12.3	- 7.9
June.....	- 4.1	- 0.5	0.0
July.....	0.0	0.0	0.0
August.....	0.0	0.0	- 0.1
September.....	- 5.3	- 8.7	-12.1
October.....	-15.5	-19.0	-22.5
November.....	-26.0	-28.7	-30.4
December.....	-30.9	-30.8	-30.8

4.2.3 Thick Ice

Level, undeformed ice in the Arctic rarely exceeds a thickness of 4 m, while pressure ridges can reach thicknesses of several tens of meters. Although little is known about growth rates of ridge keels, a few observations [Welch et al., 1973] indicate that thicker ridges (greater than 8 m) undergo continued ablation throughout the year. New ridge keels, which are

composed of angular blocks, entrap ocean water so that they are isothermal; ablation rates must therefore be determined solely by the magnitude of the oceanic heat flux. Thick multiyear ridges are more solid, but vertical temperature gradients should still be small in the keels, and conductive heat losses negligible; ablation rates again must be dependent primarily on the oceanic heat flux. The mean oceanic heat flux of $2 \cdot 10^3$ erg cm $^{-2}$ sec $^{-1}$ corresponds to an ablation rate of about $-.06$ cm day $^{-1}$. However, movement of the keels relative to the water causes mechanical mixing and presumably increases the heat exchange between the cold mixed layer and the warmer underlying water. No estimates are available on the resulting increase in the oceanic heat flux and keel ablation. It is probable that for ridged ice, f is a function not only of h , but also the shape of the keel. Lacking hard data, we have assumed that $f(h,t) = -.06$ cm day $^{-1}$ for $h \geq 800$ cm. Between 400 cm and 800 cm, we have assumed that values from the Maykut and Untersteiner model for level ice (f_L) are applicable, but become increasingly unrealistic as h approaches 800 cm. To account for this effect we have taken

$$f(h,t) = \alpha f_L(h,t) + (1 - \alpha)(-.06 \text{ cm day}^{-1}), \quad 400 \text{ cm} \leq h \leq 800 \text{ cm} \quad (4.16)$$

where α is $(800 \text{ cm} - h)/400 \text{ cm}$. We are not confident about growth rates for ice thicker than 500 cm, and it is possible that we have seriously underestimated them. Field observations are needed before this can be determined.

4.3 The Redistribution Function

We assume $\Psi(h, \dot{\xi}^p, G)$ to have the form of equation 2.21, in which $\dot{\xi}$ is taken to be $\dot{\xi}^p$. The ridging coefficient is taken to be

$$\alpha_r = \frac{1}{2} (1 - \cos \theta) \quad (4.17)$$

which is compatible (by eq. 3.26) with the circular yield surface described in the following subsection. Then the opening coefficient is

$$\alpha_0 = \frac{1}{2} (1 + \cos \theta). \quad (4.18)$$

We have chosen arbitrarily a ridging mode $W_r(h)$ of type (3) described in section 2.3. We have taken

$$B(G) = \begin{cases} \frac{G}{G^*} \left(2 - \frac{G}{G^*}\right), & 0 < G < G^*, \\ 1, & G > G^*, \end{cases} \quad (4.19)$$

where G^* has been chosen to be 0.15. It will be recalled that if an amount of open water $\geq G^*$ exists, no ridging (and therefore no floe interaction) takes place. As a point of comparison, the void surrounding closely packed circles on a plane is $1 - \pi/2\sqrt{3}$, or about 0.09 and the void surrounding a circle inscribed in a square is $1 - \pi/4$, or about 0.21.

We have assumed that ice of any thickness, if ridged, becomes five times its original thickness

$$\hat{h} = \frac{1}{5} h. \quad (4.20)$$

Figure 4.2 shows that this thickness lies between the thickness that would

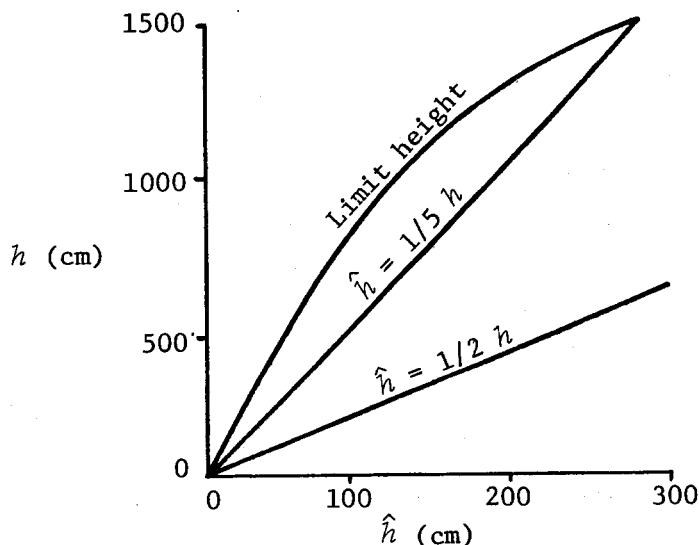


Fig. 4.2. Various one-to-one redistributions. Ice of thickness \hat{h} is piled into ice of thickness h .

be produced if the ice rafted ($\hat{h} = 1/2 h$) and the limiting height predicted by Parmerter and Coon [1973]. (Using Parmerter and Coon's Figure 12, we assign the values $G = 5$, $E = 10^{10}$ dyn cm $^{-2}$, $\rho_w = 1.03$ gm cm $^{-3}$, $v = 0.3$, $\sigma_c = 3.5 \cdot 10^6$ dyn cm $^{-2}$, $\rho_r = \rho_i = 0.92$ gm cm $^{-3}$, and $\theta = 25^\circ$. We obtain a limit height given approximately by $h = 53.4 \hat{h}^{0.59}$ with h and \hat{h} in centimeters.) This assumption ($\hat{h} = 1/5 h$) violates the limit height when ice thicker than about 300 cm ridges, but, in the examples discussed in section 5, such thick ice never ridges.

With the linear ridging law (4.20), equation 2.19 gives

$$N(h) = \frac{1}{5} A\left(\frac{h}{5}\right).$$

Then, from equation 2.11, we have

$$w_r(h) = \frac{-A(h) + \frac{1}{5} A \frac{h}{5}}{1 - \frac{1}{5}}$$

where $A(h) = B(G(h))$. The opening mode $w_o(h)$ is simply the Heaviside function $H(h)$.

4.4 The Yield Curve

We think, for reasons presented in section 3.4, that the yield curve for pack ice should be confined to the quadrant in which both principal stresses are negative. Nonetheless, in the examples discussed in section 5, we have used the circular yield curve

$$\begin{aligned} F(g, p^*) &= 2\left[\left(\sigma_I + \frac{p^*}{2}\right)^2 + \sigma_{II}^2 - \left(\frac{p^*}{2}\right)^2\right] \\ &\equiv \left(\sigma_1 + \frac{p^*}{2}\right)^2 + \left(\sigma_2 + \frac{p^*}{2}\right)^2 - \left(\frac{p^*}{2}\right)^2, \end{aligned} \quad (4.21)$$

or, equivalently,

$$F\left(\frac{\sigma_I}{p^*}, \frac{\sigma_{II}}{p^*}\right) = \left(\frac{\sigma_I}{p^*} + \frac{1}{2}\right)^2 + \left(\frac{\sigma_{II}}{p^*}\right)^2 - \left(\frac{1}{2}\right)^2.$$

The main arguments for using a circular yield curve in this study are computational, not physical.

5. THE RESPONSE OF AN ELEMENT OF PACK ICE TO SPECIFIED DEFORMATIONS

5.1 Introduction

In the preceding sections we have built up a model of sea ice using rather simple notions about the mechanisms which allow the ice to move; it breaks apart easily in tension and builds ridges in compression, converting mechanical work into potential energy. In this section we begin to transfer our emphasis from reasoning about the microscale events to studying the behavior of the model on the larger, geophysical scale. We ask: what is the strength of the ice pack and how does it change? what is the stress required to deform the pack? To answer these questions, we observe the response of a large-scale element in a series of simple examples. But to see *why* the large-scale element behaves as it does, we examine the detailed manner in which changes in the thickness distribution affect the properties of the element.

The behavior of the model will be explored and must pass tests of reasonableness. But in no sense are we testing the model by comparing predictions against actual measurements. The present treatment seemed sufficiently complex to require a full sounding of the thermal and mechanical response of a single element of material before undertaking the solution of the field equations. Previous workers have skipped this step, because the mechanical assumptions in their models were more readily comprehensible.

The strain rate time series is specified for the calculations reported here, obviating the need to solve or even consider a momentum equation. Hence, we refer to these examples as construed motions. Given the stress state and an increment of strain to be made during the next time step, the new stress is calculated from the elastic equations. If this stress lies within the yield curve, it is the correct stress, and the correct state is elastic. If this stress lies outside the yield curve, the state is plastic and the plastic stress is found from the plastic flow rule and yield curve. The thickness distribution equation is integrated using only the plastic strain rates (which are zero if the state is elastic). New values of the

elastic moduli and the plastic yield strength are computed from the thickness distribution to complete one cycle of the calculations. This sequence of calculations is shown in Figure 5.1.

A progression of simple cases is considered, as summarized in Tables 5.1 and 5.2. The discussion of each case begins with a look at the behavior of the thickness distribution and concludes with remarks about the state of stress in the element. The calculations show us what stresses are required to produce specified deformations in a test sample of material described by the model equations; it is completely fair to imagine either that the stresses cause the deformation or that the deformation causes the stresses. These results have also been presented in a paper by Coon and Pritchard [1974], but with less emphasis on the thickness distribution.

TABLE 5.1

TEST MOTIONS FOR THE CASES DISCUSSED IN SECTION 5

Description	Thermodynamics typical of:	$\dot{\epsilon}_{xx}$	$\dot{\epsilon}_{xy}$	$\dot{\epsilon}_{yy}$	Time
Thermodynamics only - sec. 5.2	January	0	0	0	
Isotropic deformation - sec. 5.3	January	$\begin{cases} 0.5\% \text{ day}^{-1} \\ -0.5\% \text{ day}^{-1} \end{cases}$	0	$0.5\% \text{ day}^{-1}$	$0 \leq t \leq 10 \text{ days}$
			0	$-0.5\% \text{ day}^{-1}$	$10 < t \leq 30 \text{ days}$
Uniaxial deformation - sec. 5.4	January	$\begin{cases} 1\% \text{ day}^{-1} \\ -1\% \text{ day}^{-1} \end{cases}$	0	0	$0 \leq t \leq 10 \text{ days}$
			0	0	$10 < t \leq 30 \text{ days}$
Pure shear deformation - sec. 5.5	January	$\begin{cases} 0 \\ 0 \end{cases}$	$0.5\% \text{ day}^{-1}$	0	$0 \leq t \leq 10 \text{ days}$
			$-0.5\% \text{ day}^{-1}$	0	$10 < t \leq 30 \text{ days}$
AIDJEX 1972 pilot study - sec. 5.6	Mar.-Apr. 1972	Strain rates given in Figure 5.25			

5.2 Thermodynamics Only

The thermodynamic forcing $f(h, t)$ does not change throughout these calculations and acts therefore as a common theme in the discussions of the results. In fact, time in these examples has been limited to the winter and spring months, when $f(h)$ has the form plotted in Figure 5.2 and the

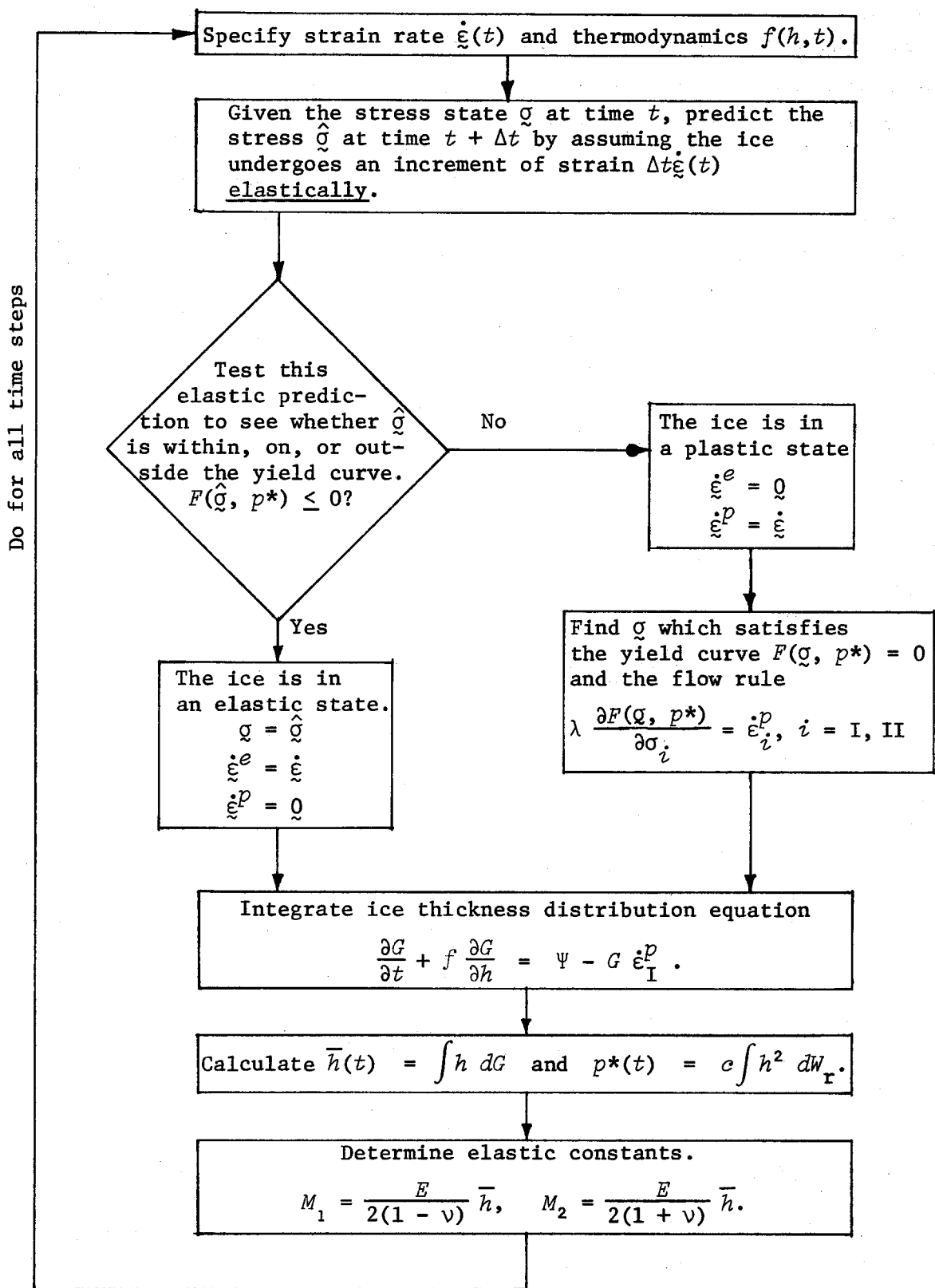
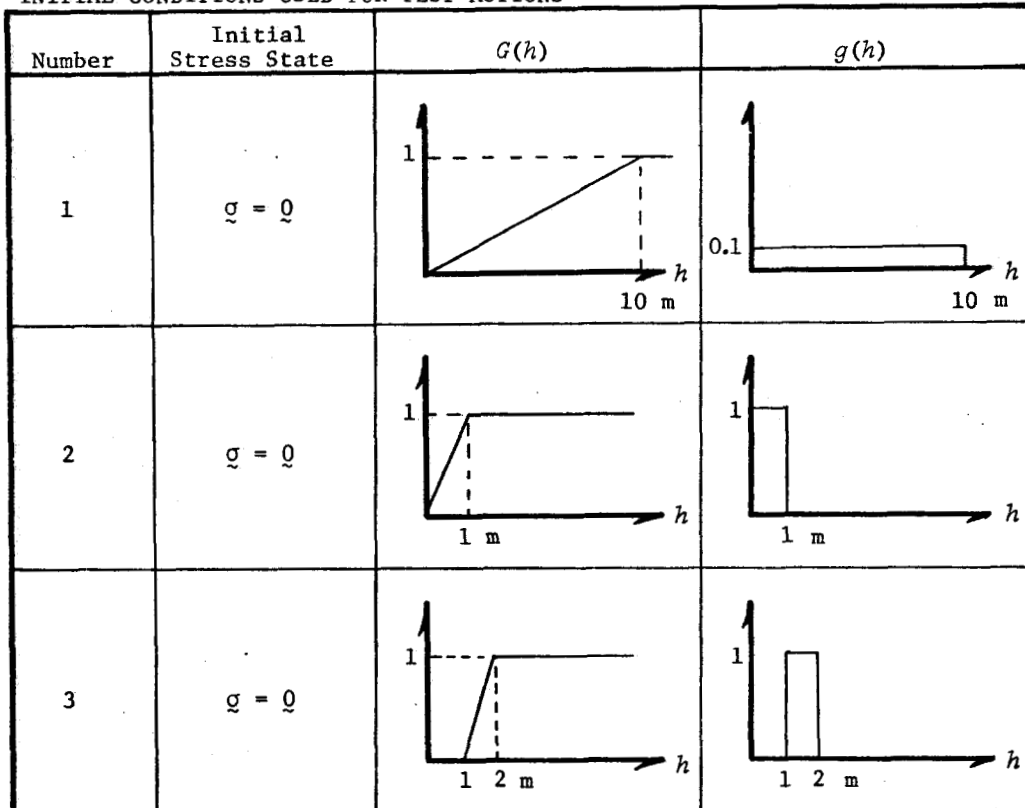


Fig. 5.1. Schematic diagram of constrained motion calculation.

TABLE 5.2

INITIAL CONDITIONS USED FOR TEST MOTIONS



temporal variation is small. To understand the consequences of the thermodynamics, we consider a case in which the rates of deformation are zero. We have only to solve the homogeneous equation $\partial G/\partial t + f(\partial G/\partial h) = 0$ subject to some initial condition $G(h,t=0)$. The boundary conditions are $G(h=0,t) = 0$ and $G(h=h_{\max},t) = 1$, as they are in all other cases.

One helpful way to consider solutions is to think of a value of G (or g) at each point in the (h,t) plane. For this case, the solution is conceptually simple. The value of G is maintained along a characteristic, which is a line in the (h,t) plane with slope $f (\equiv dh/dt)$. (See Appendix A.) The initial value $G(h,0)$ determines G on characteristics intersecting the h axis. On other characteristics the boundary values $G(0,t) = 0$ or $G(h_{\max},t) = 1$ are maintained. Starting with the initial condition 1, as shown in Figure 5.3, we observe after some time interval a new distribution, shown by the broken line. To the right of 5 meters (where $f < 0$), the

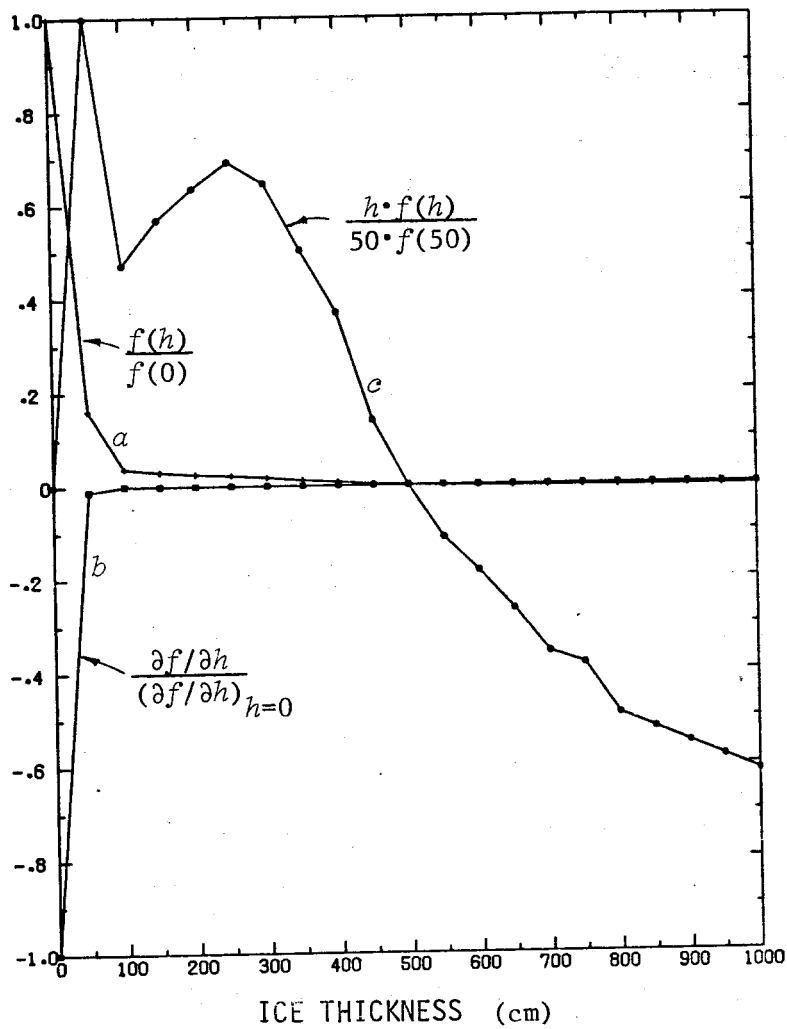
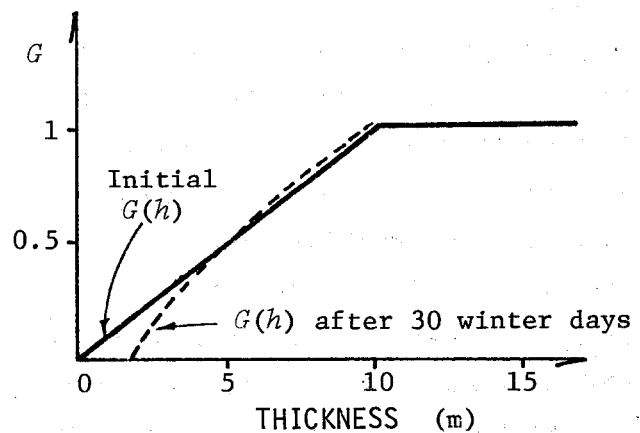


Fig. 5.2. The thermodynamic function $f(h)$ for winter and spring conditions. Also plotted are $\frac{\partial f}{\partial h}$ and hf , all normalized for convenience. Data are taken from Table 4.2.

Fig. 5.3. A sketch of how the uniform initial distribution changes in time.



characteristics have carried constant values of G to the left; to the left of 5 meters, constant values of G have moved to the right.

Since we use the lowercase $g(h,t)$ when it is easier to interpret, we point out here that although, in this case, G is maintained along the characteristic, g is not. Just by differentiating, we see that

$$\frac{\partial G}{\partial t} + f \frac{\partial G}{\partial h} = 0$$

implies that

$$\frac{\partial g}{\partial t} + f \frac{\partial g}{\partial h} = -g \frac{\partial f}{\partial h}. \quad (5.1)$$

The term $-g \frac{\partial f}{\partial h}$ has an immediate geometric interpretation: $\partial f / \partial h$ measures the rate at which characteristics in (h,t) space (Fig. 2.3 and 2.4) converge or diverge in time. Now $g(h)dh = G(h + dh) - G(h)$. Therefore, as we follow the characteristics through (h,t) and $(h + dh, t)$, they come closer together (i.e., dh decreases) where $\partial f / \partial h < 0$, and G remains constant along them; the value of $g(h)$ must increase. Figure 5.2 shows $\partial f / \partial h$. Clearly the "convergence of characteristics" effect is important mainly for $h < 100$ cm. The development of $g(h,t)$, beginning with initial condition 1, is sketched in Figures 5.4 and 5.5.

For the example just described, then, the main features of the solution for g are (1) the rightward movement along the $(0,0)$ characteristic of the value $g = 0$, (2) the leftward movement along the $(10 \text{ m}, 0)$ characteristic of the value $g = 0$, and (3) the modification of g , along intermediate characteristics, in proportion both to $(-g)$ and to $\partial f / \partial h$, which is small and negative for $h \geq 100$ cm.

The yield strength is influenced only by the area of ice thinner than h^* , that is, the thinnest 15%. As this thin ice grows thicker in winter, it becomes stronger. Thin ice grows and strengthens more quickly than thick ice, so that the thermodynamics tends to reduce initial differences in strength (Fig. 5.6).

Fig. 5.4. The thermodynamic development of $g(h, t)$.

Because the melt rates for thick ice are quite small, the time required to reach the "spike" equilibrium thickness is on the order of a decade.

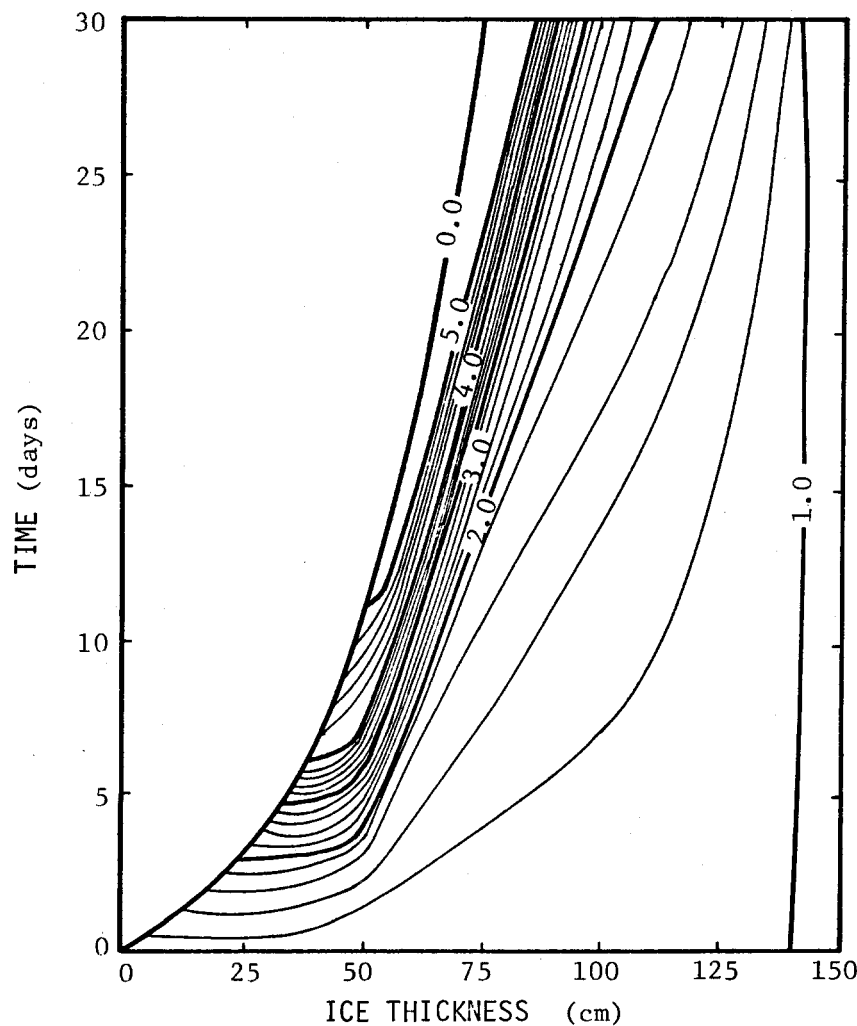
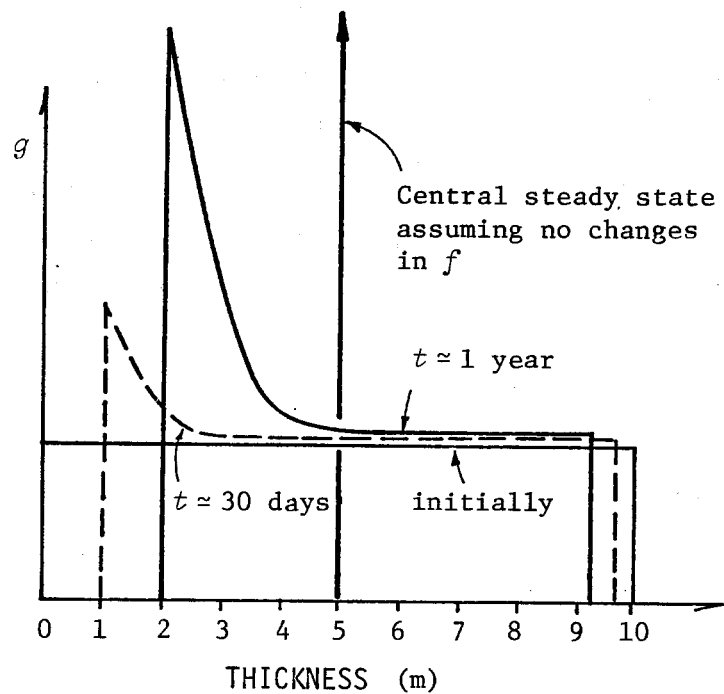
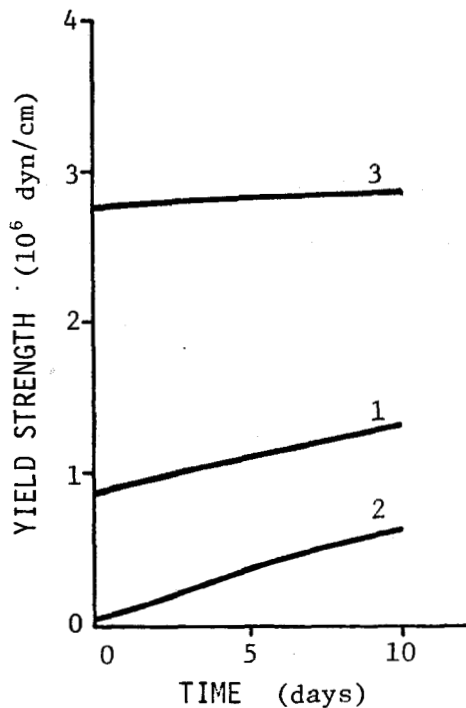


Fig. 5.5. Contours $g(h, t)$ in units of 10^{-3} cm^{-1} under the influence of thermodynamics alone, for initial condition 1 (Table 5.2).

Fig. 5.6. Changes in the yield strength p^* caused by thermodynamics alone. Numbers refer to initial conditions (Table 5.2).



This solution, with no deformation and therefore no inhomogeneous terms in the G equation, is the simplest kind of thermodynamic wave. Sections 5.3-5.6 will illustrate how deformation modifies this wave.

5.3 The Isotropic Case

Now we ask how the pure thermodynamic wave is modified if we add isotropic deformation. We examine a case in which 10 days of pure divergence are followed by 20 days of pure convergence. For this purpose we will consider the g equation (with no advection)

$$\left(\frac{\partial}{\partial t} + f \frac{\partial}{\partial h} \right) g = -g \frac{\partial f}{\partial h} - g \operatorname{div} \vec{v} + \psi \quad (5.2)$$

obtained by differentiating eq. 2.6 with respect to h and defining $\psi \equiv \partial \Psi / \partial h$.

5.3.1 Diverging Motion

Isotropic divergence introduces two additional effects. Some ice is exported from the area (by the term $-g \operatorname{div} \vec{v}$), and the ice within the area

pulls apart, creating open water (at a rate $\psi = + \operatorname{div} \tilde{v} \delta(h)$) in the area once covered by the exported ice. Since $f(h=0, t) < 0$, the open water freezes instantly, so that no finite area of open water ever develops.

The part of the thermodynamic wave to the right of the ($h=0, t=0$) characteristic is unaffected by the term ψ and is only slightly modified by the term $-g \operatorname{div} \tilde{v}$ in equation 5.2. Compare the first ten days of the contour plot of $g(h, t)$ in Figure 5.7 with Figure 5.5; also compare the schematic three-dimensional view of $g(h, t)$ in Figure 5.8 with Figure 5.4. We see, from Figure 5.9, that the term $-g \operatorname{div} \tilde{v}$ in this example is small compared to $-g(\partial f / \partial h)$.

To the left of the $(0,0)$ characteristic, the wave is qualitatively changed by the divergence because the opening provides a continuous source of thin ice which was lacking in the previous case. This source holds the value of $g(h=0^+, t)$ at a value $\operatorname{div} \tilde{v} / f(h=0)$. To obtain this result, we must recognize that the rate of creation of open water $\psi = \delta(h) \operatorname{div} \tilde{v}$ is balanced by the rate of removal of open water by thermodynamics $f(h=0)(\partial g / \partial h)_{h=0^+}$. Equating these two quantities gives

$$\left(\frac{\partial g}{\partial h} \right)_{h=0^+} = \frac{\operatorname{div} \tilde{v}}{f(h=0)} \delta(h) \quad (5.3)$$

which implies the desired result.

The solution to the left of the $(0,0)$ characteristic can best be understood by supposing f to be steady, a good approximation during winter months. The solution to eq. 5.2, then, can be written

$$g = \frac{\operatorname{div} \tilde{v}}{f(h)} \exp \left\{ -\operatorname{div} \tilde{v} \int_0^h \frac{dh}{f} \right\}, \quad 0 < h < H(t) \quad (5.4)$$

where $h = H(t)$ denotes the $(0,0)$ characteristic.

Figure 5.10 shows this solution. The rate of adjustment to this steady solution (5.4) is large for intermediate values of h (say, $H < h < 50$ cm) where the term $-g(\partial f / \partial h)$ dominates, but decreases rapidly in h .

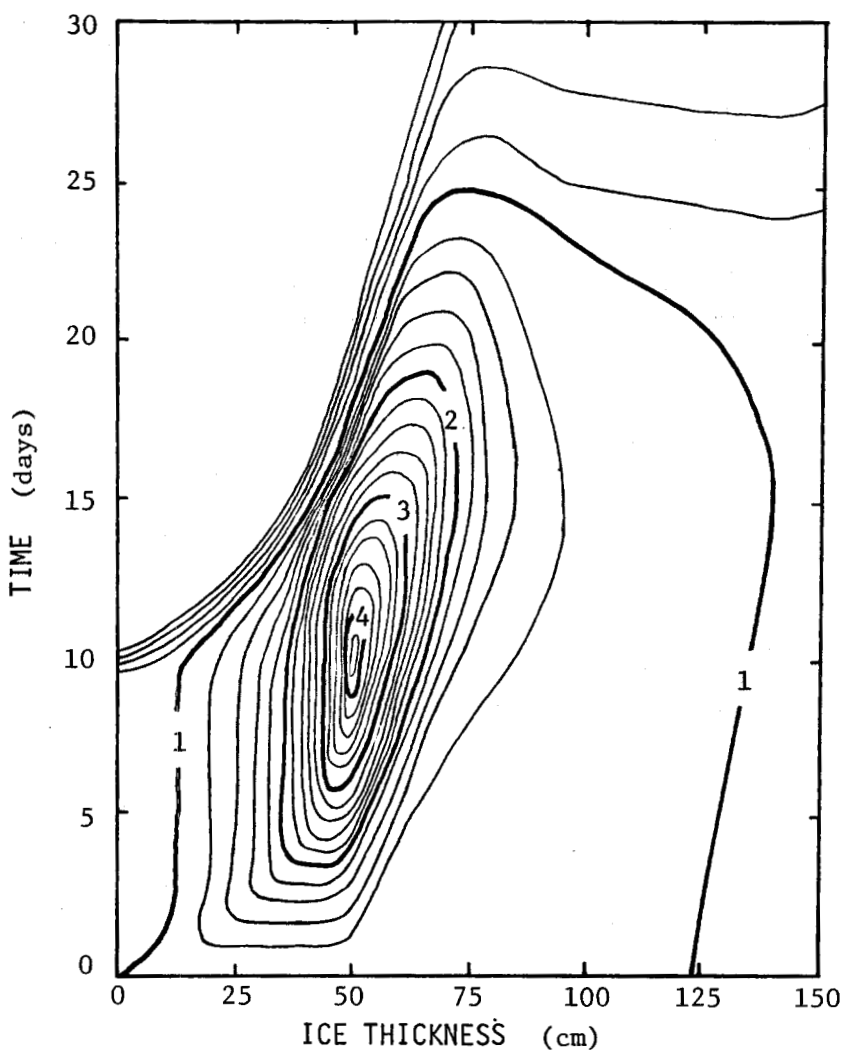
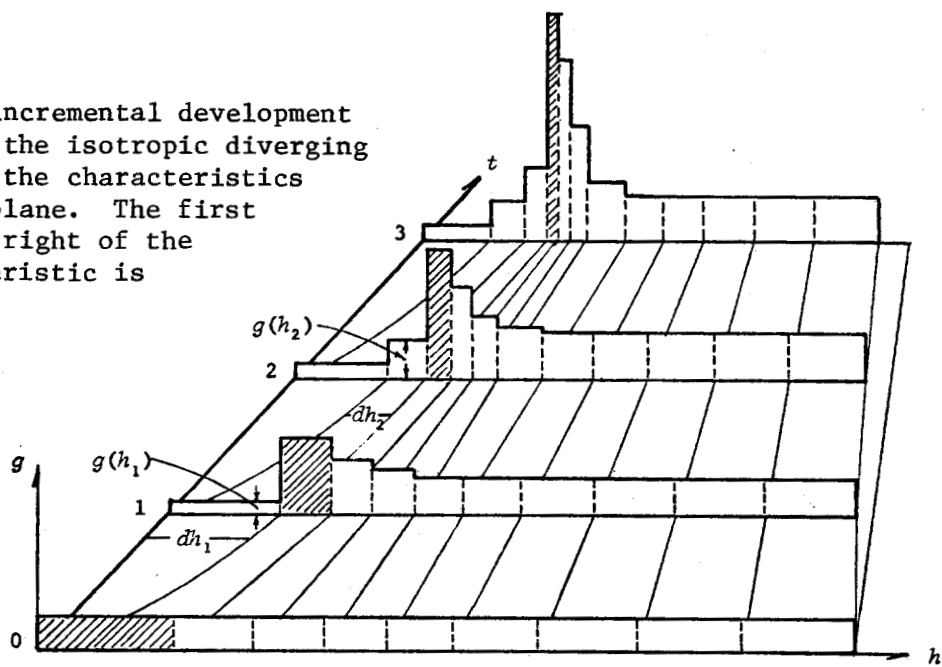


Fig. 5.7. Contours $g(h,t)$ in units of 10^{-3} cm^{-1} under the influence of thermodynamics and isotropic motions. Starting with initial condition 1 (Table 5.2), the ice diverges for 10 days and then converges for 20 days.

Fig. 5.8. An incremental development of $g(h,t)$ for the isotropic diverging case, showing the characteristics in the (h,t) plane. The first column to the right of the $(0,0)$ characteristic is shaded.



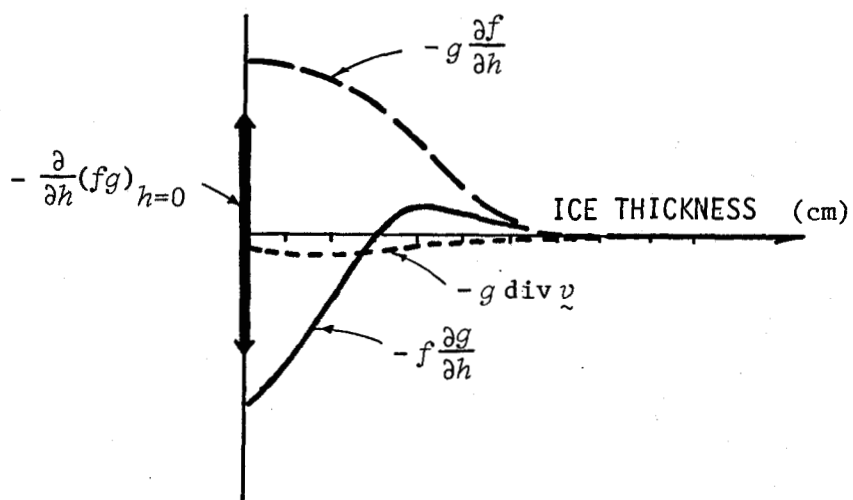


Fig. 5.9. Terms in the g -equation (5.2) at $t = 1$ day. The $(0,0)$ characteristic has reached the point $h = 12$ cm.

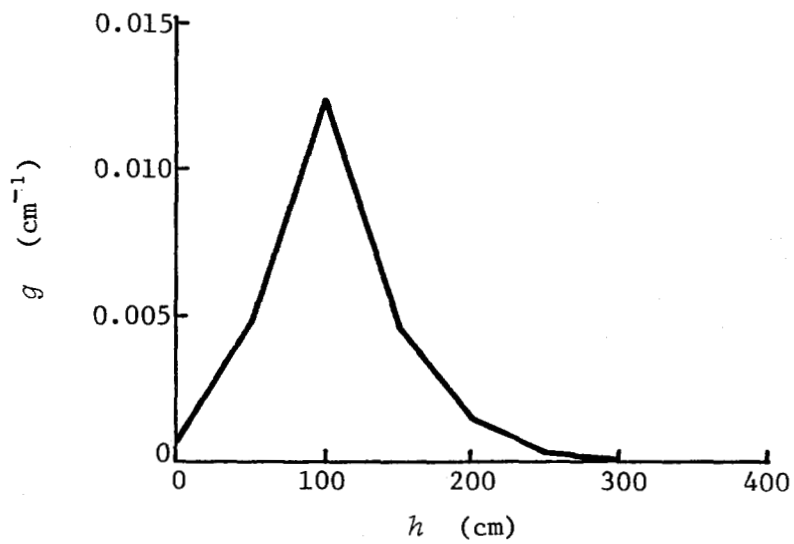


Fig. 5.10. The approximate solution (5.4) which applies to the left of $h = H(t)$; $H(1$ day) = 12 cm and $H(10$ days) \approx 50 cm.

To summarize: The combined effect of winter thermodynamics and constant isotropic divergence is to maintain a steady distribution of ice thickness for thicknesses to the left of the $(0,0)$ characteristic. The rest of the solution depends on the initial condition or on the boundary condition $g(h_{\max}, t) = 0$.

The yield strength is affected by two processes: (1) the material strengthens because it is growing thicker; and (2) the material weakens because the area of open water or thin ice is increased by the divergent motion. Yield strength histories are compared in Figure 5.11 for the three initial conditions. Weakening induced by the divergence dominates when there is little thin ice present initially (no ice thinner than 1 m for initial condition 3). The divergent motion of 1% per day for 10 days reduces initial differences in yield strength.

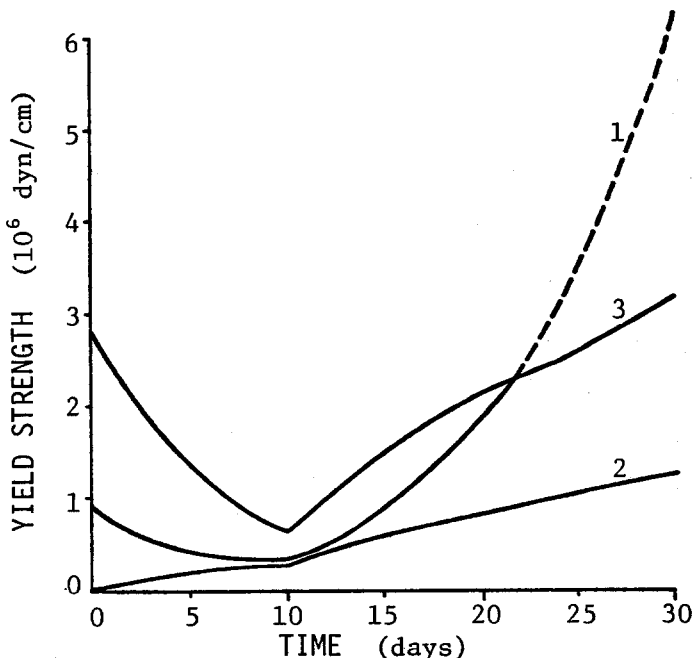


Fig. 5.11. A comparison of the yield strength histories for the isotropic case, for the three initial conditions. The motion was divergent before and convergent after $t = 10$ days.

To illustrate the stress state history, we have found it useful to normalize the stress by p^* . The stress history is then given in two parts: the yield stress history (already presented in Fig. 5.11) and the position of the stress state on the normalized yield curve (Fig. 5.12).

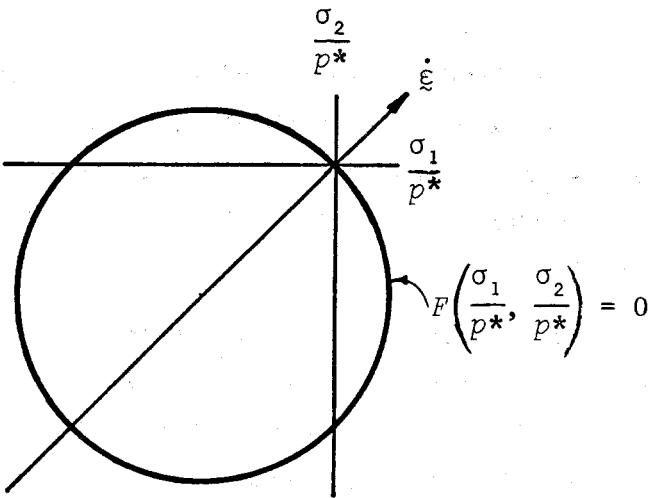


Fig. 5.12. Normalized yield curve in principal stress space.
The arrow indicates isotropic divergence.

The initial state chosen for this example is stress free, $\sigma = 0$. Throughout the divergent motion, the stress state remains at $\sigma = 0$. The stress state is plastic because it is on the yield curve. This is the only point on the yield curve that does not vary as p^* changes. We will see later in more complicated motions that a constant strain rate and changing yield strength generally combine to change the stress state.

It is important to ask what effect the initial stress state has on the stress history. We know that the history of former stress states is "forgotten" as soon as plastic flow begins. Thus, under a constant strain rate, the maximum memory time is the time required for the stress to traverse the yield curve. This is

$$\Delta t \approx \frac{p^*(0)}{M_1 \dot{\epsilon}_{ii}(0)} .$$

For the three initial conditions investigated in this work, Δt ranges from a minimum of 2 minutes for the initial thickness distribution of thin ice (0-1 m uniform) to a maximum of 4 hours for the intermediate thickness distribution (1-2 m uniform). Since each transit time is less than a time step in the calculation (12 hours), the material will automatically be plastic after one cycle. Thus, the initial stress state is eliminated immediately by the stiff elastic behavior of the ice. This phenomenon has been observed for all cases reported in this work.

5.3.2 Converging Motion

After 10 days the divergence is changed to isotropic convergence and allowed to proceed for a 20-day period. The behavior of the ridging mode is of primary interest here, since the thermodynamics is unaltered. At each time, W_r , which equals $\Psi/|\dot{\xi}^P|$, is constructed following the development in section 2.3 and 4.3.

A typical situation is shown in Figure 5.13 for $t = 20$ days. Two segments of the h axis concern us here: (h_0, h^*) , the ice going into the ridging process; and $(5h_0, 5h^*)$, the ice coming out of it. (In section 2, h_0 was defined as the thinnest ice present and h^* as the thickest ice being ridged.) When h_0 is small, the intervals may overlap, $(5h_0 < h^*)$, but this does not change anything. The sum of the functions $-a(h)$ and $n(h)$ defined on these intervals can be integrated to get $W(h)$. The shape of W_r (Fig. 5.14a,b) is quite general. W_r will always show a minimum value in $(h^*, 5h_0)$ or, if the intervals overlap, in $(5h_0, h^*)$. For thicknesses to the left of the minimum, the area of ice is being decreased by the redistribution process, and to the right of the minimum it is being increased. At the minimum itself, either nothing is happening or the area of ice going into ridging exactly equals the area coming out.

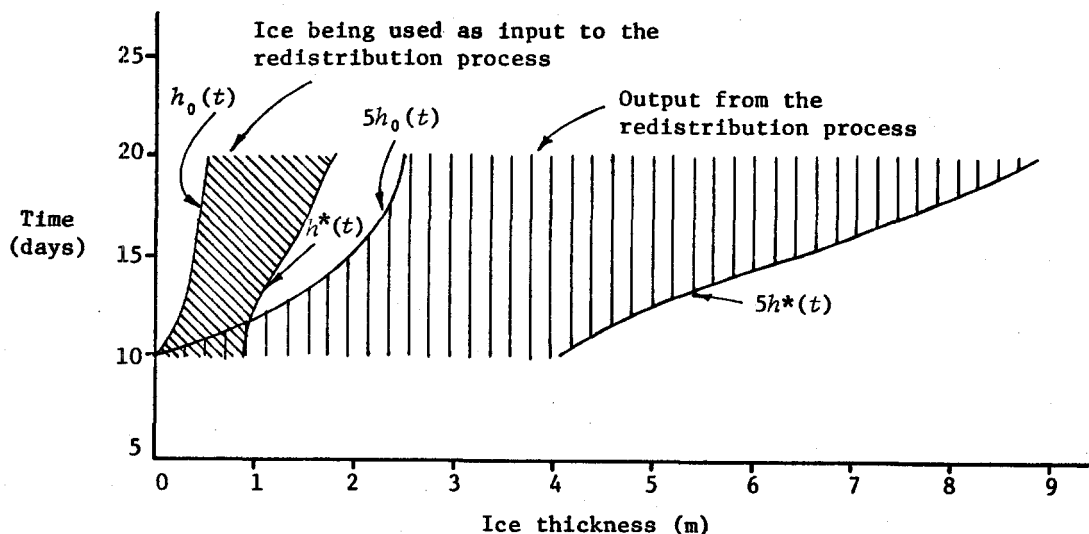


Fig. 5.13. The regions in (h, t) space which participate in the ridging process.

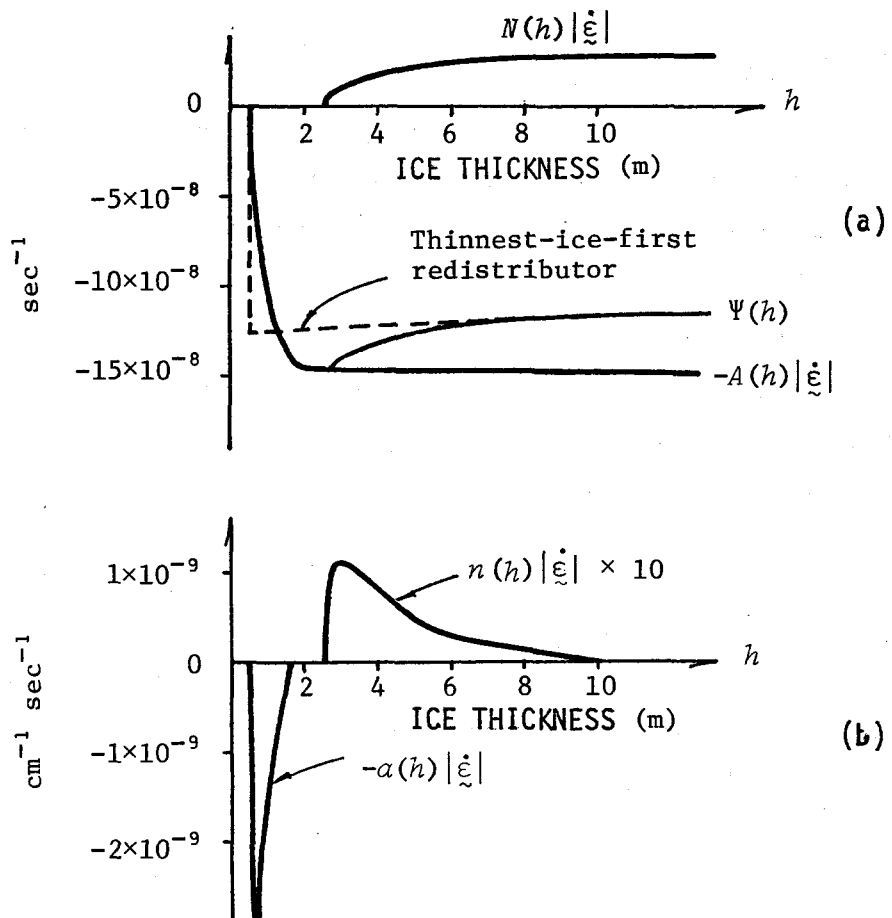


Fig. 5.14. (a) The upper case redistribution function and its components. For comparison, the thinnest-ice-first, uniform redistributor of Thorndike and Maykut [1973] is sketched as well. (b) Components of the lower case redistribution function.

The point $h_0(t)$ on the h axis is the thickness of the thinnest ice actually present at any given time. As we have seen, $h_0(t)$ is always zero during divergence. But now, in pure convergence--and only in pure convergence--there is no source of thin ice and h_0 can move to the right. Ignore for the moment the effect of thermodynamics at h_0 . At a point $h_0 + \Delta$ just to the right of h_0 , the value of G will change because of the $-G \operatorname{div} \vec{v}$ term (which is positive, but small) and because of the redistributor W_r . W_r reduces $G(h_0 + \Delta)$, but the rate depends on $G(h_0 + \Delta)$:

$$\begin{aligned}\Psi(h_0 + \Delta) &= |\dot{\xi}^p| W_r(h_0 + \Delta) \sim |\dot{\xi}^p| A(h_0 + \Delta) \\ &= |\dot{\xi}^p| B(G(h_0 + \Delta)) = |\dot{\xi}^p| G(h_0 + \Delta)(2G^* - G(h_0 + \Delta)) \quad (5.5)\end{aligned}$$

This quantity vanishes as $G(h_0 + \Delta)$ becomes small. Because the redistributor can never bring $G(h_0 + \Delta)$ to zero, it can never advance h_0 . This argument relies on the assumption, embedded in the particular choice of B , that the ridging process may use part of, but never all of, the ice of any thickness.

Nonetheless, h_0 does move because of the thermodynamics. Using a result from Thorndike and Maykut [1973], we have

$$\frac{dh_0}{dt} = \left(f - \frac{\Psi}{\partial G / \partial h} \right)_{h=h_0} \quad (5.6)$$

Our ridging mode W_r vanishes at $h = h_0$. In convergence, Ψ is simply $|\dot{\xi}^p| \alpha_r W_r$ and therefore vanishes as well. Hence,

$$\frac{dh_0}{dt} = f, \quad \text{for isotropic convergence.}$$

(Other redistributors, like the thinnest-ice-first rules, may have caused $h_0(t)$ to move; see Thorndike and Maykut, 1973.) In any other strain rate state, Ψ contains a term in the opening mode $|\dot{\xi}^p| \alpha_o^H(h)$ which requires $h_0 = 0$, and, hence, from eq. 5.6,

$$\left(f - \frac{\Psi}{\partial G / \partial h} \right)_{h=0^+} = 0 \quad \text{for any state other than isotropic convergence.}$$

The expression reduces to eq. 5.3 in the case of isotropic divergence.

The statement $dh_0/dt = f$ implies that h_0 follows a characteristic during isotropic convergence. The proper interpretation of the region to the left of $h_0(t)$ is not that all the ice less than $h_0(t)$ has been consumed by ridging, but that the ice which had zero thickness when the episode of convergence began has now grown thermodynamically to a thickness $h_0(t)$ and no new thin ice has been formed to take its place.

It is clear from the contour map of $g(h,t)$ in Figure 5.7 that most of the action occurs for thin ice, a consequence of conserving the volume of the redistributed ice. For every 5 units of area of ice of thickness h_1 going into the redistribution process, only one unit of area comes out with thickness $5h_1$.

During isotropic compression, the ridge in $g(h,t)$ which was created by the convergence of characteristics is gradually reduced by the ridging process. The thermodynamic tendency is still there, but it is masked by the dynamics which draws the most ice into the redistribution process from the peak in $g(h)$, thus reducing g more rapidly there than elsewhere. The peak in g , while being smoothed out, continues to move along a characteristic.

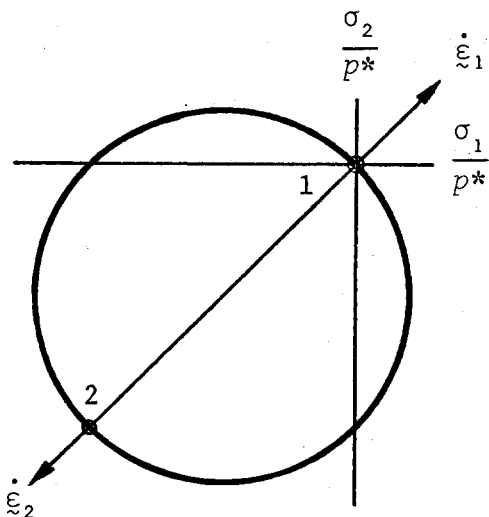
To summarize: Convergence is accomplished by converting an area of thin ice into a smaller area of thicker ice (conserving volume). The process tends to reduce peaks in $g(h)$ for $h < h^*$. There is no source of thin ice.

Calculated values for the yield strength are shown in Figure 5.11 for the three initial conditions. Although the diverging motion greatly reduces the differences in h^* for the three curves, these differences reappear during convergence. What has happened is that the thin ice created by divergence is piled up into ridges during convergence. After all the new ice has been used up, the ice that remains and must be used for ridging is strongly related to the assumed initial states. For example, at $t = 20$ days, the ice being ridged from initial condition 1 is between 55 and 185 cm; by contrast, the ice being ridged from initial condition 2 is between 55 and 68 cm. The present coding was not intended to treat cases in which h^* exceeds 200 cm. Since this did happen for initial condition 1, the dashed portion of that curve is only qualitatively valid.

In normalized principal stress space, the stress state lies at two points during this cycle of motion, shown in Figure 5.15. At the end of 10 days, the stress moves through the elastic interior of the yield curve from point 1 to point 2. The stress state then follows the yield strength

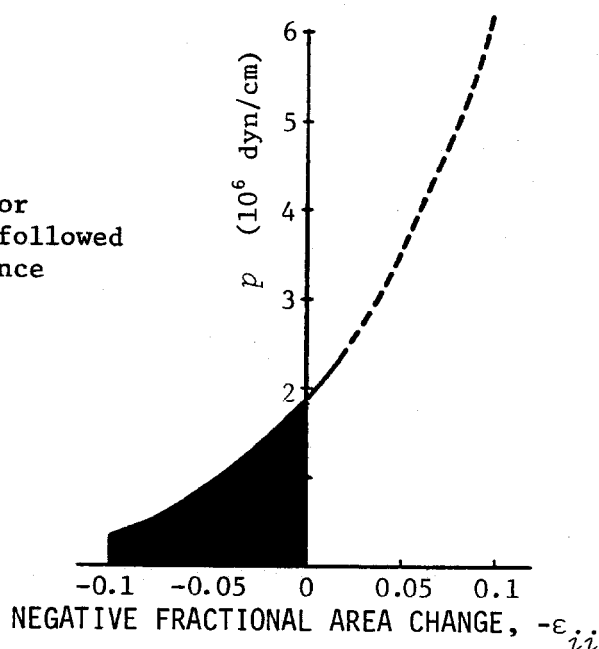
$$\sigma_{ij} = -p^* \delta_{ij} .$$

Fig. 5.15. Normalized yield curve in principal stress space. Strain rates $\dot{\varepsilon}_1$ and $\dot{\varepsilon}_2$ indicate isotropic divergence and convergence, respectively.



The stress-strain curve followed during the cycle of isotropic motion is presented in Figure 5.16. Although these data apply to initial condition number 1, they are typical of the other conditions. The curve shown is not a fundamental material property; it depends on the motion and on $g(h, t=0)$. The pressure remains at zero while the area increases by 10%, then rises quickly while the response is elastic, and finally continues to rise and follow the yield strength. Another period of divergence would cause the stress to drop quickly to zero.

Fig. 5.16. Stress-strain curve for 10 days of isotropic divergence followed by 20 days of isotropic convergence at the rate of 1.0% per day, for initial condition 1.



5.3.3 Changes in Potential Energy

Equation 2.27 shows how the thermodynamics and the dynamics alter the potential energy per unit area of the ice. One of the terms arises from the ridging mode of deformation and that term, by our assumption, must exactly equal the plastic work being done on the ice (section 3.3). The terms in the potential energy equation (2.27) and the plastic work are plotted versus time in Figure 5.17, starting with initial condition 1. The development of $g(h, t)$ was shown in Figure 5.8. The potential energy, PE , is seen to decrease during divergence and to increase during convergence, largely under the influence of the dominating term $-PE \operatorname{div} \underline{\nu}$.

The thermodynamic term is positive in this example because there is a fair amount of thin ice present. The integrand in that term is f_h , which during the winter has the shape sketched in Figure 5.2. This integrand f_h does not vanish for large h , which makes this term sensitive to the presence of very thick ice. In an area containing more thick ice, this integral could easily become negative.

The term $c \int h^2 d\Psi$ measures the increase of potential energy per unit area caused by ridging. In this example, this term is an order of magnitude smaller than the $\operatorname{div} \underline{\nu}$ term and an order larger than the thermodynamic term. It has been rigged to balance the rate of plastic work which is computed in the mechanical part of the model. We can estimate the increase in potential energy by ridging during the 10 days of convergence from the shaded area in Figure 5.17d:

$$\frac{1}{2} \times 2.3 \frac{\text{erg}}{\text{sec cm}^2} \times 10^{-1} \times 10 \text{ day} \times \frac{86,400 \text{ sec}}{\text{day}} \approx 1.0 \times \frac{10^5 \text{ erg}}{\text{cm}^2}$$

This just equals the plastic work done on the ice shown in Figure 5.17e and given by the shaded area in Figure 5.16:

$$1.0 \times 10^6 \text{ dyn cm}^{-1} \times 0.1 \approx 1.0 \times 10^5 \text{ erg cm}^{-2}$$

To get a feel for how much energy this is, note from equation 2.25 that 10^5 ergs is the difference in potential energy between an isostatic slab of ice 502 cm thick and one 500 cm thick.

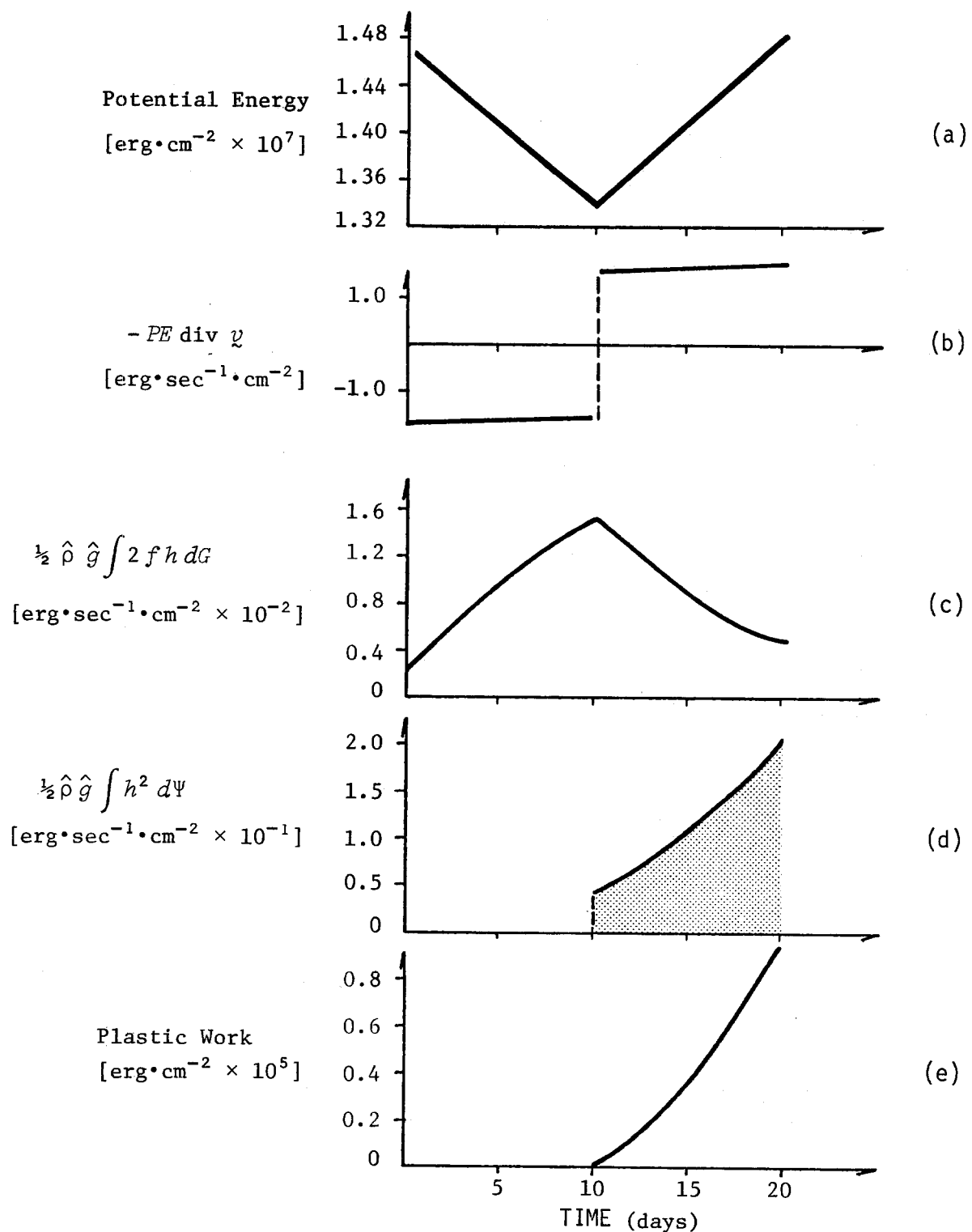


Fig. 5.17. (a) Changes in potential energy for 10 days of divergence followed by 10 days of convergence. (b), (c), and (d) Terms in eq. 2.27 for the rate of change of potential energy. (e) The plastic work $\int \xi \dot{\xi}^p dt$.

5.3.4 Some Limitations of the Isotropic Cases

In nature, and even in simple, idealized motions, the thermodynamic, opening, and ridging processes all act at once. Our model allows open water and pressure ridges to be created simultaneously, in contrast to the more limited Thorndike and Maykut [1973] model, which is basically one-dimensional. The proportions of opening and ridging are determined by α_o and α_r , which derive their functional form directly from the shape of the yield curve. In pure shear ($\theta = \pi/2$) we have $\alpha_o = \alpha_r = 0.5$. The uniaxial cases have $\alpha_o = 0.85$, $\alpha_r = 0.15$ for extension and $\alpha_o = 0.15$, $\alpha_r = 0.85$ for compression. Thus, even when the strain rate state is uniaxial extension, the model still builds some ridges and allows for the creation of open water during uniaxial convergence.

Whenever work is being done on the ice, some ridging must be present ($\alpha_r > 0$). This statement is true for any convex yield curve, provided only that the zero stress state is inside or on the yield curve. For the circular yield curve, only when the strain rate vanishes or the stress state becomes zero does the rate of work equal zero. The latter condition applies only under isotropic divergence; all other strain rate states do work on the ice and therefore must increase its potential energy by building pressure ridges. Similarly, only the isotropic convergent motion is free of any opening. The consequences of the circular yield curve do not entirely agree with our intuition about how the ice works. In subsequent study, the simplicity of that yield criterion will need to be weighed against more realistic, but less simple, representations using other yield criteria.

5.4 The Uniaxial Case

For uniaxial motion, we restrict our attention to how and why the abundance of ice of some particular thickness, 50 cm, say, changes. All of the processes discussed above come into play here except for the opening mode, which affects g only at $h = 0$. The remaining terms are sketched in Figure 5.18. In this calculation the ice is assumed to have initial condition number 1. The deformation consists of 10 days of extension followed by 20 days of compression.

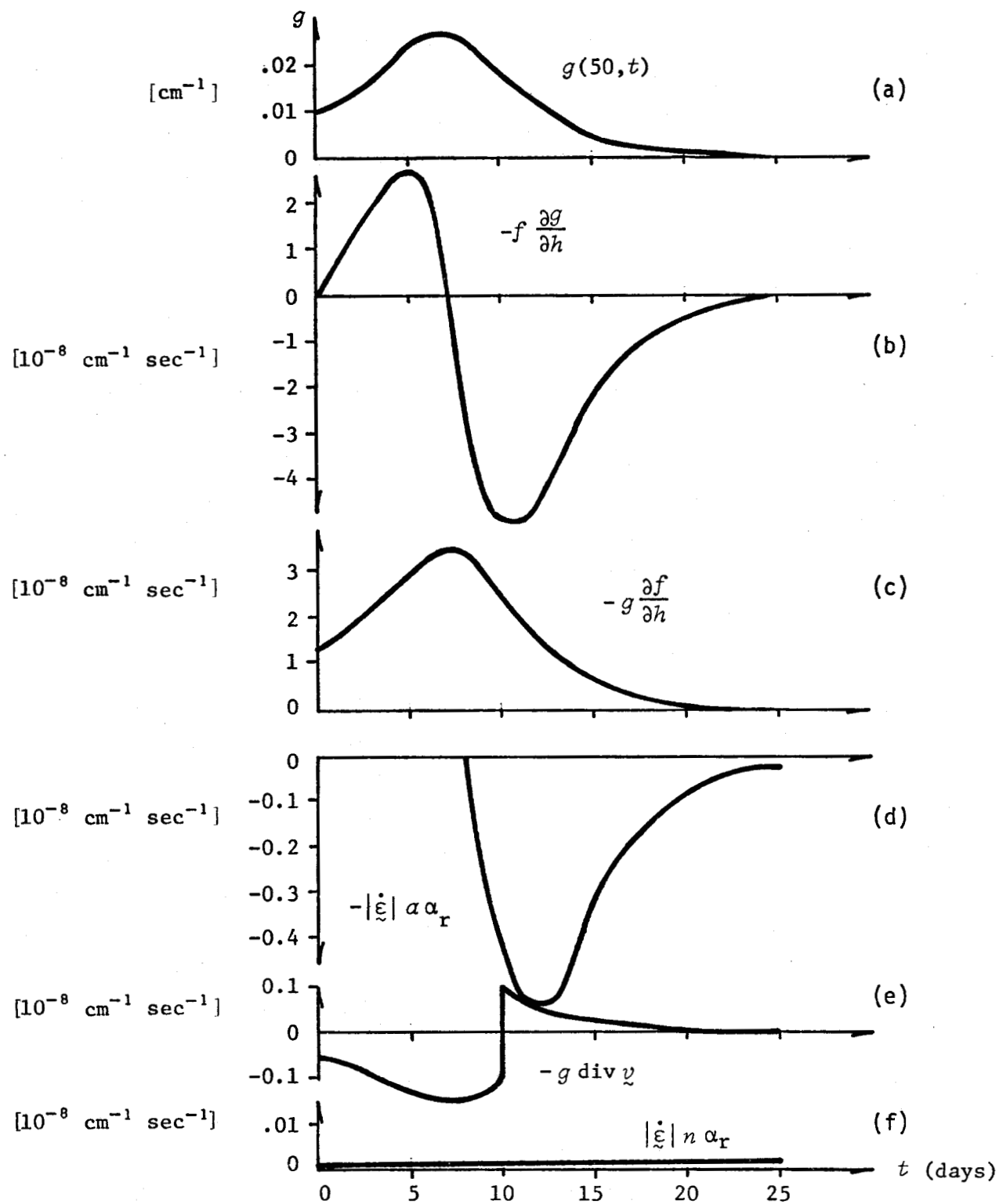


Fig. 5.18. Terms contributing to changes in the amount of ice at 50 cm thickness during uniaxial deformation--extension for 10 days followed by compression.

Taking a section at $h = 50$ cm of the surface contoured in Figure 5.19, we see that $g(50, t)$ first increases to a maximum at about 7 days and then decreases, leveling off to a constant value at about 17 days. Since many processes are acting at once here, we will identify, using Figures 5.18b through 5.18f, the terms in the g -equation responsible for the observed behavior.

5.4.1 $0 < t < 7$ days

For $0 < t < 7$ days the thermodynamic terms dominate. The "thermodynamic wave crest" advances from the origin in (h, t) space, following a characteristic, and reaching 50 cm at $t \approx 7$ days. Since $h = 50$ is to the right of the wave crest until $t = 7$, $\partial g / \partial h$ is negative. The term $(\partial f / \partial h)_{h=50}$ is always negative and $f(50)$ and $g(50)$ are always positive, so that both thermodynamic terms $\left(-f \frac{\partial g}{\partial h}\right)_{h=50}$ and $\left(-g \frac{\partial f}{\partial h}\right)_{h=50}$ are positive. Consequently, $g(50)$ increases as the wave crest advances.

The dynamic terms are much smaller. Since $\text{div } \vec{v} > 0$ (until $t = 10$ days), some ice of all thicknesses is being exported from the region (Fig. 5.18e). At the same time, a certain amount of ice is being ridged ($\alpha_r = 0.15$), and we must ask how the redistribution process affects g at $h = 50$. Figure 5.20 shows the regions of the solution space which are supplying and being supplied by the ridging process. Because h^* has been less than 50 cm, no 50 cm ice has been going into ridges. However, throughout this period h^* has been greater than 10 cm, so that some 50 cm ice has been produced from 10 cm ice by ridging. Therefore, $\alpha(50)$ is zero and $n(50)$, though exceedingly small by comparison with other terms, is positive. There are two reasons that $n(50)$ is so small. The first is that $g(10)$ becomes very small after the first several time steps, so that not much 10 cm ice is available. Furthermore, the five-fold ridging law used here produces only 1/5 of an area of 50 cm ice for every unit area of 10 cm ice. An area of ice A, in the thickness band (10, 11 cm), say, will produce an area $A/5$ in the band (50, 55 cm). Since g measures the area per unit thickness, the additional area of ice in the band (50, 51 cm) is only $A/25$. Symbolically,

$$N(h) = \frac{1}{5} A(h/5) \Rightarrow n(h) = \frac{1}{25} \alpha(h/5).$$

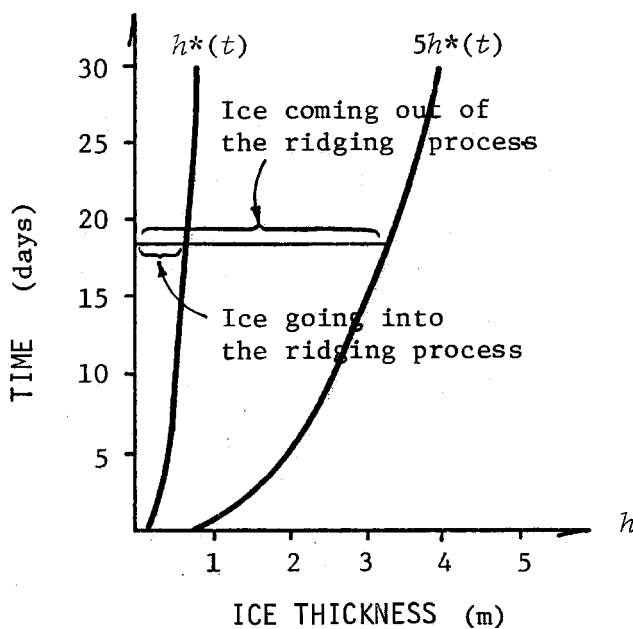
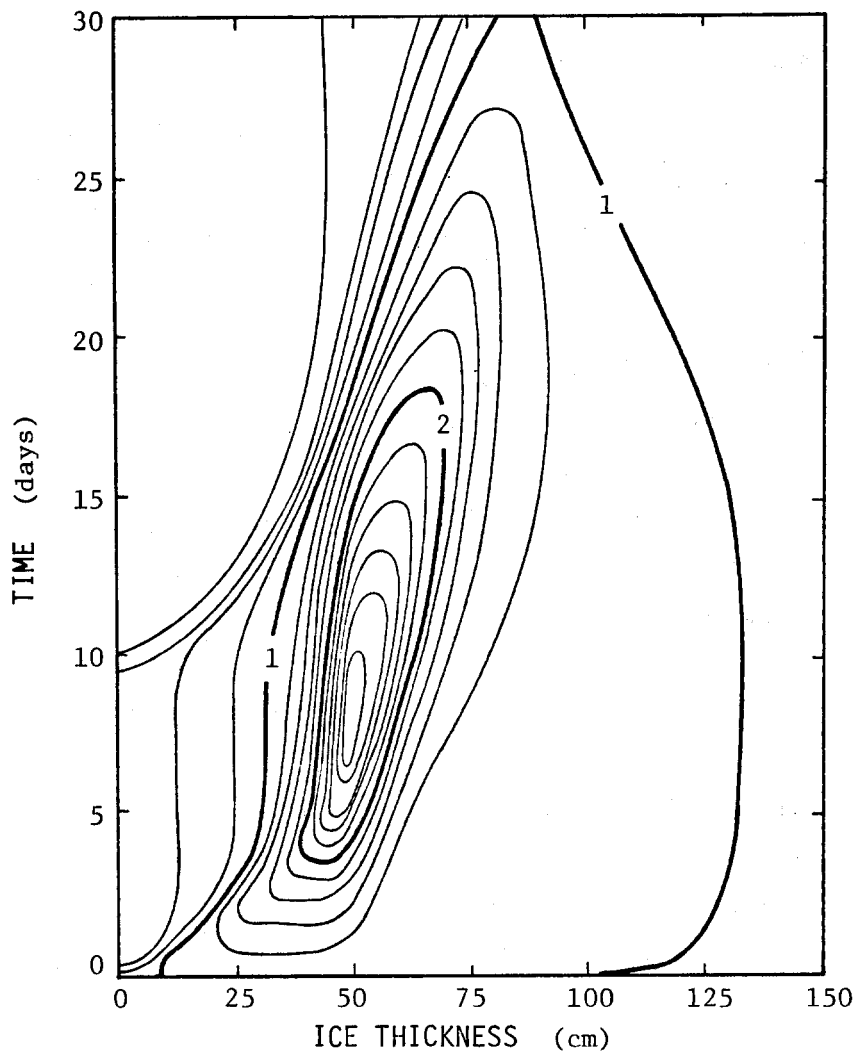


Fig. 5.20. The regions in (h, t) space participating in the ridging process.

5.4.2 $7 < t < 8$ days

For $t > 7$ days, the thermodynamic wave crest has passed and $\partial g / \partial h$ and, therefore, $-f(\partial g / \partial h)$ change sign (Fig. 5.18b). By $t \approx 8$ days, this term has grown large enough to cause $g(50, t)$ to begin to decrease.

5.4.3 $8 < t < 10$ days

Coincidentally, it is also at $t \approx 8$ days that h^* has increased past 50 cm (Fig. 5.20). At this time 50 cm ice begins to be consumed in ridging. Since there is at this time a high concentration of ice at 50 cm, i.e., a maximum in $g(h)$, the area of 50 cm ice going into ridging, $\alpha(50)$, soon becomes large. This is seen by examining the construction of $\alpha(h)$:

$$\alpha(h) = \frac{\partial}{\partial h} A(h) = \frac{\partial}{\partial h} B(G(h)) = \frac{\partial B}{\partial G} \frac{\partial G}{\partial h} = \left(\frac{\partial B}{\partial G} \right)_{h=50} g(50)$$

When $G(50) = G^* = 0.15$, i.e., $h^* = 50$ cm, then $(\partial B / \partial G) = 0$. But as soon as $h^* > 50$, $(\partial B / \partial G)_{h=50}$ becomes large; and since $g(50)$ is large, $\alpha(50)$ also becomes large. $-\alpha(50)$ is drawn in Figure 5.18d to emphasize that this process represents the rate at which 50 cm ice is taken away to be used in ridging.

5.4.4 $t > 10$ days

At $t = 10$ days, the motion changes to uniaxial compression. The $-g \operatorname{div} \vec{v}$ term changes sign, and the ridging multiplier α_r jumps from 0.15 to 0.85. From this time on, the balance is negative and $g(50)$ decreases. The figures (5.18) illustrate that all the terms are scaled by the local value of g --except for $n(50)$, which is scaled by $g(10)$.

Nothing has been said about the opening mode here. It has been active; during extension $\alpha_0 = 0.85$, and during compression $\alpha_0 = 0.15$, but the effect of the opening at $h = 50$ cm is not manifested through a redistribution term. The opening mode of the redistributor is in fact an impulse at $h = 0$. The effect of the opening is felt at $h = 50$ cm in the following way. The opening at $h = 0$ and the immediate action of $f(0)$ create thin ice which,

under the continued action of f , reaches 50 cm in about 7 days. Thus the value of $g(50)$ and the slope $(\partial g / \partial h)_{h=50}$ reflect an episode of opening only after a time lag of about a week.

A steady value is reached at $t = 17$ days, because by this time the characteristic passing through $(h=0, t=10)$ --the motion changed sign at $t = 10$ days--has reached 50 cm. Thereafter, the value of $g(50)$ is constant (Fig. 5.19).

5.5 The Case of Pure Shear

The ice thickness distribution changes in shear with equal ridging and opening:

$$\alpha_r = \alpha_o = 0.5.$$

The $\operatorname{div} \mathcal{V}$ term vanishes, of course, for a pure shear motion. A contour plot of g is given in Figure 5.21. Qualitatively, the case is similar to that of uniaxial deformation. Quantitative differences arise because α_r and α_o are different.

During pure shear deformations, the stress state is uniaxial (Fig. 5.22), so that one principal value of stress is always zero. The other takes the value of p^* . The yield strength p^* for the three initial conditions is given in Figure 5.23. The three curves tend to a constant value for p^* that will be reached when the thinnest 15% of the ice is all new ice produced by the opening mode. The two curves that harden produce no unusual results. The response is qualitatively reasonable and not unlike the isotropic response. However, in the case where all ice was initially distributed between 1 and 2 meters (initial condition 3), the opening mode produces enough thin ice to cause the yield strength to drop. This case exhibits a so-called unstable behavior: a shear strain induces a decreasing shear stress, shown in Figure 5.24. This unstable response is to be expected as a result of the model whenever a decreasing yield strength occurs (except when the stress state is zero). The capacity of the ice to continue to deform as the loads are reduced disqualifies it as a Drucker material (see section 3.6).

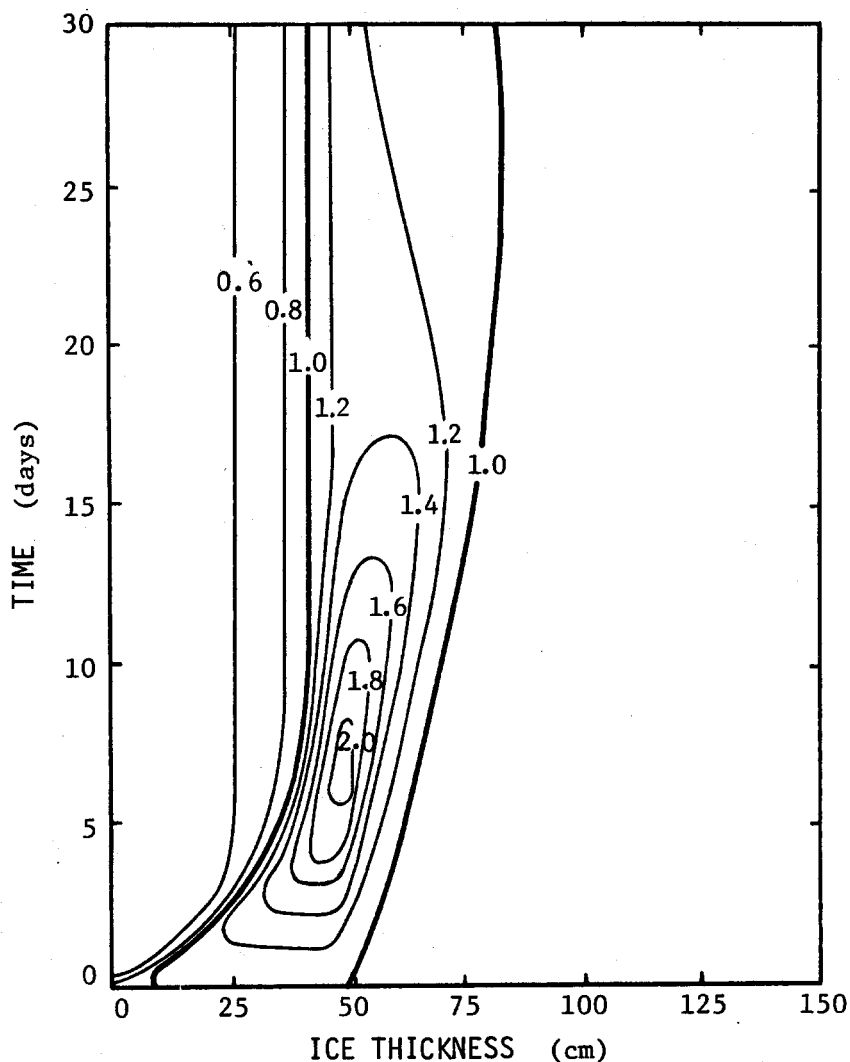


Fig. 5.21. Contours of thickness distribution $g(h, t)$ in units of 10^{-3} cm^{-1} under influence of thermodynamics and pure shear deformations. Results are for initial condition 1 (Table 5.2).

Fig. 5.22. Normalized yield curve during a pure shear deformation. The positions 1 and 2 are the stress state on the normalized yield curve for the pure shear case.

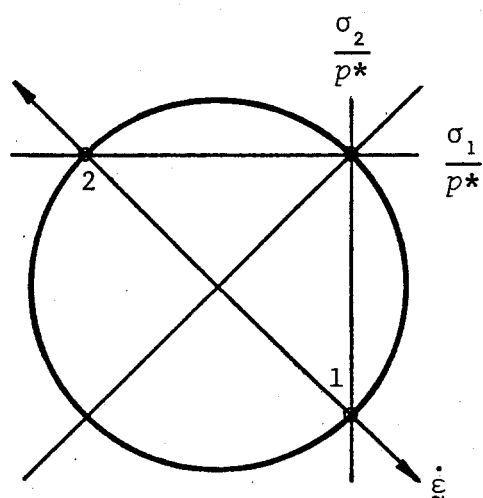


Fig. 5.23. The behavior of the yield strength in pure shear for the three initial conditions.

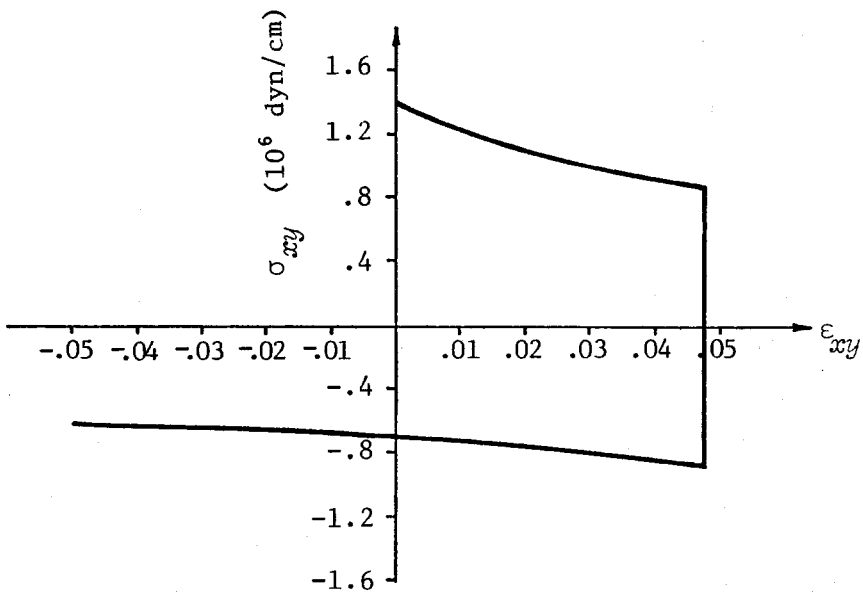
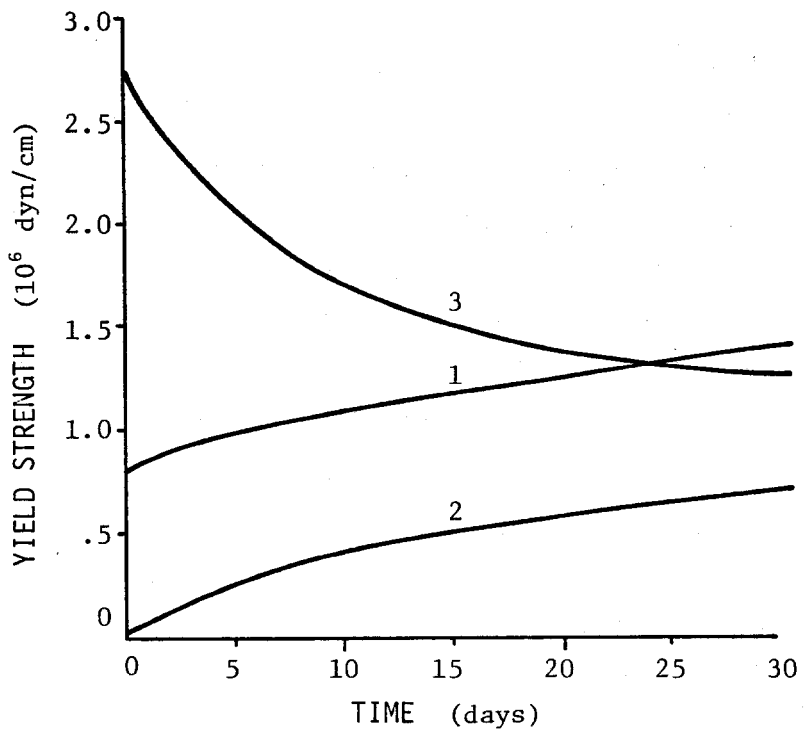


Fig. 5.24. The stress strain path for pure shear strain with initial condition 3. After 10 days the direction of straining is reversed to show the elastic jump across the yield curve followed by continued deformation.

5.6 1972 AIDJEX Pilot Study Data

Real strain rate data from the 1972 AIDJEX pilot study were used to drive the constrained motion calculations. We believe that the thermodynamic function being used is valid, and this leaves the initial thickness distribution as the only missing input to the calculations. For comparison with the other calculations, we have run these data, as in the previous cases, using each of the three initial conditions of Table 5.2; of the three, we believe that the first comes closest to representing the actual distribution.

The strain history has been taken from Thorndike [1974], plots of which are included here as Figure 5.25. The most striking event is the divergence of about 5% which occurs early in the record (16-19 March). Although part of the dilatation was recovered, the trend throughout the 40 days of observations was weakly divergent. The plots of the principal values of the strain rate tensor, not reproduced here, imply that the principal values almost never have the same sign. Thus, their sum rarely exceeds their difference, which is to say, in terms of the invariants defined in section 2.3.2, that $\pi/4 < \theta < 3\pi/4$. Shearing is favored, it appears, in the motion of pack ice.

The thickness distribution history during the experiment is presented in Figure 5.26. The p^* histories are plotted in Figure 5.27. By the end of the record, the initial disparities between the three p^* curves have almost disappeared. This can be attributed to the initial divergence, the generally divergent trend, and the tendency of the ice to deform in shear rather than in isotropic compression or extension. Curves for initial conditions 2 and 3 tend to bracket the curve for the most realistic initial condition 1. Since the true initial condition was close to condition 1 and since these curves imply that after 10 or 20 days p^* is insensitive to the initial condition, we place some confidence in the calculated values of p^* toward the end of the record. Even if we had known the initial condition exactly, the response, in p^* , would have been about the same. The magnitude of p^* is 10^6 dyn cm $^{-1}$.

The stress components (Fig. 5.28) are found by determining the point on the yield curve whose outward normal is in the direction of the strain

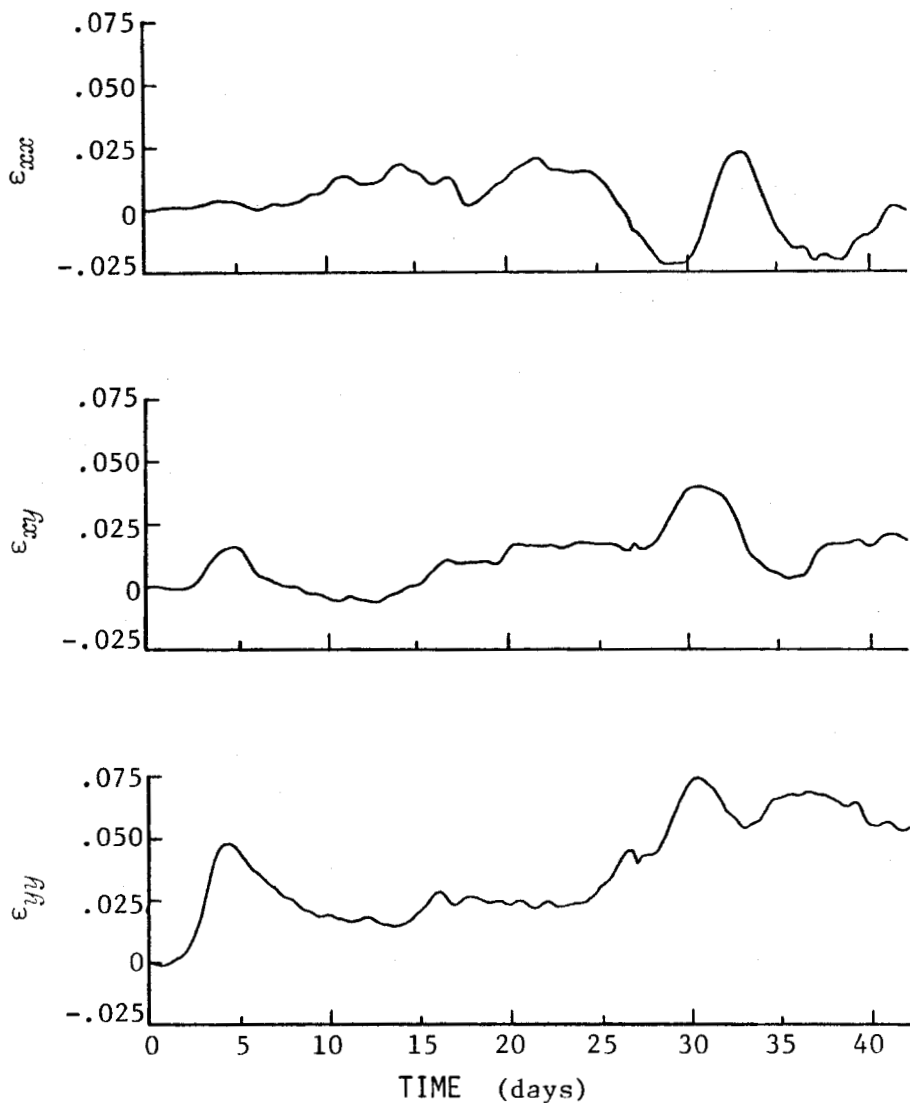


Fig. 5.25. Strain rate components from the 1972 AIDJEX large-scale strain measurements. Time is measured from 0000 GMT, 14 March 1972.

rate. Therefore, σ_{ij} is a function of $\dot{\epsilon}_{ij}$ and is proportional to the yield strength. Thus σ_{ij}/p^* depends only on the given strain rates and not on the initial conditions. The stresses will vary both because p^* changes in time and because the strain rates change. From these results it appears that p^* varies slowly compared to the strain rate. On seasonal time scales, and over distances of 1000 km, we may find that the variations in p^* become more important than the high frequency strain rate fluctuations.

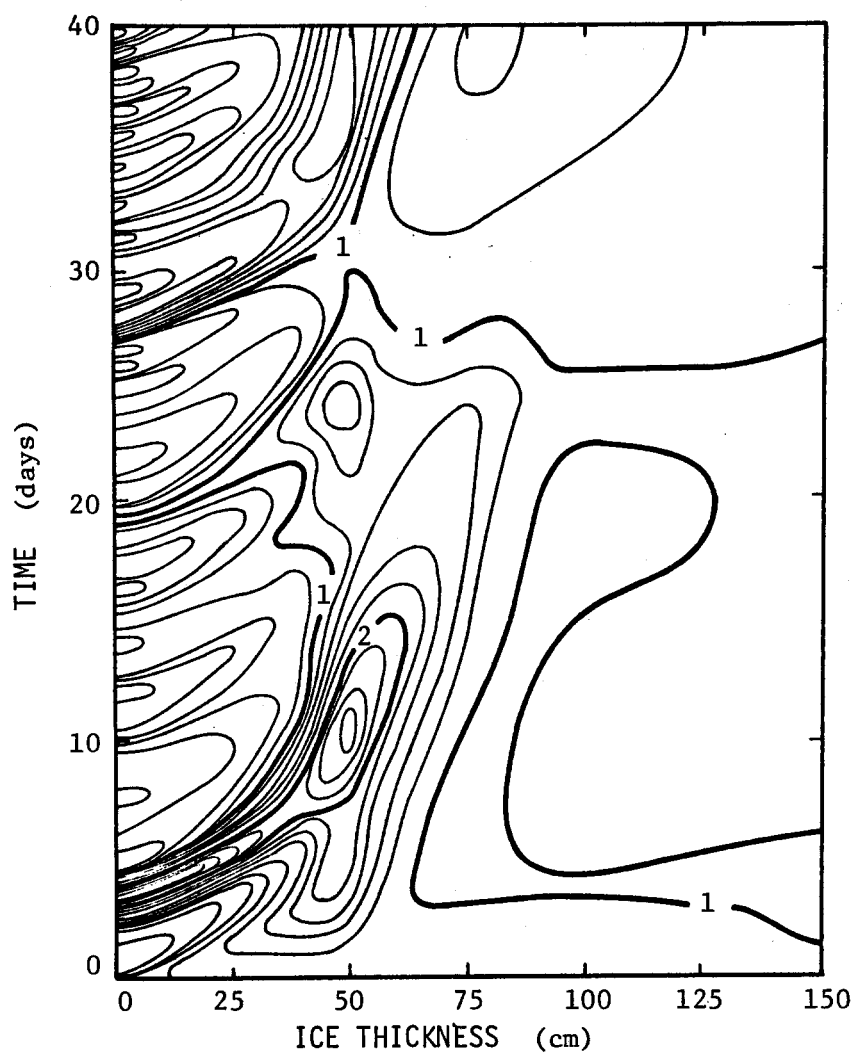


Fig. 5.26. Contours of thickness distribution $g(h, t)$ in units of 10^{-3} cm^{-1} during the 1972 AIDJEX pilot study. Results are for initial condition 1 (Table 5.2).

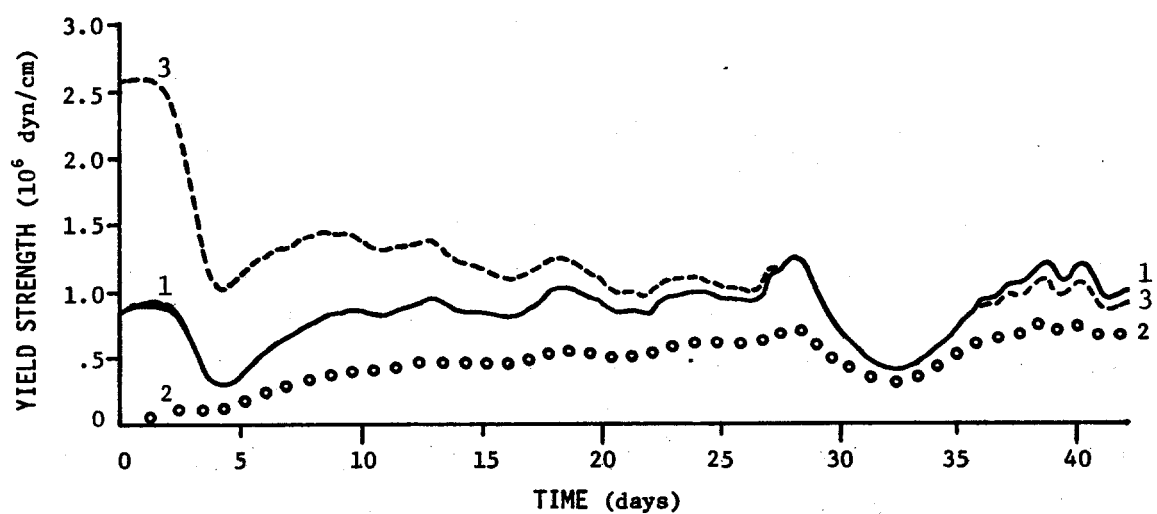


Fig. 5.27. The behavior of the yield strength p^* for the 1972 AIDJEX pilot study data, using three different initial conditions.

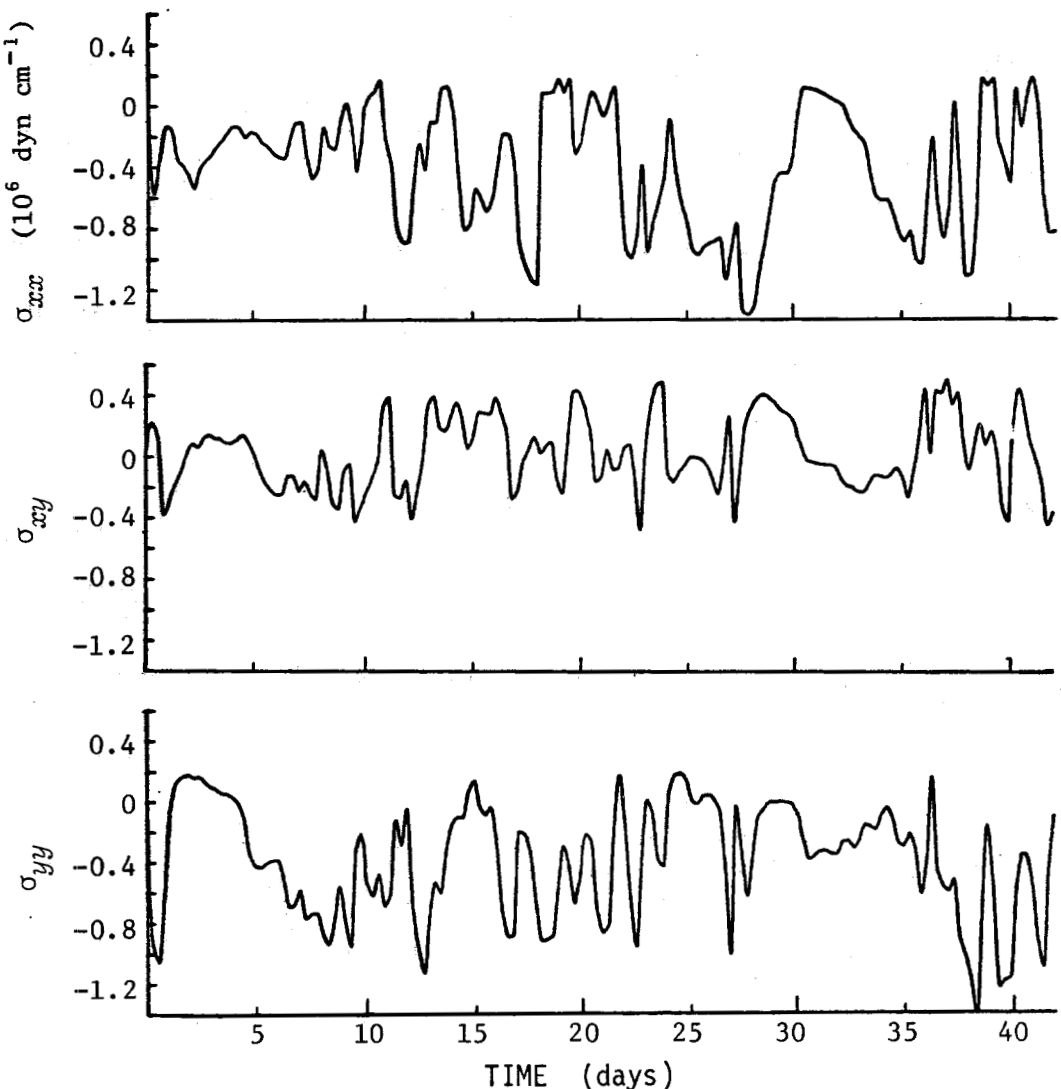


Fig. 5.28. The behavior of stress components for the 1972 AIDJEX pilot study data using initial condition number 1 (Table 5.2).

In this discussion, we have not mentioned the elastic behavior of the ice. For the time step used here ($\Delta t = 6 \text{ hr}$) and for the values used for the elastic moduli ($M_1 = 10^7 \text{ h}$ and $M_2 = 0.5 \cdot 10^7 \text{ h}$), the material is almost always plastic. In future work we will clarify the role of the elastic response.

Is the magnitude of p^* found here ($\sim 10^6 \text{ dyn cm}^{-1}$) compatible with what we know of the wind-driven movement of pack ice? To ask how readily plastic flow might occur, we consider a stationary slab of pack ice. We

ask over what length L a typical wind stress $\tau = 0.1 \text{ dyn cm}^{-2}$ must act in order to cause plastic deformation (Fig. 5.29). Assuming a yield stress of 10^6 dyn cm^{-1} we conclude that $L = 100 \text{ km}$. Had p^* been an order of magnitude higher ($p^* = 10^7 \text{ dyn cm}^{-1}$), a fetch of 1000 km would have been required. This would have been unacceptable, in that 1000 km is nearly the width of the Arctic Basin and so plastic flow would seldom occur. This example gives some meaning to the computed yield strength of $p^* = 10^6 \text{ dyn cm}^{-1}$.

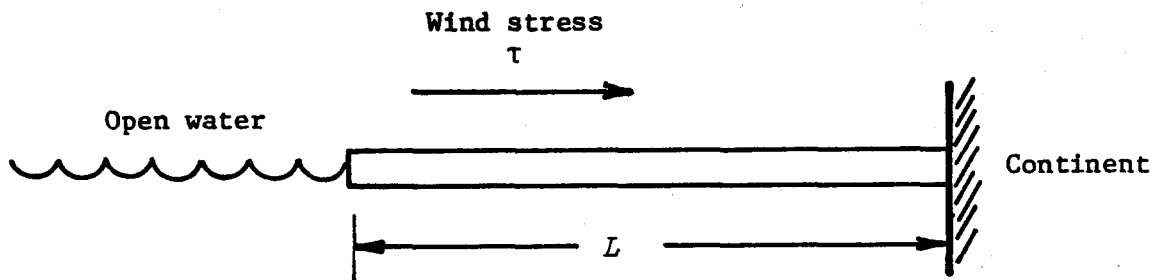


Fig. 5.29. A wind stress $\tau = 10^{-1} \text{ dyn cm}^{-2}$ acting over a fetch of ice $L = 100 \text{ km}$, produces a stress $\sigma = L\tau$ equal to the compressive yield strength of the ice $p^* = 10^6 \text{ dyn cm}^{-1}$.

6. DISCUSSION

6.1 Summary

A continuum model for the mechanical behavior of sea ice has been formulated in which the ice is viewed as a two-dimensional body with thickness included, not as a third dimension, but as a property of the material dependent on the other two coordinates. The ice is viewed as a mixture of many constituents defined only by their thickness. The thickness distribution provides a measure of the amount of each constituent in a region. The following phenomena are parameterized in the model:

1. Ice changes its thickness as it grows or melts.
2. Diverging motion acts as a source of open water.
3. Converging motion ridges thin ice into thick ice.

The mechanical response of sea ice is treated as that of an elastic-plastic material. The yield curve depends on the yield strength, p^* , determined by the thickness distribution (see eq. 4.2). During plastic flow, the strain rate vector (defined in section 2.3.2) is normal to the yield curve (see eq. 3.16). Elastic response is isotropic, and it depends on the average thickness of the ice (see eq. 3.13). Since the elastic moduli are large and the elastic strain rates are small compared to the plastic strain rates, the material approximates a rigid plastic. The elastic response must be included to solve the system of equations.

The material response is studied by driving both the mechanical constitutive equations and the thickness distribution model with a prescribed strain rate history. These construed motion studies have helped to determine how the model material behaves and how sensitive it is to material properties and initial conditions.

In this report we have discussed simple construed motions which illustrate the response of the model, and we have concluded that the model responds roughly the way we believe the ice would respond. It would be misleading to imply that the model has told us how the ice behaves; rather, we have designed the model to include what we believe to be the

important behavior of the ice. In general, many processes are acting at once--some of the ice is melting, some is freezing, and some is being ridged at the same time that open water is being formed--with opposing effects on the strength of the pack ice. It is not possible usually to make specific statements about how the ice behaves without examining the numerical values of the terms in the basic equations.

6.2 Conclusions

The yield strength of the sea ice mixture depends on the thickness of the thinnest G^* of the ice. If $G(h = 0^+) > G^*$, the ice has no strength. Thus G^* is the minimum area of open water that must be present for the ice to be incapable of resisting any load. Observations of the motion of a loose summer ice pack may help resolve this number. In any case, our nominal value $G^* = 0.15$ can't be too bad. The yield strength p^* , for a situation when 15% of the ice is uniformly distributed up to 150 cm, is $8 \cdot 10^5 \text{ dyn cm}^{-1}$.

The yield strength p^* is constructed upon potential energy arguments and an assumption that ice of thickness h changes into ice of thickness $5h$ during ridging. The densities of ice and water and the acceleration of gravity appear explicitly in the expression for p^* . The dependence of p^* on elastic moduli or the tensile strength or other mechanical properties of sea ice is implicit in the assumed form of the redistribution function.

Fluctuations in the stress state of the ice depend on fluctuations in either the strain rate state or the yield strength. Although p^* appears to vary slowly compared to the strain rate, the p^* fluctuations may become the dominant effect on a seasonal time scale.

Because our material can soften, quite plausible situations exist which do not satisfy Drucker's postulate. This can happen even during isotropic compression if the effect of melting overrides the mechanical effects. The other consequences of Drucker's postulate, such as the normality of strain rate vector to the yield curve and the convexity of the yield curve, have been used here, but these may be incorrect.

We can be certain that the ice will soften during isotropic divergence under the influence of summer thermodynamics. For any other condition, however, we cannot predict, without looking to the ice thickness distribution, whether the ice will harden or soften.

The 1972 strain data show that the ice usually deforms with principal values of opposite signs, so that the shear invariant exceeds the divergence invariant ($\pi/4 < \theta < 3\pi/4$), and we expect to find significant ridging and opening occurring together rather than alternately. Real variations in p^* will be less dramatic than in the cases of isotropic motion discussed in this report.

In actual calculations, the strength, p^* , depends on the initial conditions. However, as time goes on the characteristic originating at ($h=0$, $t=0$) partitions the solution space (h,t) into two regions, one that depends on the initial conditions and one that does not. When h^* is to the left of the (0,0) characteristic, p^* does not depend on the initial conditions. Because we are unlikely ever to have good field measurements to determine an initial thickness distribution, it is important to know how long we must run a calculation before p^* forgets the initial state. No absolute statement can be made, since the (0,0) characteristic can never exceed 500 cm and a sufficiently large convergence could push h^* over that value. But as a rough statement, divergence tends to move h^* to the left, and winter growth rates move the (0,0) characteristic most rapidly to the right; both effects tend to wipe out the influence of the initial condition on p^* . In the case of the 1972 data, perhaps typical of spring conditions in the Beaufort Sea, the effects of the extreme initial conditions 2 and 3 (section 5.5) were greatly suppressed after about twenty days.

For the cases shown in this report, the results are essentially independent of values of elastic moduli because the material is almost always plastic. Thus, any increase in the values of M_1 and M_2 would not alter the output. Since the moduli were chosen at the lower limits of expected values, no errors are believed to be introduced by our choice of values.

6.3 Recommendations

We believe we have identified the important physical processes at work and shown how they interact. But the description of each process is only tentative. More work is needed.

1. The growth rates for very thin and for very thick ice should receive more observational and theoretical attention. For real model calculations, measured growth rates or growth rates deduced from measured air temperatures should be used instead of the climatological mean values given in Table 4.3.

2. Studies will be needed to determine the sensitivity of the model to the form of the redistribution function, to the shape of the yield curve, to the assumed flow rule, and to the elastic moduli, so that future efforts may be directed at components to which the model is most sensitive.

3. Elastic strain rates should be included when the material is plastic.

4. The mathematical properties of the complete system of equations must be explored.

5. Attention should be given to the presence of voids in newly formed ridges. They affect the potential energy and therefore p^* ; and the freezing of water in these voids provides an additional mass source. More observations of these phenomena are needed.

6. The energy sinks that we have neglected--both in ridge formation and in shearing between floes--need more careful assessment. Very little is known about the fracture toughness and large-scale frictional properties of sea ice.

Future work will include further construed motion studies and also actual one- and two-dimensional dynamic calculations with real driving forces. The one-dimensional dynamic calculations will be used primarily to determine the effects of various parameters on the response. The two-dimensional dynamic calculations are, of course, the real reason for developing the model.

The first and only foreseeable test of the model discussed here will be possible in 1975-76 when real data from the main AIDJEX field experiment become available.

ACKNOWLEDGMENT

We would like to acknowledge the help of all our colleagues at AIDJEX, with special thanks to Norbert Untersteiner, the AIDJEX Coordinator; to R. J. Evans, J. F. Nye, and R. R. Parmeter for their comments and criticism during the conceptual development of the model; to R. Colony for the solution technique and programming of the thickness distribution model; and to B. Mukherji for developing the data display capability and helping to obtain plots.

Many people have participated in the preparation of this document. We recognize and appreciate the support of the entire AIDJEX staff, particularly the efforts of A. Johnson, J. Fitzgerald, C. Barnard, N. Fukuyama, and C. Plank, without whose help this document would never have appeared.

The work was supported by the National Science Foundation Grant GV-28807 to the University of Washington for support of the Arctic Sea Ice Study and by the Office of Naval Research, Arctic Program, Contract N00014-67-A-0103-0007.

APPENDIX A

NUMERICAL SOLUTION OF THE ICE THICKNESS DISTRIBUTION EQUATION

When the thermodynamic and dynamic forcing have been specified and given an initial condition $G(h, t = 0)$, the ice thickness equation can be solved for $G(h, t)$.

A mesh of points (HM_j, t_i) in (h, t) space is established at which it is desired to compute the value of $G = G(HM_j, t_i) = GM_j^i$ ($i=1, \dots, N$ and $j=1, \dots, M$). The integration proceeds in time, advancing from values GM_j^{i-1} , $j=1, \dots, M$ to GM_j^i , $j=1, \dots, M$. In the integration scheme, certain quantities are treated as functions which can be evaluated for any value of their arguments as

$$f = f(h, t), \quad \Psi = \Psi(h), \quad W_r = W_r(h), \quad \varepsilon_I = \varepsilon_I(t) = \operatorname{div} v(t)$$

$$\varepsilon_{II} = \varepsilon_{II}(t), \quad \alpha_o = \alpha_o(\varepsilon_I, \varepsilon_{II}), \quad \alpha_r = \alpha_r(\varepsilon_I, \varepsilon_{II}), \quad B = B(G).$$

These functions are constructed either by analysis or by supplying a table of values and interpolating. The only subtlety perhaps is in defining W_r , since, by equation 4.21,

$$W_r(h) = \frac{-B(G(h)) + 1/k A(G(h/k))}{1 - 1/k}.$$

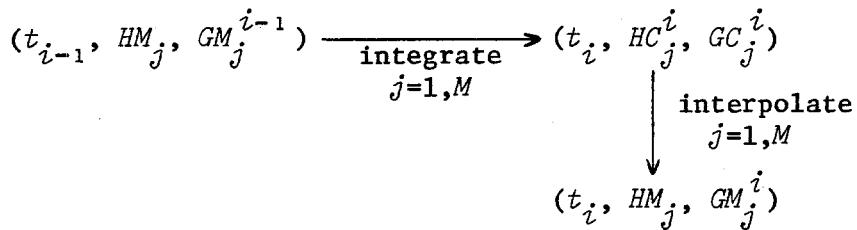
G is evaluated only at discrete values of h and may not, in general, be available at both h and h/k . In this case, a linear interpolation is done between the values of G at the h mesh points using values from the most recent time point.

The ice thickness distribution can be viewed as a pair of simultaneous ordinary differential equations

$$\frac{dh}{dt} = f(h, t) \quad \text{and} \quad \frac{DG(h, t)}{Dt} = \Psi(h) - G(h, t) \operatorname{div} v(t).$$

The first equation defines characteristics in the h, t plane and the second determines the changes in G following any characteristic. The numerical

approach taken here integrates these two equations simultaneously using a fourth-order Runge Kutta scheme (see for example Hildebrand, 1948). Thus starting at some point $(t_{i-1}, HM_j, GM_j^{i-1})$, the pair of equations tell us how HM_j will change and how GM_j^{i-1} will change. Since the new values of h will no longer correspond with the mesh points HM_j , an interpolation is done to get values of G at the mesh points:



To improve the interpolation accuracy, especially near $h = 0$, additional characteristics can be supplied starting from points on the t axis. These points simply enlarge the HC and GC arrays.

The integration of the equation can proceed in either direction along a characteristic, provided some value of G on that characteristic is specified. This applies to characteristics which cross the time axis, just as it does to characteristics crossing the h axis. Seeking solutions to a rectangular region in (h,t) space, we take the following as initial and boundary conditions:

1. $G(h,0)$ is some prescribed initial condition which must be monotonic, but not necessarily smooth.
2. $G(h_{\max}, t) = 1$ for all t . Note that h_{\max} is prescribed, but is not necessarily the smallest h such that $G(h,t) = 1$.
3. $G(0^+, t) = \begin{cases} 0, & f(0^+, t) > 0, \\ \text{unspecified}, & f(0^+, t) \leq 0. \end{cases}$

The last condition requires some comment. For $f(0^+, t) > 0$, there can be no open water. If, during divergence, open water is created, it is instantaneously acted upon by the thermodynamics to create very thin ice. Therefore, G is continuous at zero and $g(0^+, t) = 0$. However, when $f(0, t) \leq 0$, values on the characteristics crossing the $h = 0^+$ boundary (see Figure 2.4) have been specified previously, and it would overdetermine the problem to specify them again.

APPENDIX B

SOLUTION TECHNIQUE FOR MECHANICAL CONSTITUTIVE EQUATIONS

Here, we present a method for computing the stress from the elastic-plastic constitutive equations (3.5, 3.6, and 3.16), given p^* and the strain rate. Although the strain rate is specified a priori, we must determine, as part of the solution, whether the strain rate is elastic or plastic. The method applies both to a rigid plastic model and to our case, in which elastic strain rates are neglected when plastic flow occurs. The method can be used regardless of the assumed shape of the yield curve.

If the material can remain elastic without violating the yield constraint, the time derivative of equation 3.6 gives

$$\dot{I} = 2M_1 \dot{\epsilon}_{ii}$$

where I is σ_{ii} and equals twice the invariant σ_I defined in section 3. We also obtain

$$\dot{\sigma}'_{ij} = 2M_2 \dot{\epsilon}'_{ij}$$

where the prime denotes the deviator. Terms in M_1 and M_2 have been ignored.

We use the second stress invariant II' , which is defined as $\sigma'_{ij}\sigma'_{ji}$ and equals $2\sigma_{II}^2$. The yield constraint can be written in terms of p^* and the invariants I and II' . If the elastic stress state violates the yield constraint, we solve the plastic equations

$$\dot{\epsilon}_{ij} = 2\lambda \frac{\partial F}{\partial I} \quad (B.1)$$

$$\dot{\epsilon}'_{ij} = 2\lambda \frac{\partial F}{\partial II'} \sigma'_{ij} \quad (B.2)$$

$$F(I, II', p^*) = 0 \quad (B.3)$$

for σ_{ij} and λ . The most efficient procedure is to replace equation B.2 by

$$\dot{\varepsilon}'_{ij} \dot{\varepsilon}'_{ji} = \left(2\lambda \frac{\partial F}{\partial \text{II}'}\right)^2 \text{II}' \quad (\text{B.4})$$

and solve equations B.1, B.3, and B.4 for I, II', and λ . Then the stress deviator may be found from equation B.2.

The following steps allow the unknown stress to be evaluated at a set of discrete times t^n such that

$$t^n = t^{n-1} + \Delta t, \quad n = 1, 2, \dots, N.$$

We denote $\sigma_{ij}(t^n)$ by σ_{ij}^n , and $F(\text{I}^n, (\text{II}')^n, (p^*)^{n-1})$ by F^n .

1. Assume that the strain rate $\dot{\varepsilon}_{ij}^{n-\frac{1}{2}}$ is known, and that the stress state σ_{ij}^{n-1} and the strength $(p^*)^{n-1}$ are known and satisfy $F^{n-1} = 0$.

2. Compute an elastic stress estimate from

$$\text{I}^n - \text{I}^{n-1} = 2\Delta t M_1^{n-1} \dot{\varepsilon}_{ii}^{n-\frac{1}{2}}$$

$$(\sigma'_{ij})^n - (\sigma'_{ij})^{n-1} = 2\Delta t M_2^{n-1} (\dot{\varepsilon}'_{ij})^{n-\frac{1}{2}}$$

3. Compute the invariants from the elastic stress estimates and check the yield constraint. If $F^n \leq 0$, the material behavior is elastic, the elastic stress estimate is accepted as the stress state, and we omit step 4. If the estimate of F^n is positive, plastic flow must occur and we proceed with step 4.

4. For the circular yield curve used in this work, solve these equations algebraically

$$\text{I}^n = (p^*)^{n-1} \frac{(\dot{\varepsilon}_{zz})^{n-\frac{1}{2}}}{2(\dot{\varepsilon}'_{ij})(\dot{\varepsilon}'_{ji})^{n-\frac{1}{2}} + (\dot{\varepsilon}_{ii})(\dot{\varepsilon}_{jj})^{n-\frac{1}{2}}} - 1$$

$$(\text{II}')^n = (p^{*2})^{n-1} \frac{(\dot{\varepsilon}_{kl}\dot{\varepsilon}'_{lk})^{n-\frac{1}{2}}}{2(\dot{\varepsilon}'_{ij}\dot{\varepsilon}'_{ji})^{n-\frac{1}{2}} + (\dot{\varepsilon}_{ii}\dot{\varepsilon}_{jj})^{n-\frac{1}{2}}}$$

$$\lambda^n = \frac{2(\dot{\varepsilon}'_{ij}\dot{\varepsilon}'_{ji})^{n-\frac{1}{2}} + (\dot{\varepsilon}_{ii}\dot{\varepsilon}_{jj})^{n-\frac{1}{2}}}{2(p^*)^{n-1}}$$

for I^n , $(\text{II}')^n$, and λ^n . For the more general yield curves, the above values

may serve as an initial guess, with the proper solution to be obtained by using Newton's method [Isaacson and Keller, 1966]. Neither the previous stress state σ_{ij}^{n-1} nor the elastic stress estimate is a satisfactory initial guess, because the stress history may be discontinuous when plastic flow begins.

In the more general case, the equations to be solved are

$$2(\lambda)^n \left(\frac{\partial F}{\partial I} \right)^n = \dot{\varepsilon}_{ii}^{n-\frac{1}{2}}$$

$$4(\lambda^2)^n \left[\left(\frac{\partial F}{\partial II'} \right)^n \right]^2 (II')^n = (\dot{\varepsilon}'_{ij})^{n-\frac{1}{2}} (\dot{\varepsilon}'_{ji})^{n-\frac{1}{2}}$$

$$F^n = 0$$

where the notation F^n , $\left(\frac{\partial F}{\partial I} \right)^n$, $\left(\frac{\partial F}{\partial II'} \right)^n$ has been used to indicate that each depends on the stress invariants at t^n and on p^* at t^{n-1} .

Note that strain rates at $t^{n-\frac{1}{2}}$ are used to compute the stress invariants at t^n . This introduces an error of order Δt , but is necessary if a stable leap-frog difference scheme is to be found for the full field equations in section 4.1 [Richtmyer and Morton, 1967].

5. The plastic stress state is then found from eq. B.2:

$$(\sigma'_{ij})^n = (\dot{\varepsilon}'_{ij})^{n-\frac{1}{2}} / \left[2(\lambda)^n \left(\frac{\partial F}{\partial II'} \right)^n \right]$$

At this point the stress σ_{ij}^n is known. Furthermore, we now know whether $\dot{\varepsilon}_{ij}^{n-\frac{1}{2}}$ is an elastic or a plastic strain rate, and can calculate $G(h, t^n)$ and, from this, $(p^*)^n$ and $(\bar{h})^n$, and proceed to the next time step.

REFERENCES

- Anderson, D. L. 1961. Growth rate of sea ice. *Journal of Glaciology* 3: 1170-1172.
- Assur, A. 1963. Breakup of pack ice floes. In *Ice and Snow*, W. D. Kingery, ed. Cambridge, Mass.: MIT Press, pp. 335-347.
- Badgley, F. I. 1966. Heat balance at the surface of the Arctic Ocean. In *Proceedings of a Symposium on Arctic Heat Budget and Atmospheric Circulation*, The RAND Corporation, Santa Monica, California, RM-5233-NSF, pp. 267-278.
- Coon, M. D. 1972. Mechanical behavior of compacted arctic ice floes. *Offshore Technology Conference, Houston, Texas, 1-3 May 1972*. Paper No. OTC 1684. American Institute of Metallurgical, Mining and Petroleum Engineers.
- Coon, M. D., and R. S. Pritchard. 1974. Application of an elastic-plastic model of arctic pack ice. In *Proceedings of the Symposium on Beaufort Sea Coastal and Shelf Research, January 7-9, 1974, San Francisco, California*. Arctic Institute of North America. (In press.)
- Doronin, Yu. P. 1970. On a method of calculating the compactness and drift of ice floes. (K metodike rascheta splochennosti i dreifa l'dov.) *Trudy Arkt. i Antarkt. In-ta.*, 291, pp 5-17. Leningrad. [English transl., AIDJEX Bulletin No. 3 (Nov. 1970), pp. 22-39.]
- Drucker, D. C. 1950. Some implications of work hardening and ideal plasticity. *Quarterly of Applied Mathematics* 7: 411-418.
- Drucker, D. C., and W. Prager. 1952. Soil mechanics and plastic analysis on line design. *Quarterly of Applied Mathematics* 10: 157-165.
- Evans, R. J. 1970. Notes on a possible constitutive law for arctic sea ice. *AIDJEX Bulletin No. 2*, pp. 13-17.
- Evans, R. J., and N. Untersteiner. 1971. Thermal cracks in floating ice sheets. *Journal of Geophysical Research* 76: 694-703.
- Fletcher, J. O. 1965. *The Heat Budget of the Arctic Basin and Its Relation to Climate*. The RAND Corporation, Santa Monica, California, R-444-PR, 179 pp.
- Glen, J. W. 1970. Thoughts on a viscous model for sea ice. *AIDJEX Bulletin No. 2*, pp. 18-27.
- Green, K. J. 1972. A plasticity theory for porous solids. *International Journal of Mechanical Science* 14: 215-224.
- Hildebrand, F. B. 1948. *Advanced Calculus for Applications*. Englewood Cliffs, N.J.: Prentice-Hall.

Isaacson, E. and H. B. Keller. 1966. *Analysis of Numerical Methods*. New York, N.Y.: J. Wiley and Sons.

Maykut, G. A., and N. Untersteiner. 1969. *Numerical Prediction of the Thermodynamic Response of Arctic Sea Ice to Environmental Changes*. The RAND Corporation, Santa Monica, California, RM-6093-PR, 173 pp.

Maykut, G. A., and N. Untersteiner. 1971. Some results from a time-dependent, thermodynamic model of sea ice. *Journal of Geophysical Research* 76: 1550-1575.

Nelson, I., M. L. Baron, and I. Sandler. 1971. Mathematical models for geological materials for wave-propagation studies. In *Shock Waves and the Mechanical Properties of Solids*, ed. J. J. Burke and V. Weiss, Session V, Rocks and Ceramics. Syracuse, N.Y.: Syracuse University Press, pp. 289-352.

Parmerter, R. R., and M. D. Coon. 1973. Mechanical models of ridging in the arctic sea ice cover. *AIDJEX Bulletin No. 19*, pp. 59-112.

Richtmyer, R. D., and K. W. Morton. 1967. *Difference Methods for Initial-Value Problems*. New York, N.Y.: Interscience Publishers.

Rothrock, D. A. 1974a. A relation between the potential energy produced by ridging and the mechanical work required to deform pack ice. *AIDJEX Bulletin No. 23*, pp. 45-51.

Rothrock, D. A. 1974b. Redistribution functions and their yield surfaces in a plastic theory of pack ice deformation. *AIDJEX Bulletin No. 23*, pp. 53-81.

Schofield, A., and P. Wroth. 1968. *Critical State Soil Mechanics*. New York, N.Y.: McGraw-Hill.

Schwaegler, R. T. 1974. Fracture of sea ice sheets due to isostatic imbalance. In this Bulletin.

Shield, R. T. 1955. On Coulomb's law of failure in soils. *J. Mech. Phys. Sol.* 4: 10-16.

Thorndike, A. S. 1974. Strain calculations using AIDJEX 1972 position data. In this Bulletin.

Thorndike, A. S., and G. A. Maykut. 1973. On the thickness distribution of sea ice. *AIDJEX Bulletin No. 21*, pp. 31-48.

Truesdell, C., and W. Noll. 1965. The non-linear field theories of mechanics. *Encyclopedia of Physics*, vol. III/3, ed. S. Flügge. Berlin, Germany: Springer-Verlag.

Untersteiner, N. 1964. Calculations of temperature regime and heat budget of sea ice in the Central Arctic. *Journal of Geophysical Research* 69: 4755-4766.

Welch, M., E. Partch, H. Lee, and J. D. Smith. 1973. Diving report, 1972 AIDJEX Pilot Study. *AIDJEX Bulletin No. 18*, pp. 31-44.

Zubov, N. N. 1943. *Arctic Ice*. [English transl., National Technical Information Service No. AD 426972, 491 pp.]

STRAIN CALCULATIONS USING AIDJEX 1972 POSITION DATA

by

Alan S. Thorndike
Arctic Ice Dynamics Joint Experiment
University of Washington, Seattle, Washington 98105

ABSTRACT

Strain and strain rate calculations are presented based on measurements of the positions of three drifting sea ice stations. The measurements were made using the Navy Navigation Satellite System. In processing the data, time derivatives were calculated by Kalman smoothing techniques, and space derivatives by simple finite differences.

INTRODUCTION

During the AIDJEX pilot study in spring 1972, a triangular array of three drifting stations 100 km apart was deployed and manned on the Beaufort Sea pack ice. Frequent measurements of latitude and longitude at each station showed that, on a scale of 100 km, the relative positions of the camps changed by only a few percent during the 40-day observation period, from 15 March to 23 April (Fig. 1).

In the present work, we use the position measurements to estimate the bulk strain and strain rate time series of the ice within the triangular array of stations. Contemporary strain measurements on a smaller, 10 km, scale have been discussed by Hibler et al. [1973].

Throughout this report, we refer to the stations by their radio call names: Jumpsuit (JS) to the east, Brass Monkey (BM) to the north, and Blue Dog (BD) to the west.

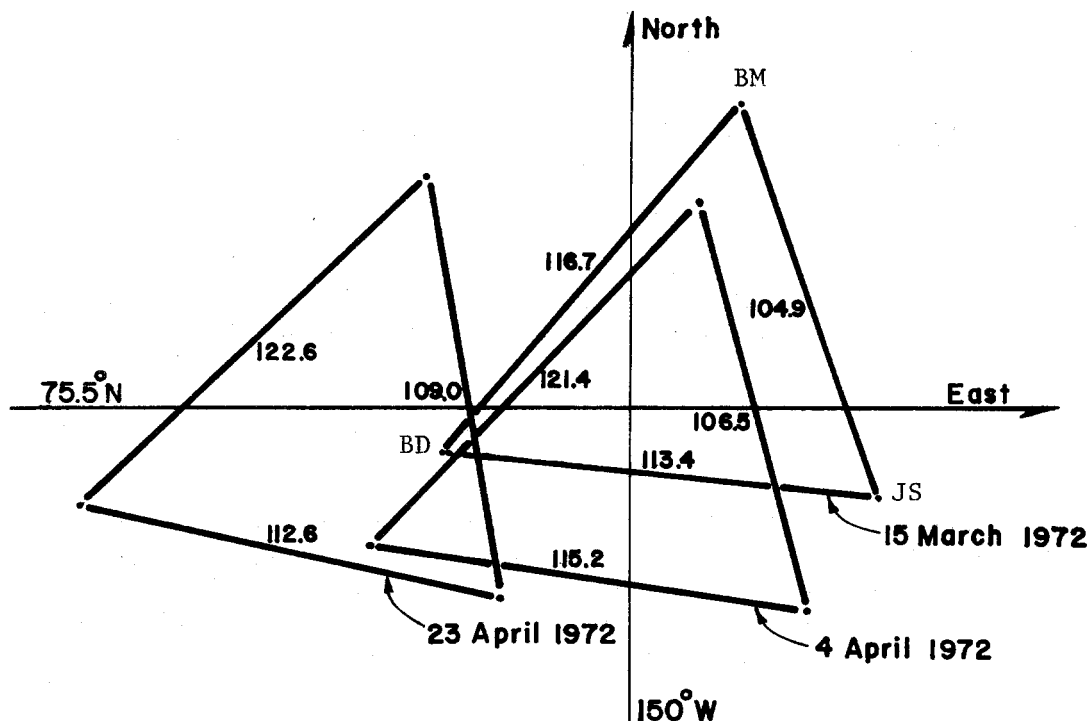


Fig. 1. The 1972 AIDJEX pilot study strain array. Distances between the stations are given in kilometers on three different days. Station Jumpsuit (JS) is at the east corner of the triangle, Brass Monkey (BM) at the north, and Blue Dog (BD) at the west.

THE MEASUREMENT SYSTEM

The Navy Navigation Satellite System (NNSS) provided the raw position measurements. With N NSS, an observer is able to determine his position from the satellite's known orbit--and thus its position at any given time--and from measurements, based on the Doppler shift principle, of the motion of the satellite relative to the observer. The fix accuracy is limited by the accuracy of the Doppler measurements, by the accuracy of the satellite's orbital parameters, and by the distortion of the satellite signal as it passes through the Earth's atmosphere.

When observers at two stations in the same region observe the same satellite during the same time interval, they should encounter similar fix errors caused by the uncertainty about the satellite's true position and by

the radio propagation errors. The errors from these sources, therefore, are correlated in space. We exploit this fact here, using NNSS in the so-called translocation mode to obtain improved measurements of the relative positions of the strain stations. To be precise, if the errors in measuring the absolute positions of points A and B have variances σ_A^2 and σ_B^2 and correlation α , then the variance of the measurement of the relative position, A - B, is $\sigma_A^2 + \sigma_B^2 - 2\alpha\sigma_A\sigma_B$. Our field calibration measurements (see Fig. 2) suggest that α is about 0.3, giving a 30% reduction of variance by using the data in a translocation sense.

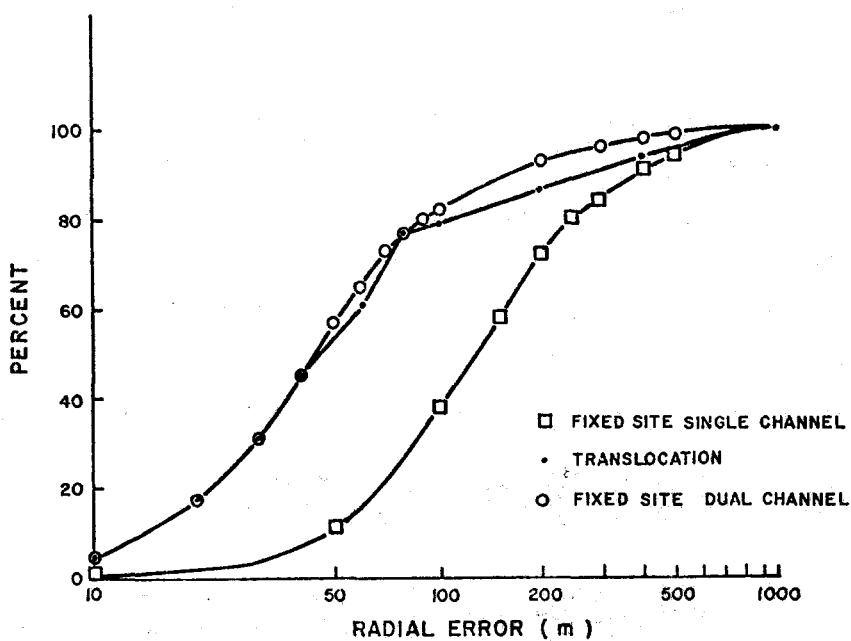


Fig. 2. Radial error distributions for two different NNSS receivers in the fixed site and translocation modes, using data collected on the north slope of Alaska in 1972.

The three sets of raw data were scanned to find pairs of stations that had acquired good data from the satellite during the same time interval. When necessary, some data were trimmed off to provide exactly matched data intervals. The matched data were used without further editing to calculate the latitudes and longitudes of the two stations and, by subtraction, the relative fix. Then the reduced variance appropriate for translocation was assigned. When, for many of the satellite passes, translocation was not possible, the standard latitude and longitude fixes were used.

Each data point takes the form $(\ell, t, x, y, \sigma_x^2, \sigma_y^2)$ where
 t is the time of the observation, taken as the time that the satellite
is closest to the observer,
 x is either a longitude or, in translocation, a difference of
longitudes,
 y is either a latitude or a difference of latitudes, and
 σ_x^2, σ_y^2 are estimates of the variance of the measurement errors in
 x and y .

The value of ℓ can vary, depending on whether it indicates a standard fix at one of the three stations or a translocation fix between a pair of stations.

A series of about 3000 data points was constructed in this way. Figure 3 shows the distribution of data points in time. The large gaps in the data series were caused by equipment failures. Following day 105, none of the data were processed in the translocation mode. Some improvement may be possible by rerunning those data, taking advantage of all translocation possibilities.



Fig. 3. The distribution of data points in time.

SMOOTHING

The sizable measurement errors and the uneven spacing of the data make straightforward processing risky. Errors of 200 m or more do occur in the data series a few times a day; this is equivalent to a strain of 0.2%, quite comparable to the strains being observed. Furthermore, it is unclear just how to estimate the distance between two stations when they receive fixes at different times. The difficulties become greater when one estimates the rate of strain, since this quantity is a second derivative of position.

The approach taken here, following earlier work to estimate the velocity and acceleration of a single ice station [Thorndike, 1973], is to smooth the data series in time using Kalman filtering techniques. The space derivatives are then calculated as simple finite differences. The decision to follow a sophisticated algorithm in time and a simple one in space was dictated by the measurements available to us. If one had more measurements in space or fewer in time, as Hibler et al. [1973] do, a different technique might be appropriate.

The filter is designed to take advantage of the translocation measurements in a natural way. The state of the three-station strain array is described by the absolute position and velocity of the first station and by the position and velocity of the other two stations relative to the first.

$$X = \text{state vector} = \begin{bmatrix} x_{JS} \\ y_{JS} \\ u_{JS} \\ v_{JS} \\ \Delta x_{BD-JS} = x_{BD} - x_{JS} \\ \Delta y_{BD-JS} = y_{BD} - y_{JS} \\ \Delta u_{BD-JS} = u_{BD} - u_{JS} \\ \Delta v_{BD-JS} = v_{BD} - v_{JS} \\ \Delta x_{BM-JS} = x_{BM} - x_{JS} \\ \Delta y_{BM-JS} = y_{BM} - y_{JS} \\ \Delta u_{BM-JS} = u_{BM} - u_{JS} \\ \Delta v_{BM-JS} = v_{BM} - v_{JS} \end{bmatrix}$$

The development of the state vector in time is modeled by

$$X_{n+1} = \Phi(n+1, n)X_n + \Gamma(n+1, n)w_n \quad (1)$$

where

$$\Phi = \begin{bmatrix} 1 & \Delta \\ 0 & 1 & \Delta \\ & 1 & 0 \\ & 1 & 0 & 0 \\ & 1 & \Delta \\ & 1 & \Delta \\ & 1 & 0 \\ & 1 & 0 \\ 0 & & 1 & \Delta \\ & & 1 & \Delta \\ & & 1 & 0 \\ & & 1 & 0 \end{bmatrix}, \Gamma = \begin{bmatrix} \Delta^2/2 & 0 & 0 \\ \Delta^2/2 & 0 & 0 \\ \Delta & 0 & 0 \\ \Delta & 0 & 0 \\ 0 & \Delta^2/2 & 0 \\ 0 & \Delta^2/2 & 0 \\ 0 & \Delta & 0 \\ 0 & \Delta & 0 \\ 0 & 0 & \Delta^2/2 \\ 0 & 0 & \Delta^2/2 \\ 0 & 0 & \Delta \\ 0 & 0 & \Delta \end{bmatrix}$$

and

$$w_n = \begin{bmatrix} w_{JS} \\ w_{BD-JS} \\ w_{BM-JS} \end{bmatrix}$$

and where Δ is the time interval between the most recent and the present fix. The fluctuations in the ice velocities are modeled by $\{w_n\}$. It is assumed that $\{w_n\}$ is zero mean Gaussian white noise. Under this assumption, and a similar one about the measurement process, the Kalman theory enables us to generate "optimal" estimates of the state vector using the available data. Although this assumption is arbitrary and crude, it is possible to select a variance for the white noise process $\{w_n\}$ which forces a qualitative agreement with observed ice motions (see Fig. 4). In fact, the Kalman theory could accommodate a more general random term, but our knowledge of the statistics of the ice motion would scarcely justify any greater sophistication.

It is known that the fluctuations in the ice velocities are correlated in space over distances comparable to the size of oceanic and atmospheric systems. If the value of the correlation coefficient for 100 km is β , then the covariance matrix for $\{w_n\}$ becomes

$$Q\delta_{mn} = \text{cov}(w_m w_n^T) = q \begin{pmatrix} 1 & (\beta - 1) & (\beta - 1) \\ (\beta - 1) & 2(1 - \beta) & (1 - \beta) \\ (\beta - 1) & (1 - \beta) & 2(1 - \beta) \end{pmatrix} \quad (2)$$

A value of $\beta = 0.6$ was representative of the velocity correlations calculated from the motions of previous drifting stations. A value of $q = 10^2 \text{ m}^2 \text{ hr}^{-4}$ has been used (Figs. 4 and 5).

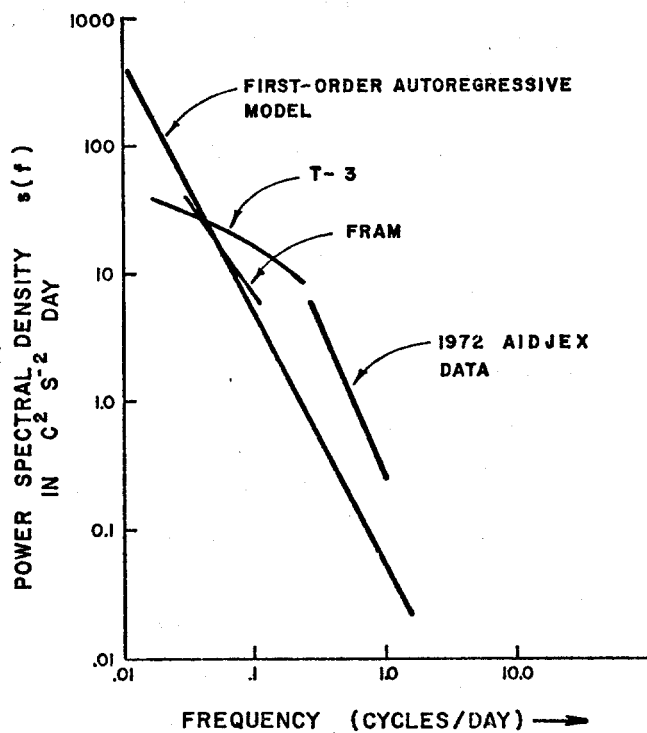


Fig. 4. A comparison of the velocity spectrum based on assumed first-order autoregressive model with spectra from several drifting stations. The driving variance for the calculations reported here was $100 \text{ m}^2 \text{ hr}^{-4}$.

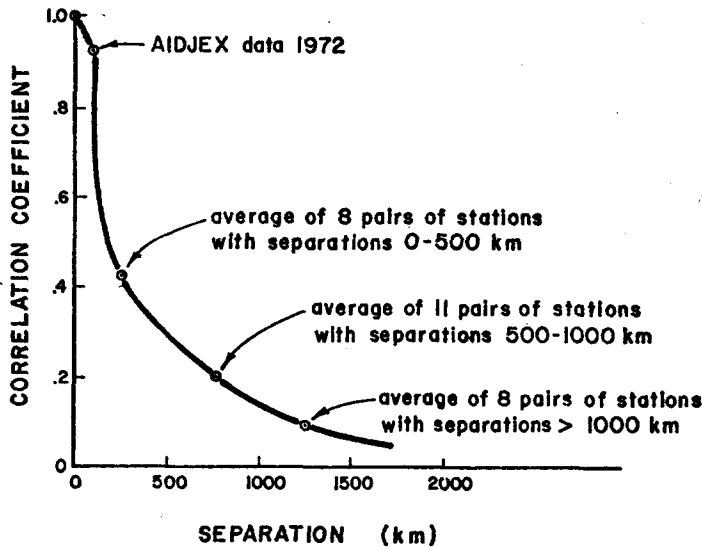


Fig. 5. The correlation coefficients for one component of the ice velocity, as a function of the separation between stations, based on calculations from drifting station data.

The measurement equation relates the measured quantity to the state vector

$$Z_{n+1} = H_\lambda X_{n+1} + v_{n+1}$$

where v_{n+1} models the measurement errors. H assumes different forms depending on the parameter λ as summarized in Table 1.

Within the structure provided by the measurement and state transition equations, Kalman filtering provides estimates of the state vector at time n , $X_{n|N}$, using the entire series of data Z_1, \dots, Z_N . Following the accepted usage in the field of digital filtering, the estimates $X_{n|N}$ are called "smoothed estimates" because they utilize past, present, and future data; that is, $N > n$. Figure 6 tends to justify this usage. The smoothing equations are available in the literature [Thorndike, 1973; Meditch, 1969].

The structure of the matrices X , Φ , Γ , and H is such that no x quantity interacts with any y quantity; this fact permits a reduction from one filter of order 12, as presented here, to two filters of order 6, as used for actual computations. The smoothing calculations used about one second of central processor time on a CDC 6400 per data point.

TABLE 1
FORMS OF H AS DETERMINED BY λ

λ	Description	H (2×12)	Typical Measurement Variance $\text{cov}(v_n v_n) [\text{m}^2]$
<i>Standard fix</i>			
1	At station JS	$\begin{bmatrix} 1 & 0 & \cdot & \cdot & \cdot \\ 0 & 1 & \cdot & \cdot & \cdot \end{bmatrix}$	50^2
2	At station BD	$\begin{bmatrix} 1 & 0 & 0 & 0 & 1 & 0 & \cdot & \cdot & \cdot \\ 0 & 1 & 0 & 0 & 0 & 1 & \cdot & \cdot & \cdot \end{bmatrix}$	100^2
3	At station BM	$\begin{bmatrix} 1 & 0 & 0 & 0 & 0 & 0 & 0 & 0 & 1 & 0 & 0 & 0 \\ 0 & 1 & 0 & 0 & 0 & 0 & 0 & 0 & 0 & 1 & 0 & 0 \end{bmatrix}$	100^2
<i>Translocation fix</i>			
4	Between BD and JS	$\begin{bmatrix} 0 & 0 & 0 & 0 & 1 & 0 & \cdot & \cdot & \cdot \\ 0 & 0 & 0 & 0 & 0 & 1 & \cdot & \cdot & \cdot \end{bmatrix}$	120^2
5	Between BM and JS	$\begin{bmatrix} \cdot & \cdot & \cdot & 1 & 0 & 0 & 0 \\ \cdot & \cdot & \cdot & 0 & 1 & 0 & 0 \end{bmatrix}$	120^2
6	Between BM and BD	$\begin{bmatrix} 0 & 0 & 0 & 0 & -1 & 0 & 0 & 0 & 1 & 0 & 0 & 0 \\ 0 & 0 & 0 & 0 & 0 & -1 & 0 & 0 & 0 & 1 & 0 & 0 \end{bmatrix}$	120^2

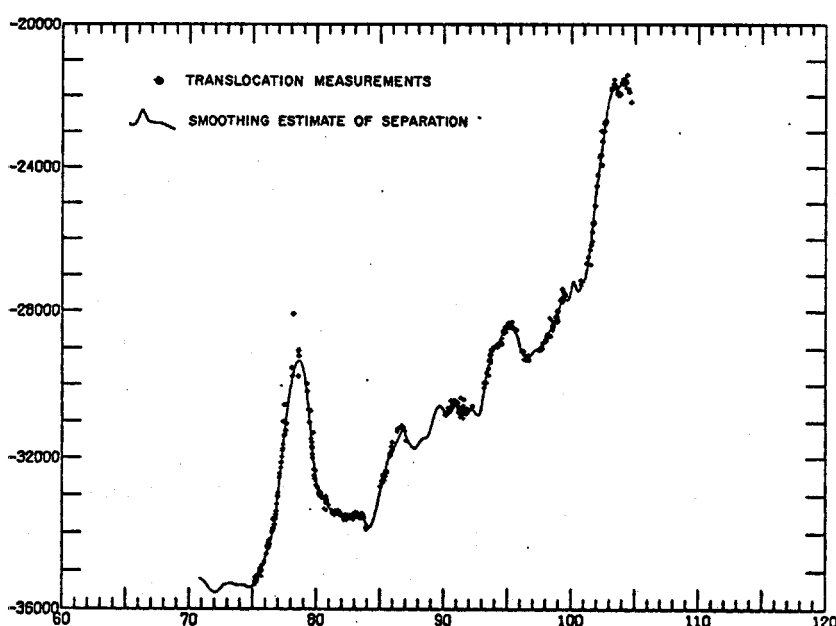


Fig. 6. Raw translocation fixes and the smoothed separation estimates, in the x direction, for ice stations Jumpsuit and Blue Dog.

STRAIN AND STRAIN RATE CALCULATIONS

The smoothing operation has produced estimates of the state vector at discrete times t_j , each estimate containing enough information to deduce strain and strain rate tensors which refer to the region defined by the triangular array. If \vec{s} is an arbitrary two-dimensional vector quantity measured at each of the three stations, we may write

$$\begin{aligned}\vec{s}_{BD} - \vec{s}_{JS} &= \frac{\partial \vec{s}}{\partial x} (x_{BD} - x_{JS}) + \frac{\partial \vec{s}}{\partial y} (y_{BD} - y_{JS}) + \dots \\ \vec{s}_{BM} - \vec{s}_{JS} &= \frac{\partial \vec{s}}{\partial x} (x_{BM} - x_{JS}) + \frac{\partial \vec{s}}{\partial y} (y_{BM} - y_{JS}) + \dots\end{aligned}\quad (3)$$

and, to the extent that \vec{s} varies linearly over the region, solve for the four unknowns $\partial \vec{s}/\partial x$, $\partial \vec{s}/\partial y$ using estimates of the quantities Δx_{BM-JS}^j , Δy_{BM-JS}^j , Δx_{BD-JS}^j , and Δy_{BD-JS}^j which are available from the smoothed state vector at times t_j .

The strain rate tensor used here is defined in the usual manner:

$$\dot{\epsilon} = \begin{pmatrix} \frac{\partial u}{\partial x} & \frac{1}{2}(\frac{\partial u}{\partial y} + \frac{\partial v}{\partial x}) \\ \frac{1}{2}(\frac{\partial u}{\partial y} + \frac{\partial v}{\partial x}) & \frac{\partial v}{\partial y} \end{pmatrix}$$

The velocity derivatives from which $\dot{\epsilon}$ is constructed can be calculated using eq. 3 and the results of the Kalman smoothing. Specifically, one associates

$$\vec{s}_{BD} - \vec{s}_{JS} \text{ with } \begin{pmatrix} \Delta u_{BD-JS} \\ \Delta v_{BD-JS} \end{pmatrix}, \quad \text{and } \vec{s}_{BM} - \vec{s}_{JS} \text{ with } \begin{pmatrix} \Delta u_{BM-JS} \\ \Delta v_{BM-JS} \end{pmatrix}$$

and solves for $\partial u/\partial x$, $\partial v/\partial x$, $\partial u/\partial y$, and $\partial v/\partial y$.

To define a measure of strain we need a reference configuration. We arbitrarily take it to be the configuration of the array at the outset of the experiment, $t_0 = 1776$ hr (= day 74 = 0000 GMT 14 March 1972). Displacement vectors are defined for each station:

$$\vec{x}_{JS}^j - \vec{x}_{JS}^0,$$

$$\vec{x}_{BD}^j - \vec{x}_{BD}^0, \quad \text{and}$$

$$\vec{x}_{BM}^j - \vec{x}_{BM}^0$$

Then, to use eq. 3 again, we associate

$$\vec{s}_{BD} - \vec{s}_{JS} \quad \text{with} \quad (\vec{x}_{BD}^j - \vec{x}_{BD}^0) - (\vec{x}_{JS}^j - \vec{x}_{JS}^0) = (\Delta\vec{x}_{BD-JS}^j - \Delta\vec{x}_{BD-JS}^0)$$

and

$$\vec{s}_{BM} - \vec{s}_{JS} = (\Delta\vec{x}_{BM-JS}^j - \Delta\vec{x}_{BM-JS}^0).$$

The derivatives $\partial\vec{s}/\partial x$, $\partial\vec{s}/\partial y$ are the displacement derivatives from which a linear strain measure is constructed:

$$\hat{\boldsymbol{\varepsilon}} = \begin{pmatrix} \frac{\partial s_1}{\partial x} & \frac{1}{2}(\frac{\partial s_2}{\partial x} + \frac{\partial s_1}{\partial y}) \\ \frac{1}{2}(\frac{\partial s_2}{\partial x} + \frac{\partial s_1}{\partial y}) & \frac{\partial s_2}{\partial y} \end{pmatrix}$$

In the calculations reported here, the reference t_0 configuration (not the present configuration) is used in the right-hand side of eq. 3 to obtain the strain estimates.

ERRORS

Before presenting the results of the strain and strain rate calculations we turn to a discussion of errors. The strains and strain rates treated above have been defined in terms of the motions of three Lagrangian points. No attempt, except an appeal to intuition, is made to relate these three point strains to definitions using limits of strain at a point. Certainly the strains reported here do depend on which three points were chosen. The errors we discuss here come from errors in measuring the motion of the three points. The arguments made are not as fancy as they might be, but greater rigor was thought to be incompatible with our substantial ignorance of some of the parameters. Suppose the position measurements at two stations have independent errors with variance σ^2 . Then the errors in the separation between them (thinking in one dimension only) have variance $2\sigma^2$. This would

be true if we took a single measurement simultaneously at both stations. But if the measurements happened to be separated by a time τ , we would have to know what the variance of the ice motion itself was over such a time to estimate the variance of the separation errors; and the larger τ became, the larger that variance would become. On the other hand, if we had many more measurements per unit time, we would benefit from an averaging effect and realize a reduction in the variance.

The Kalman smoothing procedure involves direct calculation of the estimation error covariance. As expected, the covariances depend on the measurement variance, the spacing of the measurements in time, and an assumption about how the ice behaves. The error covariance increases as the measurement variance increases, as the sampling density decreases, or as the ice is assumed to have larger high-frequency motions. The physical assumption about the ice is embedded in the state transition equation 1. Driven by white noise and with constant sampling interval Δt , the first-order, autoregressive model for the ice has the power spectral density $S(f) = \Delta t \sigma^2 / 2(1 - \cos 2\pi f \Delta t)$ drawn in Figure 4.

The general agreement between this assumed spectrum and the spectra calculated from the motions of previous drifting stations supports the use of such a simple model. Of course, with the data now in hand, we should consider improvements to the model that would represent the high-frequency spectrum better.

Typical values of the calculated smoothing covariance matrix are given in Table 2. The main diagonal elements should be interpreted as the variances of the errors in estimating the state vector components. The value of $88 \text{ m}^2/\text{hr}^2$ for $\text{cov}(\Delta u_3, \Delta u_3)$, for example, means that the standard deviation of the error in estimating the x -component of the relative velocity between the first and third stations was $\sim 10 \text{ m hr}^{-1}$.

Additional variance is introduced in the strain and strain rate errors by taking spatial derivatives, since the positions of the three points themselves are not known exactly, but the dominant errors are in the estimates of the displacement and velocity differences. A final error source, also assumed to be small, arises from interpolating between measurement

TABLE 2
SMOOTHING ERROR COVARIANCE MATRIX UNDER TYPICAL CONDITIONS

	x	v	Δx_{12}	Δv_{12}	Δx_{13}	Δv_{13}
x	1590 m^2	-13 $m^2\text{hr}^{-1}$	73 m^2	-17 $m^2\text{hr}^{-1}$	67 m^2	-18 $m^2\text{hr}^{-1}$
v	-13 $m^2\text{hr}^{-1}$	106 $m^2\text{hr}^{-2}$	-27 $m^2\text{hr}^{-1}$	11 $m^2\text{hr}^{-2}$	-43 $m^2\text{hr}^{-1}$	22 $m^2\text{hr}^{-2}$
Δx_{12}	73 m^2	-27 $m^2\text{hr}^{-1}$	1790 m^2	-94 $m^2\text{hr}^{-1}$	653 m^2	-28 $m^2\text{hr}^{-1}$
Δv_{12}	-17 $m^2\text{hr}^{-1}$	11 $m^2\text{hr}^{-2}$	-94 $m^2\text{hr}^{-1}$	99 $m^2\text{hr}^{-2}$	-18 $m^2\text{hr}^{-1}$	35 $m^2\text{hr}^{-2}$
Δx_{13}	67 m^2	-43 $m^2\text{hr}^{-1}$	653 m^2	-18 $m^2\text{hr}^{-2}$	1600 m^2	-111 $m^2\text{hr}^{-1}$
Δv_{13}	-18 $m^2\text{hr}^{-1}$	22 $m^2\text{hr}^{-2}$	-28 $m^2\text{hr}^{-1}$	35 $m^2\text{hr}^{-2}$	-111 $m^2\text{hr}^{-1}$	88 $m^2\text{hr}^{-2}$

points to get output results at equally spaced times. Under typical conditions the standard deviations in the strain and strain rate estimates are approximately 6×10^{-4} for each strain component and $8 \times 10^{-5} \text{ hr}^{-1}$ for each strain rate component. When the data rate falls below several fixes per system per day, these values do not apply.

RESULTS OF THE CALCULATIONS

Figures 7 and 9 display the time series of the components of the strain and strain rate tensors referred to a Cartesian coordinate system for which x is positive to the east and y is positive to the north. The same results are presented in terms of principal values and principal directions in Figures 8 and 10. To make the results more accessible, component values and an estimate of the standard error have been given in Table 3. Times in the table are given in hours; for example, 1902 hr is the sixth hour, Greenwich mean time, of Julian day 79 (19 March 1972). At time 1902 hr, we read that the yy strain component is 0.0415 ± 0.0001 and the yy strain rate component is $-0.00045 \text{ hr}^{-1} \pm 0.00009 \text{ hr}^{-1}$. One point is given every six hours.

Two major gaps are found in the data (Fig. 3), one occurring at Brass Monkey on days 88-90 and the other at Blue Dog on days 99-108. The computational procedure discussed in this report is unmoved by missing data

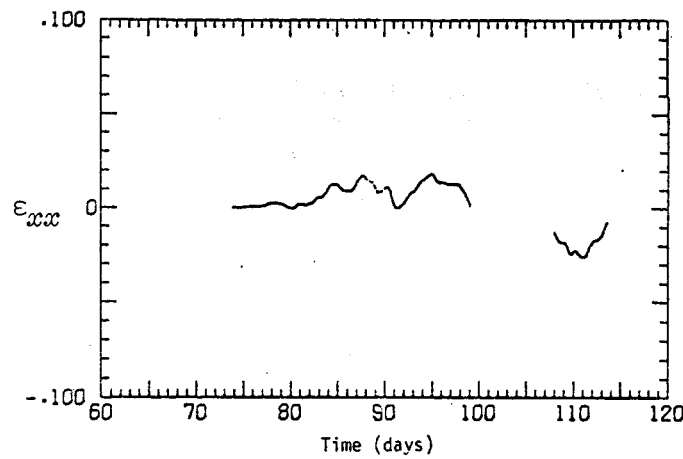


Fig. 7a. The east-west normal component of the strain tensor, AIDJEX 1972, versus time.

Fig. 7b. The north-south normal component of the strain tensor, AIDJEX 1972, versus time.

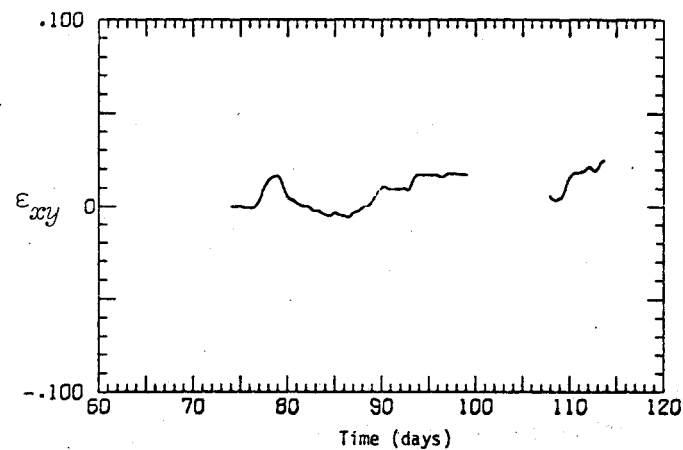
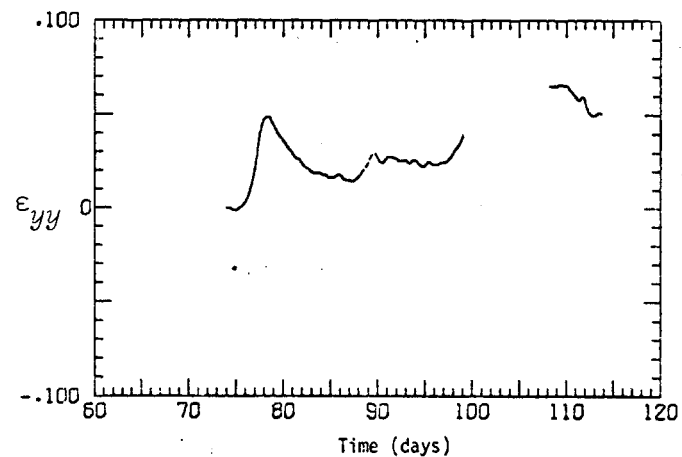


Fig. 7c. The shear component of the strain tensor, AIDJEX 1972, versus time.

Fig. 8a. The major principal value of the strain tensor, AIDJEX 1972, versus time.

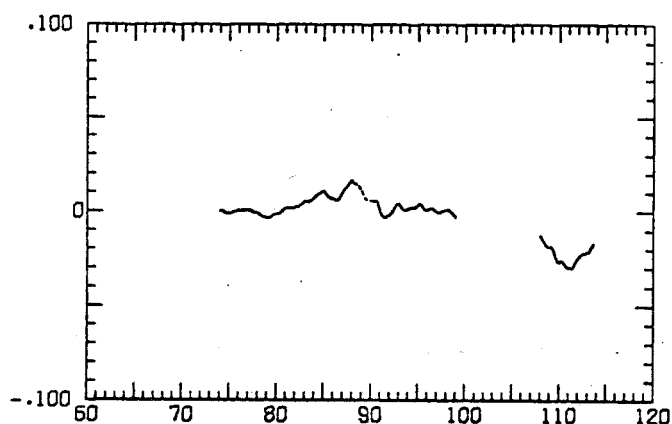
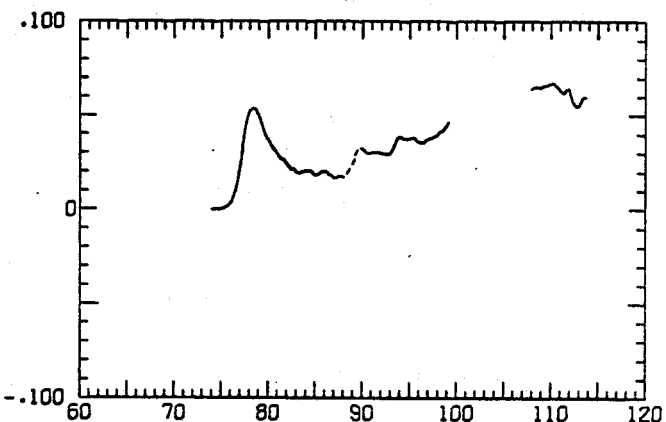
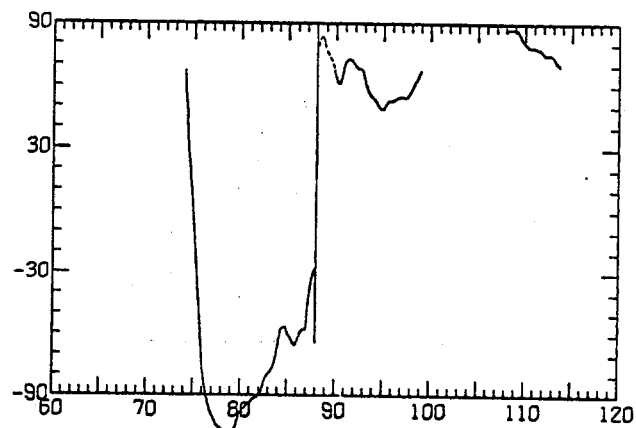


Fig. 8b. The minor principal value of the strain tensor, AIDJEX 1972, versus time.

Fig. 8c. The principal direction (degrees counterclockwise from east), of the strain tensor, AIDJEX 1972, versus time.



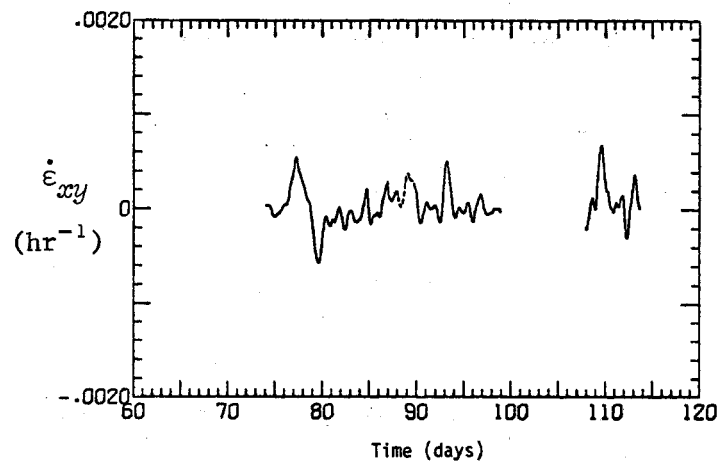


Fig. 9a. The shear component of the strain rate tensor (per hour), AIDJEX 1972, versus time.

Fig. 9b. The north-south normal component of the strain rate tensor (per hour), AIDJEX 1972, versus time.

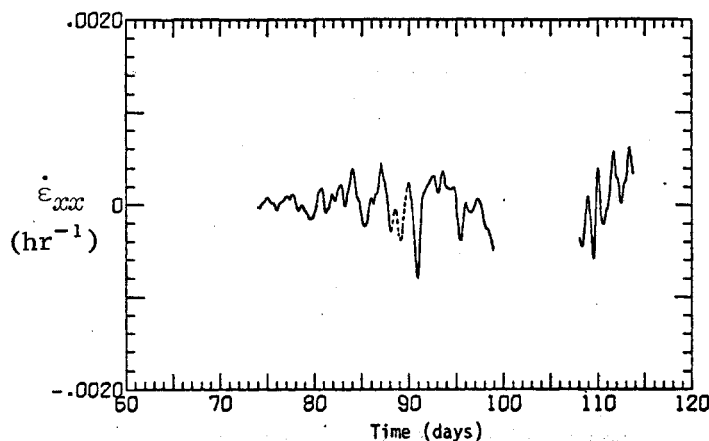
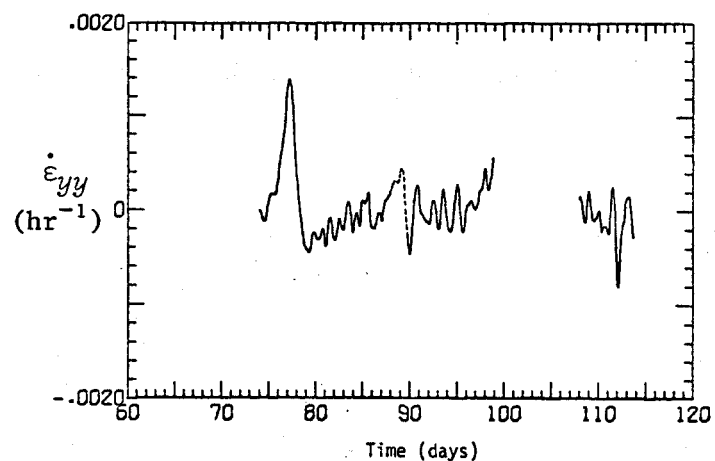


Fig. 9c. The east-west normal component of the strain rate tensor (per hour), AIDJEX 1972, versus time.

Fig. 10a. The major principal value of the strain rate tensor (per hour), AIDJEX 1972, versus time.

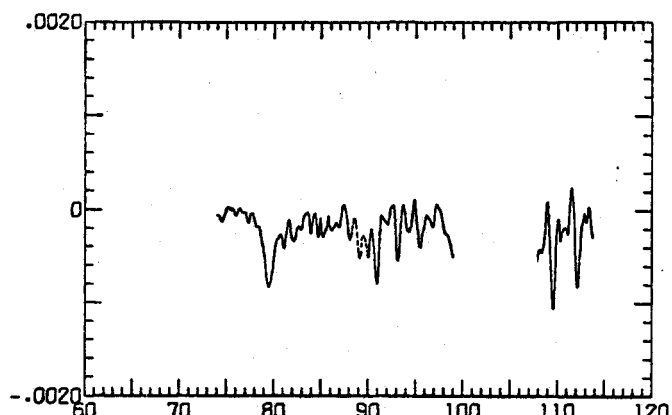
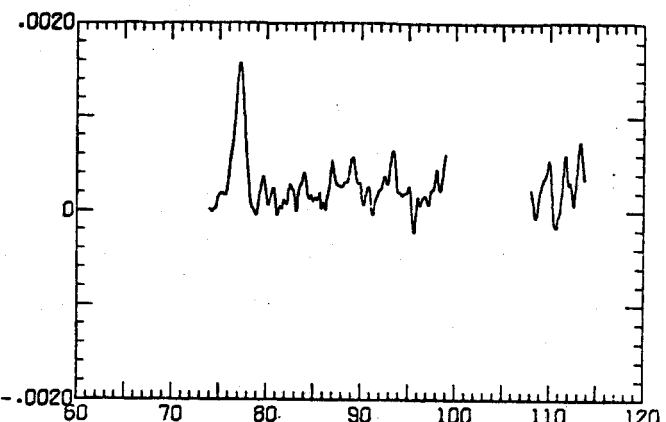


Fig. 10b. The minor principal value of the strain rate tensor (per hour), AIDJEX 1972, versus time.

Fig. 10c. The principal direction (degrees counterclockwise from east) of the strain rate tensor, AIDJEX 1972, versus time.

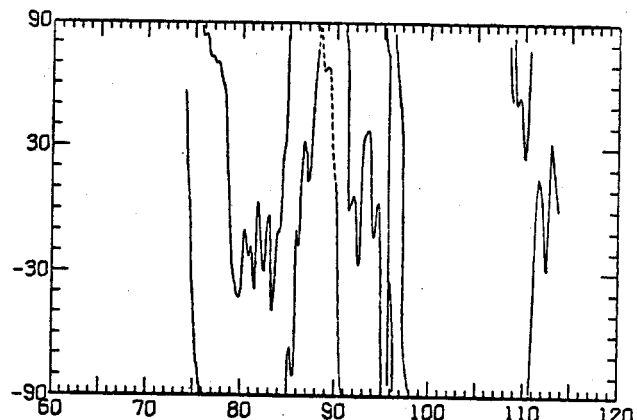


TABLE 3

COMPONENT VALUES AND ESTIMATES OF STANDARD ERROR FOR STRAIN AND STRAIN RATE TENSORS

TIME	S T R A I N				S T R A I N R A T E			
	XX-COMP	YY-COMP	XY-COMP	1 SIGMA	XX-COMP	YY-COMP	XY-COMP	1 SIGMA
1776	-2.95E-06	3.50E-06	3.35E-06	1.9E-04	-3.2E-05	-6.0E-07	3.7E-05	1.9E-04
1782	-2.01E-04	-1.84E-04	1.97E-04	1.7E-04	-1.8E-05	-7.0E-05	3.1E-05	1.7E-04
1788	-1.77E-04	-7.90E-04	3.94E-04	1.3E-04	2.6E-05	-1.2E-04	2.4E-05	1.3E-04
1794	3.80E-05	-1.34E-03	3.20E-04	1.0E-04	5.5E-05	-2.0E-05	-6.4E-05	1.0E-04
1800	4.95E-04	-1.03E-03	-1.59E-04	1.0E-04	8.3E-05	1.2E-04	-7.7E-05	1.0E-04
1806	8.55E-04	-1.08E-04	-5.54E-04	1.0E-04	2.8E-05	1.7E-04	-5.1E-05	1.0E-04
1812	9.62E-04	9.19E-04	-8.00E-04	9.6E-05	1.6E-05	1.7E-04	-2.7E-05	9.5E-05
1818	1.01E-03	1.94E-03	-8.70E-04	9.1E-05	-3.3E-06	1.9E-04	5.6E-06	9.1E-05
1824	7.61E-04	3.47E-03	-6.91E-04	9.2E-05	-5.7E-05	3.4E-04	4.9E-05	9.2E-05
1830	5.96E-04	6.27E-03	-3.96E-04	1.0E-04	1.2E-05	5.7E-04	5.5E-05	9.9E-05
1836	7.32E-04	1.02E-02	1.49E-04	9.8E-05	3.8E-05	7.4E-04	1.7E-04	9.6E-05
1842	9.61E-04	1.52E-02	1.62E-03	9.1E-05	5.9E-05	9.4E-04	3.0E-04	8.9E-05
1848	1.34E-03	2.23E-02	3.79E-03	8.7E-05	9.9E-05	1.3E-03	4.2E-04	8.4E-05
1854	1.69E-03	3.07E-02	6.87E-03	8.8E-05	6.6E-05	1.4E-03	5.5E-04	8.4E-05
1860	1.95E-03	3.87E-02	1.00E-02	9.6E-05	1.0E-04	1.2E-03	4.4E-04	9.1E-05
1866	2.49E-03	4.47E-02	1.24E-02	9.3E-05	1.1E-04	7.0E-04	3.4E-04	8.7E-05
1872	2.79E-03	4.77E-02	1.43E-02	8.9E-05	9.9E-06	3.1E-04	2.6E-04	8.3E-05
1878	2.45E-03	4.87E-02	1.57E-02	1.0E-04	-6.6E-05	3.7E-05	1.6E-04	9.4E-05
1884	2.15E-03	4.82E-02	1.64E-02	1.0E-04	-7.4E-06	-1.8E-04	8.2E-05	9.6E-05
1890	2.12E-03	4.65E-02	1.68E-02	9.9E-05	-1.3E-05	-3.6E-04	1.2E-05	9.2E-05
1896	1.91E-03	4.41E-02	1.63E-02	9.8E-05	-7.4E-05	-4.2E-04	-1.7E-04	9.2E-05
1902	1.53E-03	4.15E-02	1.44E-02	9.9E-05	-1.1E-04	-4.5E-04	-4.2E-04	9.3E-05
1908	8.84E-04	3.90E-02	1.13E-02	9.3E-05	-1.6E-04	-3.6E-04	-5.6E-04	8.8E-05
1914	1.80E-04	3.74E-02	7.72E-03	8.3E-05	-1.4E-04	-2.4E-04	-5.2E-04	7.9E-05
1920	-3.59E-04	3.59E-02	5.04E-03	8.5E-05	-7.5E-05	-2.8E-04	-3.2E-04	8.1E-05
1926	-3.58E-04	3.40E-02	3.88E-03	8.5E-05	6.9E-05	-3.1E-04	-9.8E-05	8.2E-05
1932	3.72E-04	3.22E-02	3.39E-03	8.6E-05	1.6E-04	-2.8E-04	-9.2E-05	8.2E-05
1938	1.46E-03	3.07E-02	2.57E-03	8.7E-05	1.8E-04	-2.0E-04	-1.8E-04	8.3E-05
1944	2.15E-03	2.91E-02	1.58E-03	8.9E-05	6.0E-06	-3.6E-04	-1.3E-04	8.6E-05
1950	1.79E-03	2.70E-02	8.61E-04	8.9E-05	-6.7E-05	-2.2E-04	-1.4E-04	8.6E-05
1956	1.57E-03	2.63E-02	1.44E-04	9.2E-05	-7.4E-06	-7.7E-05	-6.1E-05	8.9E-05
1962	1.84E-03	2.55E-02	4.35E-05	9.0E-05	1.1E-04	-2.1E-04	2.0E-05	8.7E-05
1968	2.51E-03	2.38E-02	8.03E-05	9.0E-05	7.9E-05	-3.2E-04	-4.8E-05	8.7E-05
1974	2.84E-03	2.20E-02	-5.90E-04	8.5E-05	7.6E-05	-2.2E-04	-1.8E-04	8.2E-05
1980	3.68E-03	2.11E-02	-1.81E-03	8.6E-05	1.8E-04	-7.9E-05	-2.0E-04	8.4E-05
1986	4.93E-03	2.03E-02	-2.52E-03	8.4E-05	2.2E-04	-1.9E-04	-4.9E-05	8.2E-05
1992	6.02E-03	1.91E-02	-2.64E-03	9.3E-05	8.4E-05	-1.6E-04	-1.2E-05	9.1E-05
1998	6.05E-03	1.86E-02	-2.82E-03	9.1E-05	-1.4E-07	1.7E-05	-6.6E-05	8.8E-05
2004	6.49E-03	1.90E-02	-3.47E-03	9.4E-05	1.5E-04	8.8E-05	-1.4E-04	9.5E-05
2010	7.75E-03	1.92E-02	-4.29E-03	9.5E-05	2.7E-04	-6.9E-05	-1.3E-04	9.3E-05

TABLE 3 (continued)

TIME	STRAIN			STRAIN RATE				
	XX-COMP	YY-COMP	XY-COMP	1 SIGMA	XX-COMP	YY-COMP	XY-COMP	1 SIGMA
2016	9.88E-03	1.80E-02	-4.96E-03	8.9E-05	4.0E-04	-1.7E-04	-1.1E-04	9.0E-05
2022	1.20E-02	1.74E-02	-5.36E-03	8.7E-05	2.6E-04	-3.2E-05	-1.8E-05	8.8E-05
2028	1.28E-02	1.71E-02	-5.00E-03	8.0E-05	7.0E-05	-1.1E-04	1.3E-04	8.0E-05
2034	1.30E-02	1.62E-02	-3.87E-03	8.6E-05	1.8E-05	-1.1E-04	2.1E-04	8.4E-05
2040	1.25E-02	1.64E-02	-3.41E-03	9.0E-05	-1.4E-04	1.1E-04	-9.1E-05	8.7E-05
2046	1.12E-02	1.68E-02	-4.30E-03	8.3E-05	-2.3E-04	7.1E-05	-1.3E-04	8.1E-05
2052	9.73E-03	1.73E-02	-4.86E-03	8.2E-05	-1.9E-04	1.7E-04	-6.4E-05	7.9E-05
2058	8.90E-03	1.80E-02	-5.28E-03	8.9E-05	-6.3E-06	-2.7E-05	-4.1E-05	8.6E-05
2064	9.14E-03	1.70E-02	-5.55E-03	9.3E-05	7.8E-05	-1.9E-04	-8.0E-05	9.0E-05
2070	9.18E-03	1.60E-02	-5.95E-03	9.5E-05	1.5E-05	-2.0E-04	-7.6E-06	9.2E-05
2076	9.60E-03	1.50E-02	-5.53E-03	9.1E-05	1.3E-04	-9.8E-05	1.2E-04	8.7E-05
2082	1.04E-02	1.48E-02	-4.41E-03	9.2E-05	2.1E-04	-3.3E-05	2.3E-04	8.9E-05
2088	1.28E-02	1.44E-02	-3.31E-03	1.4E-04	4.6E-04	-1.2E-04	1.5E-04	1.4E-04
2094	1.52E-02	1.43E-02	-2.54E-03	1.7E-04	3.1E-04	6.2E-05	8.9E-05	1.6E-04
2100	1.67E-02	1.50E-02	-1.95E-03	1.6E-04	1.8E-04	1.2E-04	1.2E-04	1.6E-04
2106	1.73E-02	1.59E-02	-1.04E-03	1.6E-04	-2.2E-05	1.6E-04	1.8E-04	1.5E-04
2112	1.64E-02	1.71E-02	5.14E-05	1.5E-04	-2.6E-04	2.1E-04	1.6E-04	1.4E-04
2118	1.47E-02	1.86E-02	6.39E-04	1.4E-04	-2.2E-04	3.1E-04	3.4E-05	1.4E-04
2124	1.38E-02	2.06E-02	7.87E-04	1.4E-04	-6.1E-05	3.0E-04	7.4E-05	1.3E-04
2130	1.34E-02	2.24E-02	1.63E-03	1.4E-04	-1.6E-04	3.0E-04	2.5E-04	1.4E-04
2136	1.17E-02	2.47E-02	3.49E-03	1.5E-04	-3.6E-04	4.1E-04	3.7E-04	1.4E-04
2142	9.44E-03	2.74E-02	5.64E-03	1.6E-04	-2.4E-04	4.2E-04	3.2E-04	1.5E-04
2148	8.55E-03	2.94E-02	7.46E-03	1.6E-04	-9.7E-07	9.7E-05	3.0E-04	1.6E-04
2154	9.07E-03	2.90E-02	9.21E-03	1.6E-04	1.9E-04	-2.8E-04	2.5E-04	1.5E-04
2160	1.05E-02	2.67E-02	1.06E-02	1.5E-04	2.2E-04	-4.7E-04	1.7E-04	1.4E-04
2166	1.13E-02	2.46E-02	1.08E-02	1.1E-04	2.4E-05	-1.7E-04	-1.0E-04	1.1E-04
2172	1.04E-02	2.46E-02	9.90E-03	7.9E-05	-3.0E-04	1.5E-04	-1.3E-04	7.6E-05
2178	7.41E-03	2.59E-02	9.34E-03	7.3E-05	-6.7E-04	2.6E-04	-2.8E-05	7.0E-05
2184	2.83E-03	2.74E-02	9.31E-03	8.1E-05	-7.4E-04	1.6E-04	6.6E-05	7.7E-05
2190	1.14E-04	2.76E-02	9.61E-03	7.2E-05	-1.8E-04	-4.3E-05	3.6E-05	6.9E-05
2196	3.03E-04	2.73E-02	9.66E-03	7.5E-05	1.2E-04	-8.6E-05	4.9E-06	7.2E-05
2202	1.22E-03	2.66E-02	9.77E-03	7.8E-05	1.9E-04	-1.2E-04	2.3E-05	7.5E-05
2208	2.50E-03	2.59E-02	1.00E-02	9.7E-05	2.4E-04	-1.5E-04	4.0E-05	9.3E-05
2214	4.03E-03	2.52E-02	1.01E-02	8.9E-05	2.8E-04	-2.6E-05	-6.1E-05	8.6E-05
2220	5.85E-03	2.55E-02	9.43E-03	8.2E-05	3.2E-04	1.1E-04	-1.3E-04	8.3E-05
2226	7.74E-03	2.60E-02	9.03E-03	8.5E-05	2.8E-04	1.2E-05	4.7E-05	8.5E-05
2232	8.85E-03	2.53E-02	1.05E-02	9.6E-05	1.4E-04	-2.0E-04	4.1E-04	9.3E-05
2238	9.64E-03	2.43E-02	1.35E-02	9.6E-05	2.4E-04	-5.3E-05	5.0E-04	9.3E-05
2244	1.14E-02	2.49E-02	1.62E-02	8.9E-05	3.7E-04	2.2E-04	3.1E-04	8.4E-05
2250	1.33E-02	2.59E-02	1.74E-02	8.8E-05	2.7E-04	7.7E-05	9.5E-05	8.4E-05

TABLE 3 (continued)

TIME	STRAIN			STRAIN RATE				
	XX-COMP	YY-COMP	XY-COMP	1 SIGMA	XX-COMP	YY-COMP	XY-COMP	1 SIGMA
2256	1.46E-02	2.56E-02	1.76E-02	9.5E-05	1.9E-04	-1.3E-04	-6.9E-05	9.0E-05
2262	1.56E-02	2.42E-02	1.71E-02	8.7E-05	1.8E-04	-2.3E-04	-6.2E-05	8.3E-05
2268	1.66E-02	2.28E-02	1.71E-02	8.1E-05	1.8E-04	-1.6E-04	2.2E-05	7.7E-05
2274	1.77E-02	2.22E-02	1.72E-02	8.4E-05	1.9E-04	7.4E-05	-2.8E-05	8.0E-05
2280	1.85E-02	2.32E-02	1.70E-02	9.6E-05	-1.1E-05	2.7E-04	-3.4E-05	9.1E-05
2286	1.75E-02	2.46E-02	1.69E-02	8.3E-05	-2.7E-04	1.3E-04	3.2E-05	7.9E-05
2292	1.54E-02	2.46E-02	1.72E-02	8.9E-05	-3.8E-04	-1.7E-04	5.9E-05	8.4E-05
2298	1.36E-02	2.35E-02	1.72E-02	8.9E-05	-1.6E-04	-2.0E-04	-5.3E-05	8.4E-05
2304	1.35E-02	2.31E-02	1.65E-02	9.6E-05	2.7E-05	1.8E-05	-1.3E-04	9.1E-05
2310	1.34E-02	2.36E-02	1.61E-02	8.6E-05	-6.3E-05	6.4E-05	9.8E-06	8.2E-05
2316	1.30E-02	2.42E-02	1.64E-02	8.6E-05	-7.3E-05	1.0E-04	9.2E-05	8.2E-05
2322	1.26E-02	2.48E-02	1.72E-02	9.3E-05	-4.6E-05	3.2E-05	1.7E-04	8.9E-05
2328	1.24E-02	2.49E-02	1.81E-02	9.8E-05	4.7E-06	1.2E-05	1.1E-04	9.4E-05
2334	1.27E-02	2.52E-02	1.83E-02	9.4E-05	7.0E-05	9.5E-05	-2.0E-05	8.9E-05
2340	1.30E-02	2.62E-02	1.80E-02	8.7E-05	2.4E-05	2.2E-04	-5.4E-05	8.3E-05
2346	1.29E-02	2.75E-02	1.77E-02	8.8E-05	-6.1E-05	2.7E-04	-3.5E-05	8.3E-05
2352	1.19E-02	2.97E-02	1.75E-02	9.0E-05	-2.2E-04	4.5E-04	-3.0E-05	8.5E-05
2358	1.04E-02	3.18E-02	1.73E-02	8.5E-05	-2.7E-04	2.6E-04	8.3E-06	8.1E-05
2364	8.65E-03	3.32E-02	1.73E-02	9.0E-05	-3.0E-04	2.6E-04	3.6E-06	8.5E-05
2370	6.48E-03	3.52E-02	1.72E-02	1.1E-04	-4.0E-04	4.5E-04	-4.5E-06	1.1E-04
2376	3.59E-03	3.85E-02	1.69E-02	1.6E-04	-5.3E-04	6.1E-04	-6.0E-05	1.6E-04
2382	3.45E-04	4.19E-02	1.61E-02	1.9E-04	-4.9E-04	5.4E-04	-1.6E-04	2.0E-04
2388	-2.24E-03	4.47E-02	1.47E-02	2.1E-04	-3.8E-04	3.7E-04	-2.2E-04	2.1E-04
2394	-4.74E-03	4.58E-02	1.37E-02	2.2E-04	-5.1E-04	3.8E-05	-1.9E-05	2.3E-04
2400	-8.94E-03	4.32E-02	1.54E-02	2.4E-04	-8.0E-04	-9.1E-04	5.2E-04	2.4E-04
2406	-1.22E-02	4.10E-02	1.63E-02	2.4E-04	-1.7E-04	4.7E-04	-3.7E-04	2.5E-04
2412	-1.35E-02	4.30E-02	1.47E-02	2.4E-04	-3.7E-04	1.1E-04	-2.9E-05	2.5E-04
2418	-1.60E-02	4.31E-02	1.51E-02	2.4E-04	-4.4E-04	-2.1E-05	1.4E-04	2.5E-04
2424	-1.85E-02	4.35E-02	1.61E-02	2.4E-04	-4.0E-04	1.6E-04	2.0E-04	2.5E-04
2430	-2.11E-02	4.55E-02	1.76E-02	2.4E-04	-4.0E-04	4.7E-04	3.6E-04	2.5E-04
2436	-2.35E-02	4.90E-02	2.02E-02	2.3E-04	-3.3E-04	6.5E-04	5.0E-04	2.4E-04
2442	-2.52E-02	5.36E-02	2.36E-02	2.3E-04	-1.5E-04	8.1E-04	6.0E-04	2.4E-04
2448	-2.58E-02	5.87E-02	2.72E-02	2.2E-04	5.4E-05	7.6E-04	5.8E-04	2.3E-04
2454	-2.58E-02	6.34E-02	3.07E-02	2.2E-04	1.7E-05	7.2E-04	5.4E-04	2.3E-04
2460	-2.63E-02	6.79E-02	3.40E-02	2.2E-04	-7.4E-05	6.7E-04	5.3E-04	2.3E-04
2466	-2.68E-02	7.18E-02	3.71E-02	2.2E-04	3.3E-05	5.5E-04	4.4E-04	2.2E-04
2472	-2.60E-02	7.47E-02	3.93E-02	2.1E-04	3.4E-04	3.1E-04	2.1E-04	2.2E-04
2478	-2.37E-02	7.58E-02	4.04E-02	2.1E-04	4.9E-04	6.7E-05	7.9E-05	2.2E-04
2484	-2.03E-02	7.53E-02	4.08E-02	2.1E-04	6.8E-04	-1.7E-04	-2.7E-05	2.2E-04
2490	-1.58E-02	7.37E-02	4.10E-02	2.1E-04	9.0E-04	-2.4E-04	-5.4E-05	2.2E-04

TABLE 3 (continued)

TIME	STRAIN			STRAIN RATE				
	XX-COMP	YY-COMP	XY-COMP	1 SIGMA	XX-COMP	YY-COMP	XY-COMP	1 SIGMA
2496	-1.00E-02	7.18E-02	4.09E-02	2.1E-04	1.0E-03	-2.8E-04	-1.1E-04	2.2E-04
2502	-3.90E-03	6.93E-02	4.07E-02	2.1E-04	1.0E-03	-3.9E-04	-1.4E-04	2.2E-04
2508	1.95E-03	6.61E-02	4.03E-02	2.2E-04	9.3E-04	-5.4E-04	-1.4E-04	2.2E-04
2514	7.38E-03	6.22E-02	3.98E-02	2.2E-04	8.7E-04	-6.1E-04	-2.1E-04	2.2E-04
2520	1.25E-02	5.92E-02	3.81E-02	2.3E-04	6.7E-04	-2.6E-04	-4.6E-04	2.3E-04
2526	1.57E-02	5.77E-02	3.51E-02	2.3E-04	3.1E-04	-2.4E-04	-5.6E-04	2.3E-04
2532	1.73E-02	5.52E-02	3.14E-02	2.4E-04	1.4E-04	-4.4E-04	-6.8E-04	2.4E-04
2538	1.82E-02	5.26E-02	2.65E-02	2.4E-04	5.2E-05	-2.1E-04	-8.8E-04	2.4E-04
2544	1.87E-02	5.23E-02	2.07E-02	2.4E-04	-1.4E-04	2.3E-04	-8.9E-04	2.4E-04
2550	1.66E-02	5.33E-02	1.63E-02	2.4E-04	-6.2E-04	1.6E-04	-4.8E-04	2.4E-04
2556	1.21E-02	5.37E-02	1.39E-02	2.4E-04	-8.3E-04	1.5E-04	-2.6E-04	2.4E-04
2562	7.18E-03	5.54E-02	1.21E-02	2.4E-04	-8.1E-04	4.4E-04	-2.6E-04	2.4E-04
2568	2.73E-03	5.86E-02	9.98E-03	2.3E-04	-7.5E-04	6.0E-04	-2.9E-04	2.3E-04
2574	-1.72E-03	6.19E-02	8.03E-03	2.2E-04	-7.8E-04	3.8E-04	-2.1E-04	2.3E-04
2580	-6.26E-03	6.32E-02	6.91E-03	2.0E-04	-7.5E-04	9.4E-05	-8.6E-05	2.1E-04
2586	-1.02E-02	6.37E-02	6.11E-03	1.8E-04	-5.7E-04	7.7E-05	-1.3E-04	1.9E-04
2592	-1.27E-02	6.44E-02	4.78E-03	1.5E-04	-3.6E-04	1.5E-04	-2.2E-04	1.5E-04
2598	-1.48E-02	6.52E-02	3.74E-03	8.9E-05	-4.4E-04	7.4E-05	-6.5E-05	9.3E-05
2604	-1.74E-02	6.51E-02	3.76E-03	9.2E-05	-3.5E-04	-1.0E-04	9.4E-05	8.4E-05
2610	-1.85E-02	6.45E-02	4.43E-03	9.2E-05	-2.3E-05	9.1E-06	6.8E-05	8.5E-05
2616	-1.84E-02	6.52E-02	4.61E-03	9.1E-05	9.1E-05	2.1E-04	1.3E-05	8.3E-05
2622	-1.89E-02	6.58E-02	6.04E-03	9.4E-05	-1.7E-04	-1.3E-05	4.0E-04	8.5E-05
2628	-2.16E-02	6.53E-02	9.43E-03	9.7E-05	-5.8E-04	-1.1E-04	6.7E-04	8.8E-05
2634	-2.47E-02	6.49E-02	1.34E-02	1.0E-04	-1.5E-04	-8.2E-05	5.7E-04	9.1E-05
2640	-2.37E-02	6.47E-02	1.60E-02	8.6E-05	4.0E-04	4.6E-07	2.6E-04	7.7E-05
2646	-2.27E-02	6.40E-02	1.75E-02	8.1E-05	1.5E-05	-1.7E-04	1.9E-04	8.2E-05
2652	-2.39E-02	6.23E-02	1.85E-02	8.1E-05	-2.0E-04	-1.7E-04	4.2E-05	7.7E-05
2658	-2.54E-02	6.07E-02	1.87E-02	8.5E-05	-1.5E-04	-1.7E-04	-2.0E-05	8.5E-05
2664	-2.61E-02	5.91E-02	1.88E-02	7.9E-05	-3.8E-05	-2.4E-04	2.4E-05	7.3E-05
2670	-2.60E-02	5.78E-02	1.93E-02	7.8E-05	1.6E-04	-2.8E-05	4.8E-05	7.1E-05
2676	-2.44E-02	5.86E-02	1.96E-02	8.7E-05	4.5E-04	2.6E-04	5.7E-05	7.8E-05
2682	-2.13E-02	5.94E-02	2.05E-02	8.3E-05	5.5E-04	-2.1E-05	1.4E-04	7.4E-05
2688	-1.90E-02	5.73E-02	2.15E-02	9.0E-05	2.9E-04	-7.4E-04	3.2E-05	8.1E-05
2694	-1.73E-02	5.26E-02	2.08E-02	8.2E-05	1.9E-04	-5.9E-04	-3.1E-04	7.4E-05
2700	-1.68E-02	5.01E-02	1.94E-02	7.7E-05	1.9E-05	-1.9E-04	-1.3E-04	6.9E-05
2706	-1.62E-02	4.92E-02	1.96E-02	7.7E-05	2.4E-04	-4.8E-05	1.0E-04	6.9E-05
2712	-1.50E-02	4.96E-02	2.10E-02	8.1E-05	2.8E-04	1.3E-04	3.1E-04	7.3E-05
2718	-1.27E-02	5.05E-02	2.33E-02	8.2E-05	5.9E-04	1.6E-04	3.0E-04	7.3E-05
2724	-9.34E-03	5.10E-02	2.47E-02	8.0E-05	5.4E-04	-6.0E-05	8.1E-05	7.2E-05
2730	-6.89E-03	4.96E-02	2.51E-02	8.2E-05	3.0E-04	-3.1E-04	-7.3E-06	7.7E-05
2736	-6.30E-03	4.75E-02	2.52E-02	1.4E-04	-4.3E-05	-2.2E-04	-5.3E-05	1.2E-04
2742	-7.05E-03	4.63E-02	2.47E-02	1.4E-04	-1.1E-04	1.6E-05	-1.5E-04	1.3E-04
2748	-8.09E-03	4.63E-02	2.36E-02	2.7E-04	-1.5E-04	1.8E-04	-1.6E-04	2.4E-04

and continues to generate estimates of the relative positions and velocities of the three stations. When the data rate is low, the error covariances given by the Kalman filter become large, and one may decide to ignore the estimated values. In this spirit, the interval 88-90 has been partially and 99-108 totally masked in the plots.

SUMMARY

The method which has been described for obtaining measurements of the deformation of sea ice over a scale of 100 km requires that assumptions be made regarding the statistical nature of the measurement errors and of the motion of the ice itself. The assumptions made here are:

- 1) the measurement errors are independent, zero-mean, white Gaussian processes with typical variances of 100 m^2 ;
- 2) a reduction in the measurement variance of about 30% is possible by utilizing fixes in a translocation sense;
- 3) the ice velocities and relative velocities are given by a first-order autoregressive model driven by Gaussian white noise with variance $100 \text{ m}^2 \text{ hr}^{-4}$;
- 4) the velocities of ice stations separated by 100 km have a correlation coefficient of about 0.6.

A Kalman filtering approach used these assumptions to estimate the position and velocity time series of the three drifting stations. From these estimates the spatial derivatives of displacement and velocity were calculated and combined to give the components of the strain and strain rate tensors.

The uncertainties in the strain rate estimates are frequently comparable to the strain rate itself. Nevertheless, many features of the deformation history were clearly resolved as a result of the program.

The same measurement and processing scheme seems promising for future use, especially if the measurement errors can be reduced and the sampling density increased.

ACKNOWLEDGMENT

This work was supported by National Science Foundation Contract C-625 and by Office of Naval Research Arctic Program Contract N00014-67-A-0103-0007.

Of the many people who participated in the field work and data processing, I wish especially to thank Pat Martin, who coordinated the technical end of the experiment.

REFERENCES

- Hibler, W. D., W. F. Weeks, A. Kovacs, and S. F. Ackley. 1973. Differential sea ice drift I: spatial and temporal variations in mesoscale strain in sea ice. *AIDJEX Bulletin No. 21*, pp. 79-113.
- Meditch, J. S. 1969. *Stochastic Optimal Linear Estimation and Control*. New York: McGraw-Hill.
- Thorndike, A. S. 1973. An integrated system for measuring sea ice motions. In *Ocean 73, Proceedings of the 1973 IEEE International Conference on Engineering in the Ocean Environment*. IEEE Publ. No. 73 CH0774-0 OCC, pp. 490-499.

FRACTURE OF SEA ICE SHEETS DUE TO ISOSTATIC IMBALANCE

by

R. T. Schwaegler
Dept. of Civil Engineering
Seattle University
Seattle, Wa. 98122

ABSTRACT

The nonuniform thickness of sea ice sheets creates regions of isostatic shear imbalance. For an assumed ice thickness variation, the resulting bending stresses are determined to be sufficient to cause cracking. The ice sheet is modeled as a floating elastic plate with constant flexural rigidity. Variable thickness is obtained by representing the bottom surface as a sine wave. Upper and lower bound curves are obtained for the amplitude of the bottom surface variation versus ice breaking strength.

INTRODUCTION

The stated objective of AIDJEX is to reach an understanding of the interaction between sea ice and its environment. Such an understanding presupposes the ability to describe quantitatively the system by appropriate models of the ice, ocean, and atmosphere. While a large body of knowledge exists on modeling the atmosphere and ocean, considerable progress is still required to fully understand the actual behavior of sea ice under a variety of environmental conditions. A realistic sea ice model is, therefore, a prerequisite for future study and is a primary goal of AIDJEX.

The final model for predicting the motion of arctic pack ice requires a good mechanical constitutive law of pack ice (AIDJEX Bulletin No. 15, Scientific Plan). If the behavior of the ice is to be resolved on short time and space scales, the cracking of individual floes must be considered.

The motion of pack ice is basically that of the individual floes after they have broken from the ice sheet. The mechanisms that cause the ice field to crack and break into smaller floes then become important to the modeling effort. Preferably for the model, these mechanisms would be separate from those that move the pack ice about.

Several mechanisms have been proposed to explain the large-scale cracking patterns that lead to the breakup of pack ice. Evans and Untersteiner [1971] and Evans [1971] have recently investigated thermodynamics as a major source of cracks in perennial sea ice. Assur [1963] has investigated long water-wave cracks and has described the cracking patterns they produce. Isostatic shear imbalance, which results from the nonuniformity of the ice thickness, provides the stress environment for a third mechanism. Within this environment, contours of high flexural stress are developed throughout the ice field. The magnitude of these stress contours can reach levels that would be sufficient in themselves to cause local cracking. Alternately, when such a system of high-stress contours is present, any additional thermal loading or wave-wave action may combine to propagate existing cracks or initiate new ones. It is this type of loading mechanism which will be investigated in this paper.

As a preface to a mechanical analysis of the ice cover, some comment should be made regarding the topographic features found on the upper and lower surfaces of the pack ice. These surfaces figure significantly in the physical behavior of pack ice because they are so readily affected by atmospheric and oceanic currents. With the abundance of data available from past investigations of these surfaces and ice thickness, it would seem an easy task to construct a representative model of equilibrium ice having characteristic top and bottom surface roughness. Such is not the case, however. The random nature of the topographic features of arctic pack ice defies any simple structural idealization. Because of this, the ice is modeled as a floating sheet with sinusoidal variations of the top and bottom surfaces. The parameters required to define these surfaces include roughness amplitude, wavelength, and phase shift.

The findings of Hibler et al. [1972] have been used in this study to approximate the topographic features of the multiyear floe. Comparison of

typical upper and lower surfaces indicates that the average height of surface roughness of the bottom is approximately four to five times that of the top [Hibler et al., 1972], and the average wavelength of the bottom surface roughness is approximately four to five times as large as the corresponding top surface variation.

These surface characteristics have a dual effect on the ice-cracking mechanism under study. The first effect is shown by the direct relationship between the top and bottom surface variations and the magnitude of the isostatic shear imbalance. While the differential shear force created by adding a unit volume of ice to the top surface is approximately ten times as great as that created by adding the same volume to the bottom surface, the shorter wavelength of the top surface variation leads to local self-equilibrating shear. The bottom surface variations, with their greater wavelengths, permit shear imbalance conditions to develop over much larger areas of the ice. It is concluded, therefore, that the bottom surface is the principal source of isostatic shear imbalance for the assumed ice thickness profile. Preliminary studies have supported this conclusion.

The second effect is related to the section modulus used to determine stresses. Since the section modulus varies with the square of the ice thickness, the shape of the bottom surface will generally dictate the positions of critical bending stresses within the ice sheet.

In view of the dominating influence of bottom surface characteristics, we simplify our study by considering only bottom surface variations, and only those thickness variations that occur in "smooth" ice; that is, we exclude both pressure ridges and the flat ice found in frozen leads. Because no single structural model can adequately represent the complexity of actual ice conditions and behavior, we examine several models in this study, evaluating numerical examples of each and comparing the results.

We use two methods of analysis to determine the maximum flexural stress within the ice sheet model. The first method represents the ice sheet as a continuous plate on an elastic foundation. This is the most realistic approach, but it is also the most complex analytically. The second method yields similar stress results, but without the labor required to solve the elastic foundation problem.

In each analysis, the ice sheet is assumed to be an isotropic, homogeneous, linear elastic plate of variable thickness. The plate is also assumed to be unconstrained in the plane of its middle surface, to be in contact with the water over its entire lower surface, and to be out of the water on its top surface. Gravity and hydrostatic forces acting on the sheet as a free body are assumed to be in equilibrium. The plate is then analyzed to determine the nature of the local isostatic shear imbalance that results from the nonuniformity of the ice thickness.

The numerical values of the physical parameters used are:

$$\text{Young's modulus: } E = 10 \cdot 10^{10} \text{ dyn/cm}^2$$

$$\text{Poisson's ratio: } \mu = 0.29$$

$$\text{Equilibrium ice thickness: } H = 300 \text{ cm}$$

$$\text{Water density: } \rho_w = 10^{-3} \text{ kg/cm}^3$$

$$\text{Ice density: } \rho_I = 0.9 \cdot 10^{-3} \text{ kg/cm}^3$$

$$\text{Fracture stress of ice: } \sigma_M = 3.0 \cdot 10^6 \text{ dyn/cm}^2 = 3.0 \text{ bars.}$$

Each of these quantities is subject to considerable variation throughout the pack ice. The values chosen are intended as average values, compatible with those used by other authors [Weeks and Assur, 1967].

ONE-DIMENSIONAL ANALYSIS

Since the geometry of an actual ice plate is so difficult to define, we will examine three one-dimensional cases which place bounds on the general solution.

Infinite Beam on an Elastic Foundation

In the first case, we consider the ice sheet as an infinite beam on an elastic foundation [Hetyenyi, 1946], subject to a single sinusoidal variation of the bottom surface (Fig. 1a). The flexural rigidity of the beam is assumed to be constant, and the foundation modulus is provided by the supporting sea water. This case simulates conditions near the center of a large ice sheet that result from local unbalanced loadings. The ice is assumed at first to be of constant thickness H . The bottom surface is then permitted

to grow or erode to the depth $H \pm \Delta/2$ at the axis of symmetry. We will neglect the small change in freeboard that occurs as the ice grows or decays. Figure 1b shows the effective load variation applied to the infinite beam.

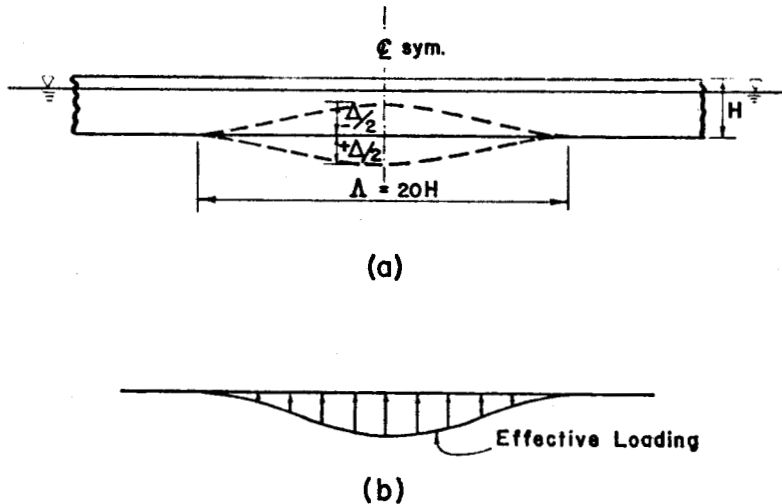


Fig. 1. Infinite beam on an elastic foundation.

Using this model, the following values are obtained for the physical parameters:

Equilibrium ice depth: $H = 3.0 \text{ m}$

Characteristic of elastic foundation system: $\lambda = \sqrt[4]{\frac{\rho_w g}{4EI}} = 0.0183 \text{ m}^{-1}$

Characteristic length of beam on elastic foundation:

$$1/\lambda = 54.6 \text{ m} = 18.2 H$$

Wavelength of bottom surface variation: $\Lambda = 20 H \approx 1/\lambda$

Bottom surface roughness ratio: $\Delta/H = 0.3 \rightarrow 1.0$

Mechanical properties of the ice have already been stated.

As noted above, the wavelength of the ice thickness variation is taken to be approximately equal to the characteristic length of the ice beam. Wavelengths greater than this cause little change in the computed bending moments in the beam. Numerical examples support this assertion.

The maximum bending stress, which occurs on the axis of symmetry, was evaluated for the range of bottom roughness ratios $0.3 \rightarrow 1.0$. The results, shown in Figure 2, indicate the insensitivity of the bending stress to shallow keels (lower curve). Quite the opposite is true for the case of negative keels or reduced ice thickness. The graph indicates the extreme sensitivity of the bending stress in areas of reduced ice thickness (upper curve).

The source of this sensitivity lies in the fact that the section modulus of the ice beam varies with the square of the ice depth at the axis of symmetry. For any given roughness ratio Δ/H , the magnitude of the bending moment is the same for both the upper and the lower curve. The divergence of the two stress curves, then, is a direct result of the ice thickness used in the expression for the section modulus. It should be noted that both curves overestimate the theoretical bending stress present in the ice sheet. Neglecting the change in freeboard as the bottom surface is allowed to vary results in overestimating lateral loading on the beam. This effect is small for low roughness, but it can become significant as Δ/H increases.

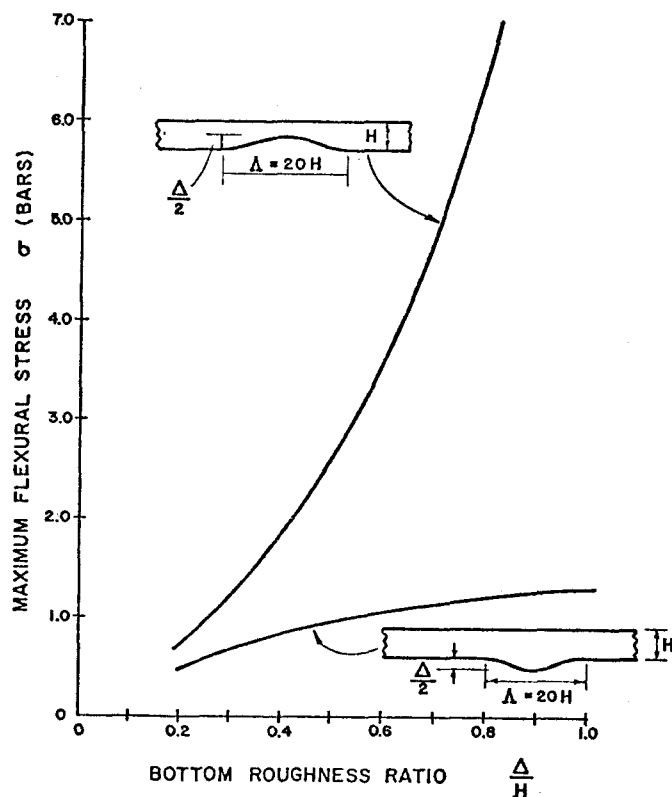


Fig. 2. Infinite beam. ($H = 3.0$ m.)

If we interpret the two curves in Figure 2 as upper and lower bounds on the bending stress that might result from random variation of the bottom surface, then we conclude that it is possible to reach the fracture stress at roughness ratios which are representative of actual sea ice.

Finite Beam on an Elastic Foundation

In the second one-dimensional case, we view the ice sheet as a finite beam on an elastic foundation subject to a single sinusoidal variation of the bottom surface. The flexural rigidity of the beam is assumed to be constant, and the foundation modulus is provided by the water. This case simulates conditions found in smaller ice sheets subjected to variable ice thickness loading. The beam idealization is shown in Figure 3. The ice is again assumed to be of constant thickness at first. Equilibrium is established between gravity and hydrostatic forces. The bottom surface is then permitted to grow to the assumed shape. Note that the symbol Δ has a slightly different definition from that used previously in the infinite beam model; here, Δ and the thickness variation are defined so as not to disturb the overall vertical equilibrium of the beam. Only symmetrical loadings are considered here, so that moment equilibrium is also maintained during the bottom surface transformation. It follows, then, that no change in the free-board will occur in this case. The effective loading is shown in Figure 3b. Both the beam length and the ice variation wavelength have been chosen to closely approximate the characteristic length of a beam-on-elastic foundation system.

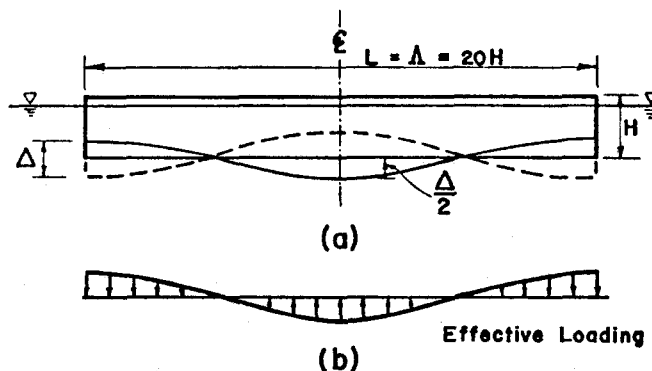


Fig. 3. Finite beam on an elastic foundation.

The solutions for this model, computed for the same range of roughness ratios used previously ($0.3 \rightarrow 1.0$), are shown in Figure 4. The solution curves given are similar to those for the infinite beam: the bending moment expressions for the upper and lower curves are equal but opposite in sign; their divergent nature is directly related to the ice thickness on the axis of symmetry; and they represent upper and lower bounds for the flexural stress in the actual ice cover. A comparison of the two sets of curves (Figs. 3 and 4) indicates that the flexural stresses induced in the beam of finite length are approximately two-thirds the stresses induced in the beam of infinite length for corresponding bottom roughness ratios.

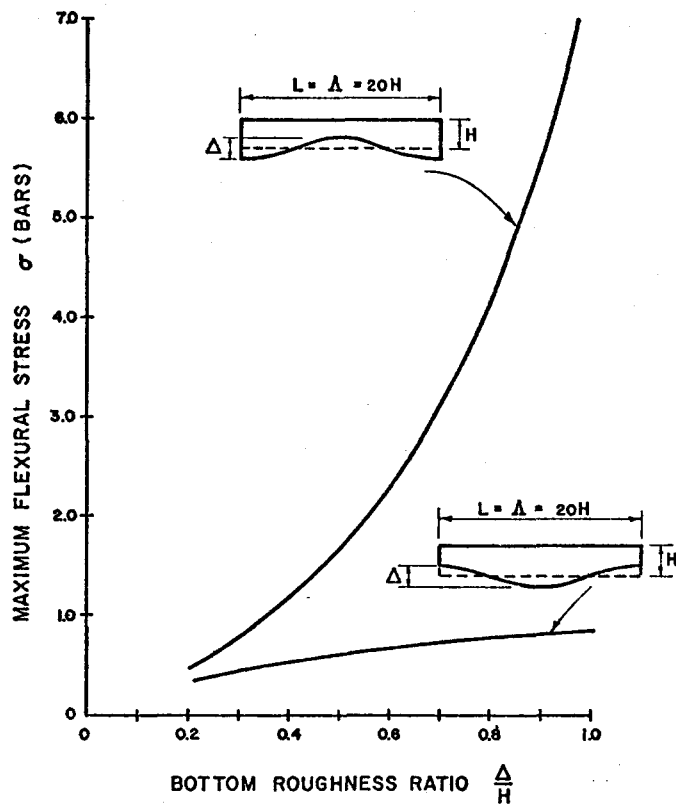


Fig. 4. Finite beam on elastic foundation. ($H = 3.0$ meters.)

Note that no force boundary conditions have been used in the above analysis. Since it is unreasonable to assume that cracks will be present in the pack ice at spacings which approximate the bottom surface wavelength, boundary conditions should be considered at each end of the beam model. If we consider

symmetrical conditions only, we can assume that realistic values of these boundary conditions may either amplify or diminish the flexural stress in the beam by a factor of two. While this may appear to reduce our model to a crude approximation, it is virtually impossible to analyze the finite-length beam without making the above simplifying assumptions.

Simplified Beam Method

We now introduce a simplified beam approach as an alternative method of analysis. The expressions for bending moment and flexural stress resulting from this method may be no shorter than their elastic foundation counterparts, but the complexity of the expressions for variable ice thickness loadings is considerably reduced. In this model the elastic foundation is neglected. The ice beam is represented as a free-floating rigid body in equilibrium with the supporting hydrostatic forces. Bending moments are caused by the bottom surface variation and the rigid body tilting which results from unsymmetrical geometry. Force boundary conditions are neglected. We will show that, for the types of loading discussed here, this simplified beam approach yields solutions that are in close agreement with those obtained by the more difficult elastic foundation method.

Figure 5a shows the simplified beam idealization in the original uniform-thickness configuration. The spatial coordinate x is measured from the left end. Figure 5b shows the assumed ice-thickness variation. Let the variation in the bottom surface, as measured from the original undeformed configuration, be defined by y_b . The assumed variation is expressed by:

$$y_b = \frac{\Delta}{2} \sin\left(\frac{2\pi x}{\Lambda} + \beta\right) \quad (1)$$

where Δ is the amplitude of the bottom roughness and β is the phase shift of the thickness variation from the origin. By introducing the phase shift β , consideration can be given to nonsymmetric loading conditions. In the discussion that follows, the beam length and the wavelength Λ are both taken to be approximately equal to the characteristic beam length for the elastic foundation method. This choice permits direct comparison of the

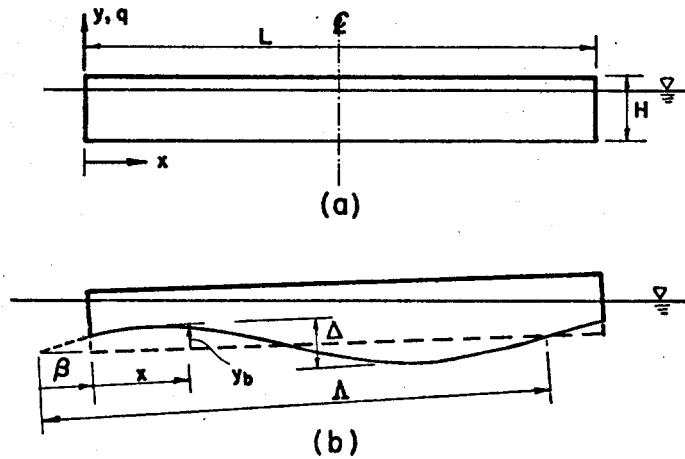


Fig. 5. Finite beam - simplified method.

two methods under consideration. Vertical equilibrium of the beam is satisfied for all values of β when $\Lambda = L$, but moment equilibrium is not assured. For nonsymmetrical ice variations, the beam must be tilted slightly to balance the overturning moments. The resulting lateral loading on the simplified beam is given by

$$q(x) = -(\rho_w - \rho_I) \frac{\Delta}{2} \sin\left(\frac{2\pi x}{\Lambda} + \beta\right) + q^1 \left(1 - \frac{2x}{L}\right) \quad (2)$$

where q^1 is defined as the effective lateral load at the end of the beam that results from the slight tilting of the beam as a rigid body. The negative sign preceding the first term reflects the fact that when y_b is positive (upward), the resulting lateral load on the beam is negative (downward). The expression for the bending moment at any position x along the beam is obtained by double integration of equation 2 with appropriate boundary condition. The resulting bending moment is expressed by

$$\begin{aligned} M(x) = & (\rho_w - \rho_I) \frac{\Delta}{2} \left\{ \left(\frac{\Delta}{2\pi}\right)^2 \left[\sin\left(\frac{2\pi x}{\Lambda} + \beta\right) - \sin\beta \right] \right. \\ & \left. - \left(\frac{\Delta}{2\pi}\right)x \cos\beta \right\} + q^1 \left(\frac{x^2}{2} - \frac{x^3}{3L} \right) \end{aligned} \quad (3)$$

The bending stress is computed from the equation

$$\sigma(x) = \frac{6M(x)}{t(x)^2} \quad (4)$$

where $t(x)$ is the thickness of the beam at position x . Since both $M(x)$ and $t(x)$ vary along the beam, the maximum value of $\sigma(x)$ will not necessarily occur at a section where $t(x)$ is a minimum or $M(x)$ is a maximum. These expressions can be studied with a digital computer to determine the effects of the parameters on the magnitude of the maximum bending stress. Solution curves similar to those in Figure 4 are shown in Figure 6. The curve $\beta = 3\pi/2$ corresponds to the upper bound curves in Figure 4, while $\beta = \pi/2$ corresponds to the lower bound curves. When these two sets of curves are compared (Fig. 7), it is apparent that the simplified beam method yields solutions which reasonably approximate those of the more precise elastic foundation method.

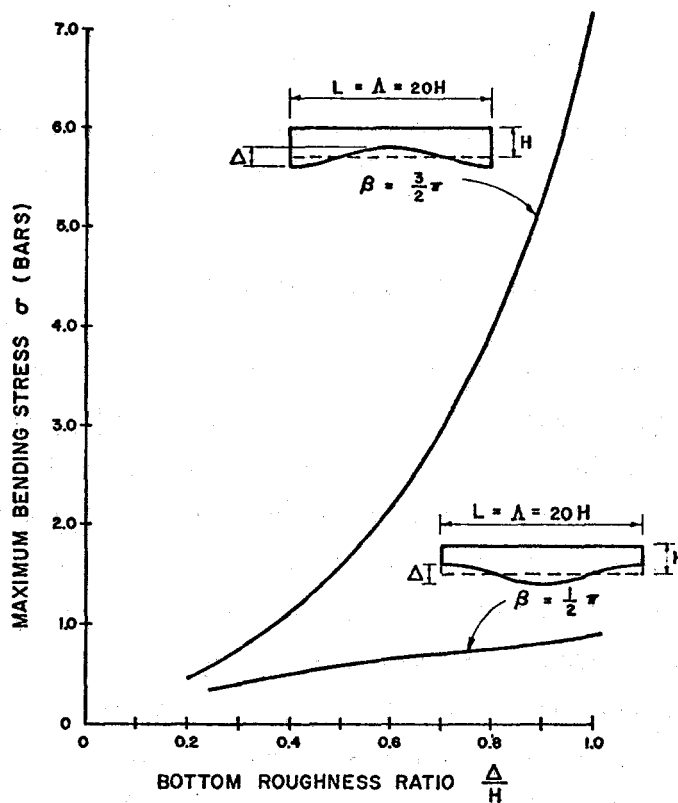


Fig. 6. Finite beam - simplified method. ($H = 3.0$ meters.)

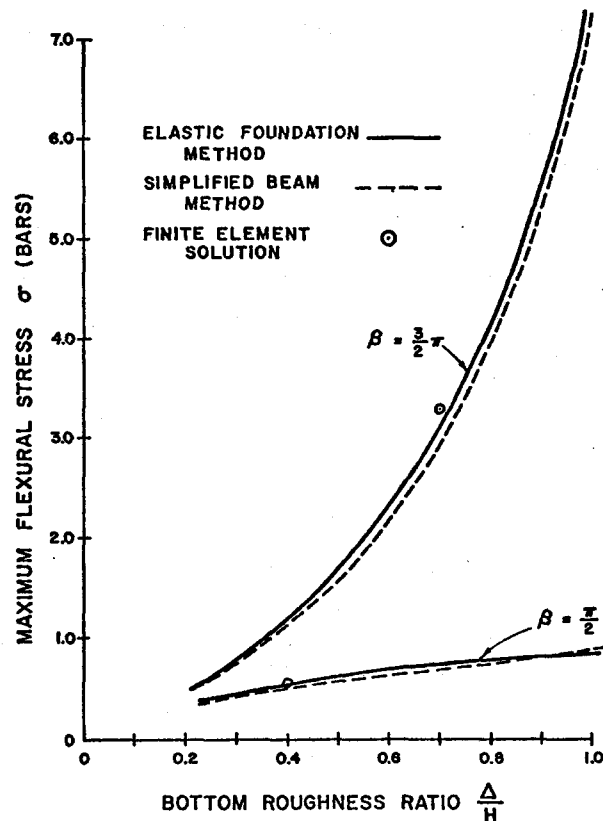


Fig. 7. Comparison of solution curves for beam-on-elastic-foundation method and simplified-beam method.

TWO-DIMENSIONAL ANALYSIS

Extending the previous methods of analysis to the two-dimensional variable-thickness plate problem presents a considerable challenge. Because this problem is so complex, we will not discuss an analytical approach here. However, in order to evaluate the significance of the one-dimensional solutions, we wish to obtain some numerical data for comparative purposes. Using the computerized finite-element method, we can examine several two-dimensional plate problems, considering only square plates with side dimensions equal to the characteristic length of the beam on an elastic foundation system. The effective loading on the plate is determined by the same procedure used in the simplified beam method. Two loading conditions are considered. The first condition permits the ice thickness to vary in one direction only. The maximum flexural stresses produced by this type of

loading are essentially identical to those of the one-dimensional solutions. Considering the large number of possible variations which exist in this format, no firm conclusions can be drawn from the results. However, solutions for three different thickness variations indicate maximum bending stresses which exceed the one-dimensional solution bounds for a given roughness ratio. Further study in this area is necessary to establish the true relationship between the one- and two-dimensional solutions.

SUMMARY

This study has examined the flexural stresses resulting from variable ice thickness within arctic pack ice. We have not placed as much importance on determining specific numbers as on understanding the load-stress phenomena and identifying the principal variables involved. Sinusoidal bottom surface variations are assumed and basic strength of materials techniques are applied. Solution bounds for three different one-dimensional models are presented and compared. Brief comments regarding the two-dimensional behavior are included. Only bottom surface variations are considered in the present study.

ACKNOWLEDGMENT

The author thanks Dr. Max D. Coon and Dr. R. Reid Parmerter for their informative discussions of the subject of this report. This study was supported by a subcontract to Seattle University from AIDJEX under NSF Grant GV-28807 with the University of Washington.

REFERENCES

- Assur, A. 1963. Breakup of pack-ice floes. In *Ice and Snow*, ed. W. D. Kingery. Cambridge, Mass.: MIT Press, pp. 335-347.
- Evans, R. J. 1971. Cracks in perennial sea ice due to thermally induced stress. *Journal of Geophysical Research* 76: 8153-8155.

Evans, R. J., and N. Untersteiner. 1971. Thermal cracks in floating ice sheets. *Journal of Geophysical Research* 76: 694-703.

Hetenyi, M. 1946. *Beams on Elastic Foundation*. Ann Arbor, Mich.: University of Michigan Press.

Hibler, W. D., S. Ackley, W. F. Weeks, and A. Kovacs. 1972. Top and bottom roughness of a multiyear ice floe. *AIDJEX Bulletin No. 13*, pp. 77-91.

Weeks, W., and A. Assur. 1967. The mechanical properties of sea ice. CRREL Report II-C3. U.S. Army Cold Regions Research and Engineering Laboratory, Hanover, New Hampshire.

ABSTRACTS OF INTEREST

All of the following abstracts were drawn from reports that appeared in the *Journal of Glaciology* 13(67), 1974.

J. Weertman: Stability of the junction of an ice sheet and an ice shelf (pp.3-11).

An analysis is made of the steady-state size of a two-dimensional sheet whose base is below sea-level and which terminates in floating ice shelves. Under the assumption of perfect plasticity it is found that an ice sheet placed on a bed whose surface was initially flat cannot exist if the depth of the bed below sea-level exceeds a critical depth. If this depth is less than the critical level, the ice sheet extends out to the edge of the continental shelf. Similar results are found with more realistic assumptions about the laws governing the flow of ice. If the bed slopes away from the centre, the ice sheet can have a stable width that increases in value as the accumulation rate increases or as sea-level is lowered. It is not possible to decide whether or not the West Antarctic ice sheet is in stable equilibrium. It is entirely possible that this ice sheet is disintegrating at present, as suggested by Hughes.

A. C. de La Casinière: Heat exchange over a melting snow surface (pp.55-72).

The relative importance of the principal elements of the thermal balance above snow during a period of melting has been evaluated using recent studies of the turbulent transfer in the boundary layer. Several anomalies in the profiles prove the continuing presence, near to the surface, of a thick layer of air apparently re-heated by the radiative flux. It is shown that the upper surface of this "exchange layer" ought to be considered as the new level for the origin of profiles, and taken as the exchange surface. The importance of nocturnal refreezing has been quantified. Excellent correlations have been found between mean air temperature and total energy balance; they have allowed the establishment of an approximate, non-linear expression for the effective daily ablation of snow as a function of mean air temperature. This relation gives satisfactory results at high and intermediate altitudes, in horizontal uncovered terrain. The measurements were made in the French Alps at 3,550 m and in Spain at the latitude of Madrid at 1,860 m.

(Abstracts of Interest)

W. Ambach: The influence of cloudiness on the net radiation balance of a snow surface with high albedo (pp. 73-84).

The short-wave and long-wave radiant fluxes measured in the accumulation area of the Greenland ice sheet during a mid-summer period are discussed with respect to their dependence on cloudiness. At a cloudiness of 10/10, a mean value of $270 \text{ J/cm}^2\text{d}$ is obtained for the daily totals of net radiation balance, whereas a mean value of only $75 \text{ J/cm}^2\text{d}$ is observed at 0/10. The energy excess of the net radiation balance with overcast sky is due to the significant influence of the incoming long-wave radiation and the high albedo of the surface (average of 84%). High values of net radiation balance are therefore correlated with high values of long-wave radiation balance and low values of short-wave radiation balance.

S. C. Colbeck: The capillary effects on water percolation in homogeneous snow (pp. 85-97).

A theoretical basis for introducing capillary effects into the theory of water percolation through snow is given. A capillary pressure-liquid saturation relationship found in the laboratory is used together with the theory to make a quantitative examination of capillary effects. It is shown that capillarity accounts for less than 10% of the total force when water flux is 10^{-8} m s^{-1} although the percentage rapidly increases for smaller fluxes. The experiments suggest that the irreducible water content of dense snow is 7% of the pore volume. It is concluded that the wave-front diffusion seen in lysimeter studies is not the result of capillary action. Other possible causes are suggested.

Charles F. Raymond: The local distribution of stress near a point of zero shear stress in a rectilinear flow field (Short Notes, pp. 141-143).

The distribution of stress in the vicinity of a point at which shear stress magnitude is zero is investigated analytically for rectilinear flow of a fluid in a channel or pipe. For a fluid with non-linear power-law properties the contours of constant stress and velocity either approach circular or flat shapes near such a point, irrespective of the particular boundary conditions. There are no intermediate cases, although such intermediate behavior exists for linear fluids.

CORECTIONS CORRECSIONS CORRECTIONS

The following errors should be corrected in D. Rothrock's two reports that appeared in AIDJEX Bulletin No. 23 (January 1974) on pages 45-51 and 53-81.

On page 47, in the second equation, $-h_L^*$ should be $-h_L$.

On page 48, lines 12 and 13, the expressions (0.1) and (0.9) should be (or about 0.1) and (or about 0.9).

On page 60, on the line below eq. 10, $\alpha(h)$ should be $\alpha(h)dh$.

On page 68, in Figure 8, the value of h at which W_r jumps from zero to $-k/(k-1)$ should be h^* , not h .

On page 70, in eq. 37, $\alpha_r(h)$ should be $\alpha_r(\theta)$.

